Coating and Printing on Chemically Patterned Surfaces

A dissertation submitted to the faculty of the
Graduate School of the
University of Minnesota
by

Sreeram Krishnamoorthy Kalpathy

In partial fulfillment of the requirements for the
degree of Doctor of Philosophy.

Advisors: Lorraine Francis and Satish Kumar

March, 2012

Acknowledgements

I would like to begin by thanking my advisors, Profs. Satish Kumar and Lorraine Francis, for giving me the opportunity to learn what research is all about, and for all the valuable guidance I have received from them during my stay at University of Minnesota. Their inputs have been very valuable, both in professional life as well as my overall development as a person. I have interacted with a number of peer graduate students at University of Minnesota in the last five years, and I should specially thank those who have more closely given me a lot of technical advice. Two prominent names among these are Scott Roberts and Shawn Dodds whom I would often approach to find an answer to the burning questions in my mind, especially coding issues. Other names worth mentioning are Balram Suman, Christine Cardinal, Heng Zhang, Erica Redline, Karan Jindal, Jin-Oh Song, Damien Brewer, Nazish Hoda, and Benson Tsai. They have all helped me on different ocassions and took their valuable time off to attend my research talks. I would also like to thank Dr. Wieslaw Suzynski for his timely advice and support in designing and conducting experiments in the lab, and helping me mature as an experimentalist too. This list is not exhaustive, and I wish to apologize if I have left out any important names here. At heart I am trying to a person who develops the impressions of gratitude towards people who do me even the slightest and timely favors.

A lot of credit goes to my friends Ankur Khare, Srijan Aggarwal, Saket Gupta, Pulkit Agarwal, and Ricky Jain, with whom I experienced a kind of comradeship that I never previously experienced in my life. As goes by without saying, my closest family members have always chipped in with timely moral support.

Contents

Acknowledgements **i**

Table of Contents **i**

List of Tables **iii**

List of Figures **iv**

1 Introduction **1**
1.1 Background . . . 2
1.1.1 *Creation of patterns* . . . 2
1.1.2 *Coating and Printing methods* . . . 5
1.1.3 *The physics of thin liquid film flows* . . . 8
1.2 Thesis Overview . . . 11
1.2.1 *Shear effects in the lithographic printing nip* . . . 11
1.2.2 *Thin film models for liquid displacement* . . . 12
1.2.3 *Thermally induced competitive dewetting* . . . 12

2 Shear-induced suppression of rupture in two-layer thin liquid films **13**
2.1 Introduction . . . 14
2.2 Problem formulation . . . 16
2.2.1 *Governing equations* . . . 16
2.2.2 *Numerical methods* . . . 20
2.2.3 *Linear stability analysis* . . . 21
2.3 Rupture behavior on homogeneous surfaces . . . 22
2.3.1 *Delay in rupture and parametric study* . . . 22
2.3.2 *Mechanisms* . . . 23
2.4 Rupture behavior in presence of wettability gradients . . . 28

2.5 Application to printing and nanofluidics/ microfludics . . . 30
2.6 Conclusions . . . 34

3 Thin film models of liquid displacement on chemically patterned surfaces for lithographic printing processes 37
3.1 Introduction . . . 37
3.2 Model . . . 41
3.2.1 *Evolution equation* . . . 41
3.2.2 *Linear stability analysis* . . . 43
3.2.3 *Numerical methods* . . . 45
3.3 Results and Discussion . . . 46
3.3.1 *Chemically homogeneous surfaces* . . . 46
3.3.2 *Chemically patterned surfaces: Effect of image size* . . . 47
3.3.3 *Chemically patterned surfaces: Effect of non-image size* . . . 51
3.4 *Application to lithographic printing and wire-wound rod coating* . . . 55
3.4.1 Lithographic printing . . . 55
3.4.2 Wire-wound rod coating . . . 57
3.5 Conclusions . . . 61
3.6 Appendix 1: Hamaker constants for multiple image areas on a domain 61
3.7 Appendix 2: Values of Hamaker constants for lithographic printing systems . . . 62

4 Thermally induced delay and reversal of liquid film dewetting on chemically patterned surfaces 65
4.1 Introduction . . . 65
4.2 Mathematical model . . . 68
4.2.1 *Governing equations* . . . 68
4.2.2 *Linear Stability Analysis* . . . 73
4.2.3 *Numerical methods* . . . 74
4.3 Results and Discussion . . . 75
4.3.1 *Uniform heating and cooling* . . . 76
4.3.2 *Localized heating and cooling* . . . 81
4.3.3 *Effects of repulsive intermolecular forces* . . . 91
4.3.4 *Simulations with realistic parameter values* . . . 98
4.4 Conclusions . . . 100

5 Conclusions 103
5.1 Summary of key results . . . 103
5.2 Directions for future work . . . 105
5.3 Final remarks . . . 106

Bibliography 107

List of Tables

1.1 Methods to create striped domains on substrates 4

2.1 Typical parameter values relevant to printing (MacPhee, 1998) 34

3.1 Comparison between the time it takes for the interface to first reach the equilibrium film thickness with the time it takes to reach the equilibrium film thickness at the center of the image area. 50

3.2 Estimates of surface tension values from Kaelble and Dynes (1975) . . 63

4.1 Typical values of the physical quantities present in M, H_1, and H_2 . . 72

List of Figures

1.1 A patterned coating: By chemical patterning, it is possible to modify a surface and deposit coating materials on selected areas 1
1.2 A computer memory device which uses microscale features. Figure taken from http://www.epson.co.jp/ 2
1.3 World's First roll-to-roll printed LED, from GE. Figure taken from http://www.gizmag.com/ 3
1.4 A schematic of the photolithographic process for creation of patterns. 5
1.5 A schematic of the lithographic printing process 6
1.6 A schematic of the wire-wound rod coating process 7
1.7 Prototypical geometry to illustrate the lubrication approximation. Here $\epsilon = \frac{H}{L} << 1$. 10

2.1 Schematic repesentation of the problem set up, with all labelled quantities in dimensional form. 16
2.2 Initial and rupture-time interface profiles for different shear velocities when $A_1 = 1$, $A_2 = 0$, $\mu_r = 1$, $h_0 = 0.5$, and $\gamma = 1$. 22
2.3 Effect of shear on rupture time for various viscosity ratios when $A_1 = 1$, $A_2 = 0$, $\mu_r = 1$, $h_0 = 0.5$, and $\gamma = 1$. Suppression of rupture occurs at a critical velocity at which there is a steep increase in rupture time (the point where the curves become vertical). This critical velocity decreases as μ_r increases for $0.1 < \mu_r < 3$, and increases thereafter for $\mu_r > 3$. 24
2.4 Gradients of flowrate components at the rupture location plotted against time, t for $V_0 = 25$. In both plots $A_1 = 1$, $A_2 = 0$, $h_0 = 0.5$, $\gamma = 1$, and $\mu_r = 1$. Rupture occurs at $t = 7.26$ for $V_0 = 0$ and at $t = 8.81$ for $V_0 = 25$. 24

2.5 Schematic showing the mechanism by which shear delays rupture. Shear propagates a traveling wave, causing a fluid element at the location of minimum interface height to move to a higher position on the interface. Van-der-Waals-assisted rupture wins so long as V_0 is less than a critical velocity. 26
2.6 Time period of the interface wave versus the viscosity ratio for $V_0 = 20$. The curve exhibits a minimum at $\mu_r = 3$. Here $A_1 = 1$, $A_2 = 0$, $h_0 = 0.5$, and $\gamma = 1$. This curve explains the trend in figure 2.3 where the critical velocity for suppression of rupture also exhibits a minimum. 27
2.7 Minimum interfacial height at various velocities. Here $A_1 = 1$, $A_2 = 0$, $\mu_r = 1$, $\gamma = 1$, and $h_0 = 0.5$ in all cases. For $V_0 = 40$ rupture is suppressed, and the minimum interface height oscillates around $h = 0.4$. 27
2.8 Effect of imposed shear on rupture time in the case of heterogeneous surfaces for image sizes $I = 1.95\lambda_{md}$ and $I = 0.3\lambda_{md}$. In both cases $A_2 = 0$, $h_0 = 0.5$, $\gamma = 1$, and $\mu_r = 1$. 28
2.9 Initial and rupture-time interfacial height profiles on heterogeneous surfaces for different imposed velocities when $I = 1.95\lambda_{md}$, $A_2 = 0$, $h_0 = 0.5$, $\gamma = 1$, and $\mu_r = 1$. 29
2.10 Flowrate components versus x at 50% completion, 90% completion and 99% of the time to rupture when $V_0 = 0$ and $I = 1.95\lambda_{md}$. Here $A_2 = 0$, $h_0 = 0.5$, $\gamma = 1$, and $\mu_r = 1$. 31
2.11 Flowrate components at 50% completion, 90% completion and 99% completion of the time to rupture when $V_0 = 10$ and $I = 1.95\lambda_{md}$. Here $A_2 = 0$, $h_0 = 0.5$, $\gamma = 1$, and $\mu_r = 1$. 32
2.12 Effect of shear on rupture time in bounded two-layer flows computed using parameters typical of microfluidic flows. Here μ_r is the ratio of top layer viscosity to bottom layer viscosity. 35

3.1 The lithographic printing process 39
3.2 Model geometry used to study liquid displacement. Liquid 1 represents water and Liquid 2 represents ink. 39
3.3 Time evolution of the interface on chemically homogeneous surfaces. . 46
3.4 Time taken to reach the equilibrium film thickness as a function of image size (in units of λ_{md}). 48
3.5 Steady-state interface profiles on chemically patterned surfaces for (a) $I_a = 0.3\lambda_{md}$, (b) $I_b = 0.8\lambda_{md}$, (c) $I_c = 1.15\lambda_{md}$, and (d) $I_d = 2.5\lambda_{md}$. . 48
3.6 Time evolution of the interface on a chemically patterned surfaces with a single image area of size $I = 0.8\lambda_{md}$. 50
3.7 Time evolution of the interface on a domain with alternating image and non-image areas with image size $I = 0.5\lambda_{md}$ and non-image size $N = 0.1\lambda_{md}$. 52
3.8 Steady-state interface profile for a domain with alternating image and non-image areas with image size $I = 0.5\lambda_{md}$ and non-image size $N = 0.4\lambda_{md}$. 52
3.9 Map demarcating the regions where 'spill-over' events are observed. . 54

3.10 Volume fraction of the bottom liquid 1 present on the non-image areas for $I = 1.5\lambda_{md}$. The plotted data is at time $t = 17.1$ when steady state has been reached. The labels 'top boundary' and 'bottom boundary' correspond to the boundaries of Figure 3.9. 54
3.11 Time evolution of the interface using parameter values characteristic of lithographic printing. Note that the scale of the x-axis is changing in each plot. 56
3.12 Illustration of the wire-wounding rod coating process for coating on chemically patterned surfaces. 58
3.13 Optical microscope images of wire-wound rod coating experiments. In all images the width of the hydrophilic stripes is 50 μm. The widths of the hydrophobic stripes are 100 μm (left image), 50 μm (center image), and 25 μm (right image). 58
3.14 Effect of film thickness on the non-image size at which spill-over is first eliminated. 60

4.1 The problem setup 66
4.2 Interface profiles at rupture for three different hydrophobic patch widths: (a) $0.1\lambda_{md}$, (b) $1.0\lambda_{md}$, and (c) $2.2\lambda_{md}$. In each case, $\bar{C} = 1$, $H_2 = 0$, and $M = 0$ uniformly throughout the domain. The variation of $H_1(x)$ is represented by the function (4.17) (see section 4.2.3) with $H_1 \to 1$ at the hydrophobic patch (hatched areas) and $H_1 \to 0$ on the hydrophilic areas (unhatched areas). 75
4.3 (a) Time to rupture as a function of $-M$ using initial perturbations with mean amplitudes of 0.01 and 0.4. In these calculations, the variation of $H_1(x)$ is represented by the function (4.17) (see section 4.2.3) with $H_1 \to 1$ at the hydrophobic patch (hatched areas) and $H_1 \to 0$ on the hydrophilic areas (unhatched areas). Further we set $w_h = 1.1\lambda_{md}$, $\bar{C} = 1$, and $H_2 = 0$. 77
4.4 Interface profiles at rupture for three different hydrophobic patch widths: (a) $0.1\lambda_{md}$, (b) $1.0\lambda_{md}$, and (c) $2.2\lambda_{md}$. In each case, $\bar{C} = 1$, $H_2 = 0$, and $M = 100$ uniformly throughout the domain. The variation of $H_1(x)$ is represented by the function (4.17) (see section 4.2.3) with $H_1 \to 1$ at the hydrophobic patch (hatched areas) and $H_1 \to 0$ on the hydrophilic areas (unhatched areas). 78
4.5 Rescaled rupture time as function of the hydrophobic patch width w_h for different values of M. Here, $\bar{C} = 1$, and $H_2 = 0$. The variation of $H_1(x)$ is represented by the function (4.17) (see section 4.2.3) with $H_1 \to 1$ at the central hydrophobic patch and $H_1 \to 0$ on the hydrophilic areas. For $w_h = 0$, the absolute rupture time values are $T_r \to \infty$, $T_r = 2.8$, and $T_r = 7$ x 10^{-3} for $M = 0$, $M = 5$, and $M = 100$ respectively. 80
4.6 Typical spatial variations of $M(x)$ and $H_1(x)$ on a chemically patterned surface. 82

4.7 Interface profiles at rupture for three different hydrophobic patch widths. Here, $\bar{C} = 1, H_2 = 0$, $M(x)$ and $H_1(x)$ vary as in Figure 4.6(a), according to the analytical function defined in section 4.2.3.Further, we set $w_M = w_h$ in all cases. 83
4.8 Interface profiles at rupture for three different hydrophobic patch widths. Here, $\bar{C} = 1$, $H_2 = 0$, $M(x)$ and $H_1(x)$ varies as in Figure 4.6(b), i.e., $M(x) = -100$ on the hydrophobic patches (hatched areas), and $M(x) = 100$ on the hydrophilic patches (unhatched areas). Further, we set $w_M = w_h$ in all cases. 85
4.9 Interface profiles at rupture for three different hydrophobic patch widths. Here, $\bar{C} = 1$, $H_2 = 0$, $H_1(x)$ and $M(x)$ vary as in Figure 4.6, with $H_0 = 1$ and $M_0 = -1$. Further, we set $w_M = w_h$ in all cases. 86
4.10 Variation of rupture time as a function of the width w_M of the cooled region of the domain for different hydrophobic patch widths w_h. Here $C = 1$, $H_2 = 0$, and $H_1(x)$ and $M(x)$ vary according to the analytical functions described in section 4.2.3, with $H_0 = 1$ and $M_0 = -100$. . . 87
4.11 Critical Marangoni number as function of the hydrophobic patch width w_h for localized cooling at the center with with $\bar{C} = 1$, $h_0 = 1$, and $H_2(x) = 0$. Here $H_1(x)$ is modeled by the function (4.17) (section 4.2.3) with $H_0 = 1$. Further we set $w_M = w_h$. 89
4.12 Interfacial profiles resulting from the dewetting of a film when $M = 0$ and $\bar{C} = 1$. Here $H_1(x)$ and $H_2(x)$ are modeled by the function (4.17) (section 4.2.3) with their maximum values being 1 and 0.1 respectively. Further, we set $w_h = w_M$ in all cases. 91
4.13 Interface profiles at $t = 1.0$ x 10^{-3} for a dewetted film with $M(x) = 1$ throughout the domain and $\bar{C} = 1$. Here $H_1(x)$ and $H_2(x)$ are modeled by the function (4.17) (section 4.2.3) with their maximum values being 1 and 0.1 respectively. Further, we set $w_h = w_M$ in all cases. 92
4.14 Interface profiles at $t = 1.0$ x 10^{-3} for a dewetted film with $\bar{C} = 1$. Here $H_1(x)$ and $H_2(x)$ are modeled by the function (4.17) (section 4.2.3) with their maximum values being 1 and 0.1 respectively. The parameter $M(x)$ is modeled using function (4.18) (section 4.2.3) with $M_0 = 100$, and $w_h = w_M$ in all cases. 93
4.15 Interface profiles at rupture for a dewetted film with $\bar{C} = 1$. The paremeters $H_1(x)$, $H_2(x)$ and $M(x)$ vary as in the functions in section 4.2.3. The maximum values of H_1 and H_2 are 1 and 0.1 respectively, while $M_0 = -100$, and $w_h = w_M$ in all cases. 95
4.16 Interface profiles at rupture for a dewetted film with $\bar{C} = 1$. We set $H_2(x) = 0.1$ uniformly throughout the domain, while $H_1(x)$ and $M(x)$ vary as in the functions in section 4.2.3 with $H_0 = 1$, $M_0 = -100$, and $w_h = w_M$ in all cases. 96

4.17 (a) Steady state interface profile for a dewetted film with several hydrophobic patches packed in the domain, each separated by a hydrophilic patch of width $0.5\lambda_{md}$. Here $\bar{C} = 1$. Governed by the functions in section 4.2.3, $H_1(x) \to 1$ and $M(x) \to 1$ on the hydrophobic patches (hatched) of width $w_h = 0.6\lambda_{md}$. Here $w_M = w_h$ and $H_1(x) \to 0$ and $M(x) \to 0$ elsewhere in the domain. We also model $H_2(x)$ by the function (4.17) in section 4.2.3 with $H_0 = 0.1$. (b) The same figure as in (a), but with a hydrophilic patch width of $0.1\lambda_{md}$. . 96

4.18 Critical hydrophobic patch width required to avoid the "spill-over" effect in the presence and absence of thermocapillary effects. These results were obtained using $\bar{C} = 0.05$. Here $H_1(x)$ and $H_2(x)$ are modeled by the function (4.17) (section 4.2.3) with their maximum values being 1 and 0.1 respectively. The parameter $M(x)$ was also modeled similar to $H_1(x)$ and $H_2(x)$, with the maximum value of $M(x)$ being 100 at the hydrophobic center and $M(x) \to 0$ at the hydrophilic areas of the domain. 97

4.19 Interface profiles at rupture for hydrophobic patch widths of $0.3\lambda_{md}$, $1.2\lambda_{md}$, and $2.5\lambda_{md}$. In each case, $H_1(x)$ and $M(x)$ were modeled using the functions (4.17) and (4.18) (section 4.2.3), where we set $H_0 = 3.5$ x 10^{-4} and M_0 = -4.0 x 10^{-2}. Further $h_0 = 1$, $H_2 = 0$, $w_h = w_M$, and $C = 0.01$. 99

4.20 Schematic of the lithographic printing process. 102

CHAPTER 1

Introduction

A variety of coated products require coatings with micro and nanoscale patterns (see Figure 1.1). In addition to traditional printed products, applications of such patterned coatings include flexible electronics (e.g., see figure 1.2), RFID tags, microlenses, and bioanalytical devices. All these products require either selective printing of microscale features or coating by means of selective material deposition. While the term 'coating' generally refers to depositing the target material (usually a liquid or a suspension of solid particles in a liquid) onto an entire surface, printing usually involves deposition of the material in discrete locations of a surface. Especially exciting from an industrial standpoint is the creation of patterned coatings in continuous webs, which can be used for low cost manufacture of flexible displays and several other applications (McCollough et al., 2006; Chaug et al., 2004; Goto, 2007). For instance, figure 1.3

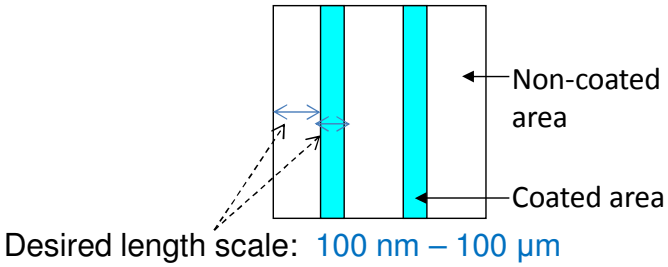

Figure 1.1: A patterned coating: By chemical patterning, it is possible to modify a surface and deposit coating materials on selected areas

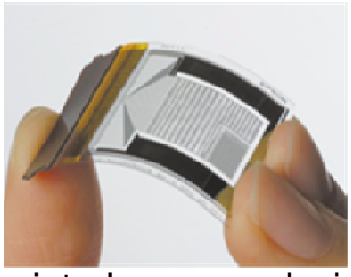

Figure 1.2: A computer memory device which uses microscale features. Figure taken from http://www.epson.co.jp/

shows the world's first "roll-to-roll" printed LED from GE. Creating these patterns in a continuous, roll-to-roll manner offers economic advantages, but presents challenges, such as developing techniques for rapid pattern formation. These patterns are commonly developed by chemical modification of the surface features (see section 1.1.1). Once the patterns are successfully created, the major challenge lies in being able to subsequently coat or print selectively on the desired pattern. The present work closely examines the key scientific aspects of coating or printing on such features. A major part of the thesis lays emphasis on the process known as the lithographic printing process (MacPhee, 1998), a leading technique for printed mass media and a promising candidate for the manufacturing of printed electronic devices. However, the models used and principles derived from these studies are also applicable in general to other methods of coating and printing on chemically patterned surfaces.

1.1 Background

1.1.1 *Creation of patterns*

An important step in creating patterned coatings is patterning the substrate. By patterning, we refer to the creation of preferential locations on the substrate where the coating liquid or particles can be deposited. Patterning may be done chemically, by creating regions of surface energy or wettability contrasts; or by creating differences in topography, such as trenches and holes on the substrate where coating liquid may be deposited. The two major interactions by which substrates are chemically patterned are (1) differences in wettability (Heule et al., 2004), and (2) differences in charge (Clark et al., 1997) between the patterned and unpatterned areas on the substrate.

http://www.gizmag.com/
First roll-to-roll printed LED, from GE

Figure 1.3: World's First roll-to-roll printed LED, from GE. Figure taken from http://www.gizmag.com/

For example, an aqueous liquid overlaid on a substrate patterned with hydrophobic and hydrophilic areas will potentially redistribute itself prefentially to the hydrophilic areas. On the other hand, negatively charged target particles will be attracted to the positively charged features of a pattern, enabling selective deposition. The research described in this thesis caters to the former approach, while the latter is commonly employed in biological research fields such as cell and nuclear membranes, where polyelectrolyte molecules are adsorbed near charged patterned substrates (Hoda and Kumar, 2008).

As far as patterning techniques are concerned, there has been a significant amount of research into creating striped domains on substrates. A list of such techniques now prevalent, meant for creating stripes on the millimeter, micron and nanometer length scales is presented in Table 1. Photolithography has by far turned out to be the most popular due to its ease of working for the creation of nano- and micron-sized patterns for integrated ciruits, microfluidic channels, and other electronic devices. It is also the basis of the patterned images and coatings described in this thesis, so we turn to a brief description of photolithography alone, omitting a comprehensive analysis of other techniques.

With electronic devices being the major motivation for the photolithographic process, it is most easily demonstrated on a silicon wafer (Reynolds, 2007). To begin with, the native oxide film on the wafer has to be removed and a new clean oxide layer grown. To accomplish this, the wafer is first immersed into a Buffered Oxide Etch (BOE) solution (consisting of Ammonium Fluoride, Hydrofluoric acid and water) and the residue removed using de-ionized water. Next, the wafer surface is hydroxylated

Table 1.1: Methods to create striped domains on substrates

Millimeter length scales	**Micron length scales**	**Nanometer length scales**
1. Screen printing technique (Silver et al., 1999)	1. Elastomer stamps technique (Lopez et al., 1993)	1. Lithography with colloid monolayer (Burmeister et al., 1998)
2. Printed circuit board technology (Lenz et al., 2001)	2. Vapor deposition through grids (Drelich et al., 1994)	2. Atomic beams modulated by light masks (Drodofsky et al., 1997)
	3. Photolithography of amphiphilic monolayers (Moller et al., 1998)	3. Microphase separation in diblock copolymer films (Heier et al., 1997)
	4. Langmuir-Blodgett monolayers (Wang et al., 1999)	4. Local oxidation of Si surfaces induced by AFM (Garcia et al., 1998)
	5. Electrophoretic assembly of colloids (Hayward et al., 2000)	
	6. Anisotropic rupture of polymer films (Higgins and Jones, 2000)	

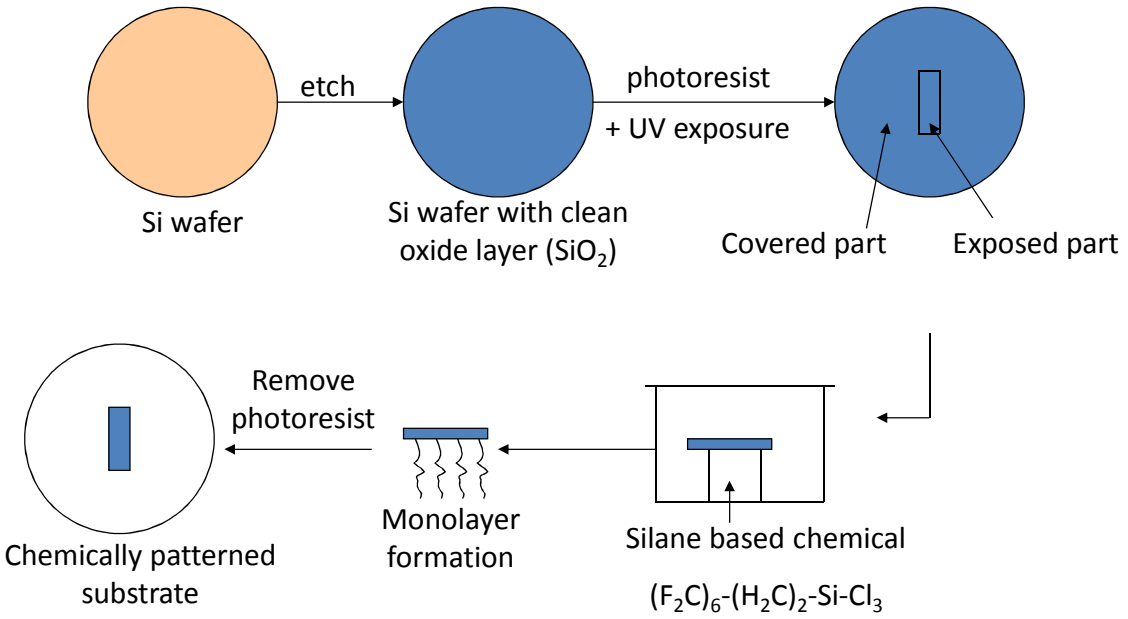

Figure 1.4: A schematic of the photolithographic process for creation of patterns.

by immersing in the piranha solution (H_2SO_4:H_2O_2=10:1) at temperatures $\sim 120\,^{\circ}C$, and dried to remove residual water.

A chromium mask, designed with the specified pattern is conventionally used in photolithography, though the emergence of transparent soft masks (Qin et al., 1998) has considerably simplified the work of the experimentalist involved. When a substrate coated with a light-sensitive organic material (known as the photoresist) is exposed to UV light, the resulting photoreaction induces crosslinking of the polymer chains in the photoresist. If the substrate is initially coated with photoresist, it is possible to expose selected regions of the substrate to UV light using a mask. Thus one can cause crosslinking of the polymer in the photoresist in the exposed region of the substrate. The remaining photoresist is washed off using suitable organic solvents (typically known as developers). One then has the desired pattern on the substrate.

1.1.2 *Coating and Printing methods*

Conventional coating and printing methods have existed in practice in the industry for almost a century. However, not all techniques have been examined for their adaptibility for the creation of patterned coatings or images. One method to produce patterned coatings is to deposit particles or coating liquids onto such chemically patterned surfaces, using simple laboratory coating methods as dip coating (Scriven,

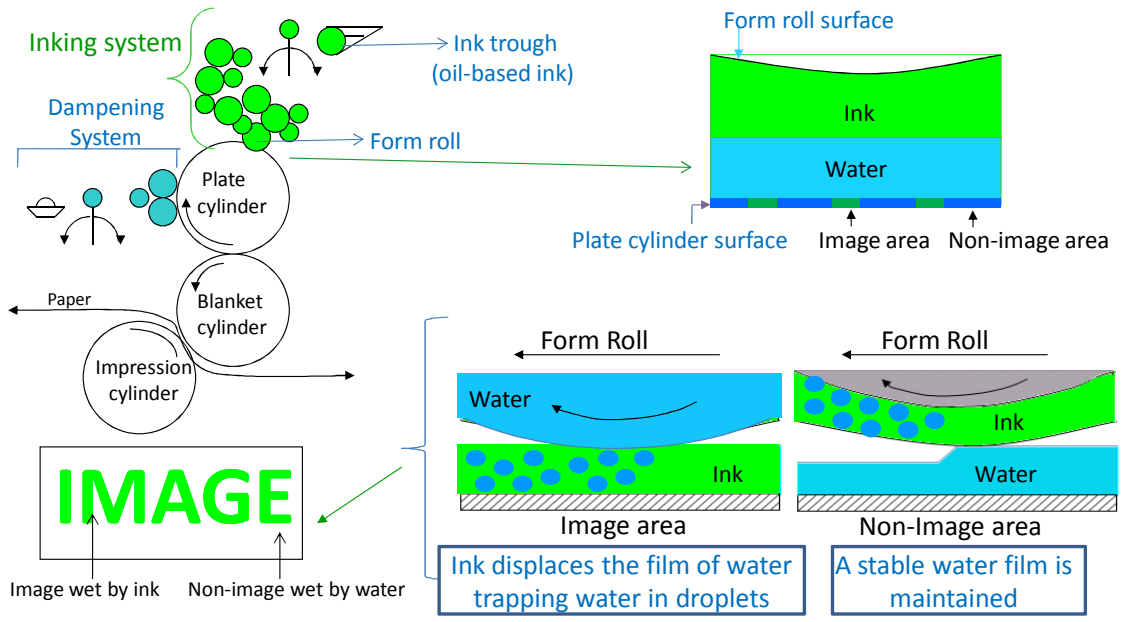

Figure 1.5: A schematic of the lithographic printing process

1988) or wire wound rod coating (MacLeod, 2006). Likewise, lithographic printing (MacPhee, 1998), the leading technique for printed mass media, relies on selective "inking" of micropatterned surfaces. Flexographic printing (Kipphan, 2006), gravure (Kasunich, 1998), and ink-jet printing (Michel et al., 2001) are other closely related conventional printing processes, and each technique has its underlying merits and demerits in terms of its resolution and utility for an application of given nature. The reader is referred to the review by Dodds (2011) for a detailed comparison. We move on to the details of two major techniques relevant to the research in the present thesis, the lithographic printing process and the wire-wound rod coating process.

The lithographic printing process

Figure 1.5 depicts the principal components of a lithographic printing press. The pattern containing the image to be printed is first created on a thin film of a flexible substrate, typically a polymer film, by standard photolithographic techniques (see section 1.1.1). The film is then wrapped around the plate cylinder surface, which therefore has regions with distinct wettability differences. A thin film of highly viscous oil-based ink is then transferred onto the chemically patterned printing plate from the ink rolls through a thin barrier film of an aqueous fountain solution. The regions of distinct wettability on the plate cylinder surface are known as 'image areas' and 'non-image areas'. The 'image areas' are those which can be wet more easily by the ink

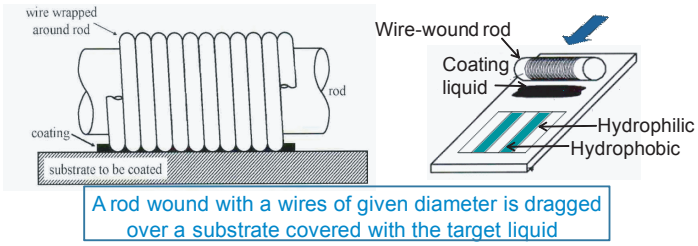

Figure 1.6: A schematic of the wire-wound rod coating process

and the 'non-image areas' are wet more easily by the water-based fountain solution. The blanket cylinder and the impression cylinder help successfully transfer the image on to the substrate, usually a roll of paper.

Herein we investigate the key fluid mechanical aspects of the process such as liquid-liquid displacement and film rupture using mathematical models. Prior researchers in this field have at best tried to model flow of similar thin liquid film systems and give generic descriptions about instability in flow (Oron et al., 1997; Kargupta and Sharma, 2002a; Joo and Hsieh, 2000). The component that is lacking in prior work, and what we try to achieve here, is a specific consideration to how these models could be tailored to extract principles relevant to real-world lithographic printing process such as effect of shear (see Chapter 2), mechanisms of liquid displacement, and image resolution (see Chapter 3).

The wire-wound rod coating process

The wire-wound rod coating process (Hanumanthu and Scriven, 1996) is sometimes termed as the Mayer-rod coating technology in credit to its inventor Charles W. Mayer (founder of Mayer Coating Machines Company, 1905, NY). Next to gravure and reverse roll coating, it is the third most popular technique in use in the coatings world (Tracton, 2006). Figure 1.6 schematically depicts the working of the process for creation of a patterned coating. To begin with, a thin film of the coating liquid is deposited onto on a chemically patterned substrate. The excess liquid is then metered off by coating using rods wound with wires of known diameters (Figure 1.6). On a chemically homogeneous surface, the initial shape of the coating after applying the metering rod is a series of stripes, spaced apart according to the spacing of the wire windings. Almost immediately, surface tension of the liquid film pulls these stripes together, forming a flat and smooth surface, ready for the following drying and curing process through heat or UV light sources. However if the substrate is chemically patterned, the coating also results in subsequent redistribution of the liquid onto the

hydrophilic areas (if the liquid is aqueous) or the hydrophobic areas (if the liquid is non-aqueous). The underlying fluid mechanics of liquid distribution is therefore more complex, and some of these details are investigated in Chapter 3.

The rods and wires are typically made of stainless steel, due to its superior corrosion-resistant properties. Typical wire diameters can vary from 0.18 mils to 13.5 mils for different coating thickness. The grooves between the wire coils determine the precise amount of coating materials that will pass through as it is moved along the web. Prior research suggests that the wet film coating thickness may be estimated to be $\sim$0.173 times the wire diameter. In practical coating production, many other factors can influence the actual coating thickness, such as the viscosity of the liquid, web tension, moving speed of the web, wettability of the liquid, and penetration of the liquid into the base material.

Wire-wound rod coating on chemically homogeneous substrates is especially useful for the creation of thin coatings with precise thickness deposition at a much faster rate than other conventional processes (e.g., dip coating (Scriven, 1988)). This is primarily because the process is rate-independent. The technique has also gained popularity due to the low costs involved in setting up a continuous coating process. However, metering rods work best with low viscosity liquids which flow easily between the wire windings. Further, coating speeds of metering rod method are usually limited to 1000 ft/min (Satas and Tracton, 2000), since the striations formed by the metering rod need a certain amount of time to level out before the web is dried.

1.1.3 *The physics of thin liquid film flows*

Thin liquid films are ubiquitous in coating and printing flows. When the mean thickness of these films are in the range of a few 100 nm or smaller, the stability of these films would be more aptly modeled by incorporating physics different from those for a thicker film. Some of these aspects are the weaker presence of gravity (which may be often ignored), the dominant role of disjoining forces (e.g., van der Waals forces) and the validity of lubrication theory. A crisp description of these aspects is presented below.

Lubrication Approximation

The foundation of lubrication theory was laid by the work of Reynolds (1886), motivated by fluid-lubricated slipper bearings. It is now a commonly applied theory in several coating flows, printing processes, polymer processing and biophysical phe-

nomena, as they are dominated by flow of thin liquid films.

Consider the prototypical geometry shown in figure 1.7. This shows flow of a liquid film over a horizontal surface, with a free-surface boundary. Let H be the change in height of the vertical boundary at the right ($x = x_2$), and L be the horizontal distance over which this change occurs. The boundary at the left is positioned at $x = x_1$. The bottom surface is moving with a velocity U to the right. Consider the situation $\epsilon = \frac{H}{L} << 1$. In such a case, it is possible to simplify the continuity and momentum-balance equations (Deen, 1998) considerably by retaining only the leading order terms in the limit $\epsilon \rightarrow 0$. This is known as the lubrication approximation. The continuity equation is expressed as:

$$\frac{\partial u}{\partial x} + \frac{\partial w}{\partial z} = 0, \tag{1.1}$$

where u and w are the liquid velocities in x and z direction respectively. We may now non-dimensionalize the horizontal distances with L and vertical distances with $H = \epsilon L$. We shall represent the resulting dimensionless quantities with an asterisk(*) superscript, as

$$x^* = \frac{x}{L}; \quad z^* = \frac{z}{H}. \tag{1.2}$$

The velocities u and w are scaled as

$$u^* = \frac{u}{U}; \quad w^* = \frac{w}{\epsilon U}. \tag{1.3}$$

The characteristic time scale to non-dimensionalize time t in the problem is $\frac{L}{U} = \frac{H}{\epsilon U}$, so that

$$t^* = \frac{t}{L/U} \tag{1.4}$$

is the dimensionless time. Pressure p of the fluid is scaled as $p^* = \frac{p}{p_c}$ where $p_c = (\mu U/\epsilon^2 L)$ and μ is the liquid viscosity. Using these scalings the dimensionless momentum balance equations (Deen, 1998) in the x and z directions are written as:

x-momentum

$$\rho\left[\frac{U^2}{L}\frac{\partial u^*}{\partial t^*} + \frac{U^2}{L}u^*\frac{\partial u^*}{\partial x^*} + \frac{\epsilon U^2}{H}w^*\frac{\partial u^*}{\partial z^*}\right] = \mu\left[\frac{U}{L^2}\frac{\partial^2 u^*}{\partial {x^*}^2} + \frac{U}{H^2}\frac{\partial^2 u^*}{\partial {z^*}^2}\right] - \frac{p_c}{L}\frac{\partial p^*}{\partial x^*} \tag{1.5}$$

z-momentum

$$\rho\left[\frac{\epsilon U^2}{L}\frac{\partial w^*}{\partial t^*} + \frac{\epsilon U^2}{L}u^*\frac{\partial w^*}{\partial x^*} + \frac{\epsilon^2 U^2}{H}w^*\frac{\partial w^*}{\partial z^*}\right] = \mu\left[\frac{\epsilon U}{L^2}\frac{\partial^2 w^*}{\partial {x^*}^2} + \frac{\epsilon U}{H^2}\frac{\partial^2 w^*}{\partial {z^*}^2}\right] - \frac{p_c}{H}\frac{\partial p^*}{\partial z^*} \tag{1.6}$$

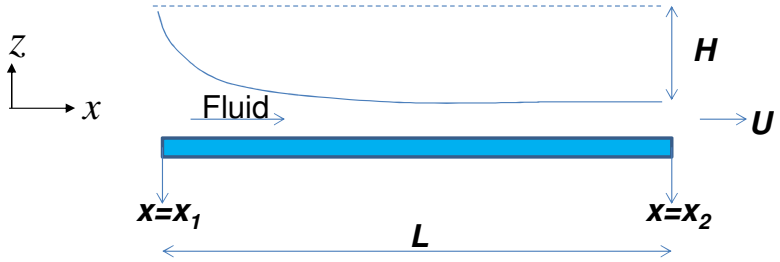

Figure 1.7: Prototypical geometry to illustrate the lubrication approximation. Here $\epsilon = \frac{H}{L} << 1$.

The equation set is considerably simplified in the limit $\epsilon \to 0$; or equivalently expanding p^*, u^*, w^* in terms of ϵ and retaining only the leading order terms in equations (1.5) and (1.6). The final set of equations in dimensionless form is given by

$$\begin{aligned} \frac{\partial u^*}{\partial x^*} + \frac{\partial w^*}{\partial z^*} &= 0 \\ 0 = \frac{\partial p^*}{\partial x^*} + \frac{\partial^2 u^*}{\partial {z^*}^2} \\ 0 = -\frac{\partial p^*}{\partial z^*} \end{aligned} \tag{1.7}$$

The set of equations (1.7) is known as the lubrication equations. It is a convenient approximation in modeling many thin film problems in coating and printing flows.

Disjoining Pressure and Van der Waals Forces

Disjoining pressure is a measure of chemical potential change in thin liquid layers. It determines the stability of thin films through contributions from electrostatic forces, van der Waals forces or steric forces such as in polymer films. This is mathematically expressed as

$$\pi = \pi_{el} + \pi_{vdw} + \pi_{st} \tag{1.8}$$

where π_{el}, π_{vdw}, and π_{st} are pressure terms which denote contributions from electrostatic, van der Waals and steric or structural forces, and π denotes total disjoining pressure. Of these, the van der Waals force is very significant because an attractive component of van der Waals force is always present between two materials, like the gravitational force. Our interest in this topic arises from our research in colloidal particles and thin liquid films. While the gravitational force of attraction between two materials can be neglected at very small dimensions as $\sim$ 100 nm, short-range

van der Waals forces become important at these dimensions. Generally contributions from π_{vdw} are mostly negative, indicating the attrative nature of van der Waals forces, while π_{el} and π_{st} have positive contributions, representing repulsive forces that stabilize thin films. Disjoining forces may be expressed in terms of a potential energy per unit volume. For example, the van der Waals contribution to potential energy of attraction felt by a particle i, when suspended above a semi infinite material j is equal to A_{ij}/h^3 where the constant A_{ij} is known as the Hamaker constant between materials i and j. This form was first obtained by Hamaker (1937) and used by Vrij (1966) and Sheludko (1967) in their work on thin film stability.

1.2 Thesis Overview

1.2.1 *Shear effects in the lithographic printing nip*

The lithographic printing process described in section 1.1.2 involves displacement of a thin layer of a water-like fountain solution by an oil-based ink. In a typical lithographic printing nip, high shear rates of $\sim 10^5$ s^{-1} are experienced in the printing nip between the ink roller and printing cylinder surfaces (MacPhee, 1998). To simulate these conditions in printing, we examine in Chapter 1, the effect of shear on stratified flow of two thin liquid films within a channel of parallel solid surfaces, and subject to dewetting by van der Waals forces. The model employed here is an idealization as explained in Chapter 2, based on prior work by Lenz and Kumar (Lenz and Kumar, 2007a). Modification of the characteristic wetting behavior of the solid surfaces by chemical patterning is also considered.

Lubrication theory (see section 1.1.3) is applied to derive a single nonlinear evolution equation in space and time for the liquid-liquid interface. Interface behavior between homogeneous surfaces is considered first, followed by an analysis of flow between chemically heterogeneous surfaces. Results derived from nonlinear simulations are supported by predictions from linear stability analysis. It is found that shear delays interfacial rupture, and suppression of rupture occurs beyond a critical shear rate. We focus particularly on the rupture time, as it is particularly significant for the application of lithographic printing where intentional rupture is desired. As seen in Chapters 2 and 3, the rupture time is a key time scale which could affect the throughout of the process, and additionally provide insights about the inherent mechanism that is responsible for rupture.

1.2.2 *Thin film models for liquid displacement*

In Chapter 3, we probe more extensively the dynamics of the liquid displacement within the nip, extending the idealized model of Lenz and Kumar (Lenz and Kumar, 2007a) as a starting point. In addition to the role of attractive van der Waals forces examined earlier (Lenz and Kumar, 2007a), here we include a repulsive component of the intermolecular force in our model, which prevents a thin liquid film from rupturing completely. Additionally, in Chapter 3, we probe the distinct role of both the 'image' size and the size of the 'non-image' areas to understand the constraints that lithographic printing imposes on the resolution of printed features. By incorporating the physics of repulsive intermolecular forces, we obtain further insights into the post-rupture dynamics and the mechanics of emulsification of ink in an aqueous film. Examination of length scales enables us to obtain estimates of the smallest and the largest image sizes one can print using lithographic printing. Besides, addressing the distinct role of 'non-image' area size reveals how densely features can be printed.

1.2.3 *Thermally induced competitive dewetting*

In Chapter 4, we examine the role of surface tension gradients arising in thin liquid film flows due to temperature variations across the film. When a thin liquid film with rests on a chemically patterned solid substrate, the competition between the resulting wettability gradients and the surface-tension gradients could lead to many interesting dynamics. These effects could be suitably manipulated to serve as important transport mechanisms for various industrial applications, in particular coating and printing processes, and also microfluidic delivery through miniaturized network assemblies. The prototype model we consider here caters primarily to a single-layer flow, though it serves as a starting point to understand two-layer flows more aptly suited for modeling the lithographic printing process which forms the basis for Chapters 2 and 3. The model suggests tremendous practical relevance of using controlled temperature effects for manipulating rupture patterns for templating applications and controlling flow in patterned microfluidic channels (Squires and Quake, 2005).

CHAPTER 2

Shear-induced suppression of rupture in two-layer thin liquid films

The effect of shear on the rupture of two stratified thin liquid films confined between parallel plates and subject to van der Waals forces is examined in this work. Lubrication theory is applied to derive a one-dimensional nonlinear evolution equation for the height of the liquid-liquid interface. Linear stability analysis reveals that the real part of the growth rate and the wavelength of the fastest growing interfacial disturbance are unaffected by shear. However, the growth rate has an imaginary part which is non-zero in the presence of shear, indicating the existence of traveling waves. Nonlinear simulations of interface behavior on homogeneous surfaces show that shear delays interfacial rupture, and suppression of rupture occurs beyond a critical shear rate. Propagation of traveling waves along the interface, and subsequent weakening of van-der-Waals-driven dewetting, is found to be the cause of the rupture delay. Analysis of flow on chemically heterogeneous surfaces also suggests a delay in interfacial rupture in the presence of shear. The problem studied here can serve as an idealized model for the lithographic printing process, and the results suggest that in the regime of shear rates relevant to printing, mechanisms of emulsification of one liquid into the other can be understood without incorporating shear. However, shear could be relevant in other physical systems such as nanofluidic and microfluidic flows.

2.1 Introduction

Thin liquid films have been a subject of extensive study in fluid mechanics in part because they occur in a number of industrial applications (Oron et al., 1997). The stability of such films is particularly relevant to several coating and printing processes (Kistler and Schweizer, 1994; Powell et al., 2005). Studies of the stability of thin liquid films may be broadly categorized into those involving single-layer flows and multi-layer flows. Although the former has dominated much of the literature to date, an increasing number of applications such as lubricated piping (Preziosi et al., 1989), oil recovery (Speight, 2007), and lithographic printing (MacPhee, 1998) involve multi-layer flows.

When a thin liquid film is bounded by another thin liquid film adjacent to a solid surface, and both films are subject to van der Waals forces, one film can displace the other and cause rupture of the latter. The natural length scale associated with the rupture is the wavelength of the perturbation at the liquid-liquid interface that grows the fastest. Such competitive displacement of thin liquid films has been studied by Lenz and Kumar (2007a) as a starting point to model lithographic printing. As acknowledged in their work, one of the factors that may affect liquid displacement is shear in the printing nip. In this paper, we examine the effect of shear on the van-der-Waals-driven rupture of a liquid-liquid interface in a stratified flow, and address the open question of shear effects in printing. In the absence of van der Waals forces and inertia, flow of two stratified immiscible liquids through a parallel plate channel is stable (Chen, 1995). But in the presence of van der Waals forces which drive dewetting, the interplay between shear and van-der-Waals-assisted rupture is not entirely obvious, especially in the nonlinear regime of film rupture. The results of the present work are thus expected to be useful both from the point of view of fundamental understanding of thin-film flows as well as for modeling applications such as printing or nanofluidic/microfluidic flows (Squires and Quake, 2005; Eijkel and van den Berg, 2005).

Studies on two-layer flows of thin liquid films bounded between two solid surfaces have focused on several phenomena that affect stability, such as van der Waals forces, thermocapillarity, chemical heterogeneity, and electric fields. Joo and Hsieh (2000) consider bounded two-layer flows with van der Waals forces as the driving force for rupture and thermocapillarity as the retarding force. Lenz and Kumar (2007a) have extended this work to include the effect of wettability gradients which come into play when at least one of the bounding solid surfaces is chemically patterned. In

such an arrangement, competition between two different length scales determines the mechanism of film rupture. One length scale is the system's natural length scale as mentioned earlier, and the other is the size of the non-wettable area in the domain. The work of Lenz and Kumar (2007a) and other prior analyses (Kargupta and Sharma, 2001, 2002a; Thiele et al., 2003) have shown that rupture and dewetting behavior depend strongly on the length scales of chemical heterogeneity. Merkt et al. (2005) described the dynamics of the liquid-liquid interface for a confined two-layer flow, focusing on gravity, thermocapillarity and electric fields as the causes for instability. Through two-dimensional nonlinear simulations, they studied the short- and long-time evolution of patterns such as holes, mazes, and drops.

Although the rupture of thin liquid films by van der Waals forces has been extensively investigated, there is typically no mean flow in the configurations considered. An exception is the study of Bielarz and Kalliadasis (2003), who examined single-layer thin-film flows near topographically patterned surfaces. They noted that whether or not topography is present, rupture of a film can be significantly delayed or even suppressed in the presence of a mean flow. However, a detailed examination of the mechanism responsible for this stabilization was not presented. It was also observed that rupture occurs only if the initial disturbance to the film height has sufficiently large amplitude. In contrast, infinitesimally small initial disturbances will grow and lead to rupture in the absence of a mean flow (Oron et al., 1997). The present work generalizes the aspects of the work of Bielarz and Kalliadasis (2003) concerned with flat surfaces by considering two-layer films and chemically patterned surfaces. It also presents a more detailed analysis of the mechanism by which a mean flow stabilizes van-der-Waals-driven rupture.

The rest of this paper is organized as follows. Section 2.2 describes the problem formulation, which closely follows that of Lenz and Kumar (2007a). A short summary of the numerical methods used and linear stability analysis results are also presented. As shall be observed later, the linear theory can be used to help explain the mechanisms of rupture behavior in the presence of imposed shear. Results of nonlinear simulations for rupture behavior on homogeneous surfaces are described in section 2.3, and those for chemically patterned surfaces (i.e. surfaces with wettability gradients) are given in section 2.4. In section 2.5, the model is applied to analyze the effect of shear in regimes relevant to lithographic printing and nanofluidic/microfluidic flows. Section 2.6 concludes the paper.

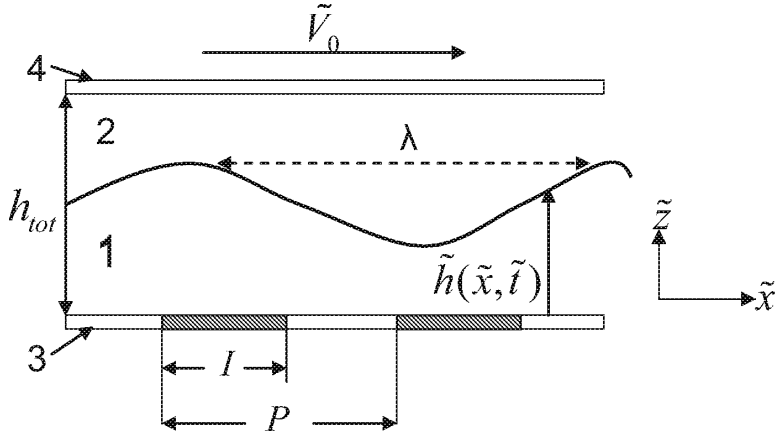

Figure 2.1: Schematic repesentation of the problem set up, with all labelled quantities in dimensional form.

2.2 Problem formulation

The problem setup is shown in figure 2.1. Two stratified Newtonian liquids, labeled 1 and 2, are flowing through a channel bounded by two solid surfaces, 3 and 4. The liquid-liquid interface is situated at a height $\tilde{h}(\tilde{x},\tilde{t})$ from surface 3. The lower surface is chemically patterned in such a way that intervals of length I can be wet by liquid 2 but not by liquid 1. Hereafter, these regions will be referred to as 'image' areas. The remaining surfaces on the substrate are neutral to both liquids, and are termed 'non-image' areas. Each non-image area has length $P - I$, where P represents the period size between two consecutive image areas. For modeling purposes, a transition region of non-zero width between the image and non-image areas is assumed (see section 2.2.1). In lithographic printing, liquid 2 would correspond to ink, liquid 1 would correspond to a barrier-like aqueous fountain solution, and the image areas would correspond to the places where ink placement is desired (Lenz and Kumar, 2007a). We will focus on the case where flow is driven by the top surface, which moves horizontally with a dimensional velocity $\tilde{V}_0$. Flow may also be driven by an imposed pressure gradient and a body force in the horizontal direction.

2.2.1 *Governing equations*

The gap between surfaces 3 and 4, h_{tot}, is assumed to be much smaller than λ, the wavelength of a typical perturbation of the interface. This assumption is the basis of the lubrication approximation and leads to considerable simplification of the

momentum conservation equations. Using a dimensionless parameter $\epsilon = h_{tot}/\lambda \ll 1$, the lengths and velocities in the problem are non-dimensionalized as follows:

$$x = \frac{\epsilon\tilde{x}}{h_{tot}}, \qquad z = \frac{\tilde{z}}{h_{tot}}, \qquad u_i = \frac{\tilde{u}_i\rho_1 h_{tot}}{\mu_1}, \qquad w_i = \frac{\tilde{w}_i\rho_1 h_{tot}}{\epsilon\mu_1}, \qquad V_0 = \frac{\tilde{V_0}\rho_1 h_{tot}}{\mu_1} \tag{2.1}$$

A tilde indicates a dimensional variable, and the subscript i denotes that the variable belongs to liquid i. The position variables in the horizontal and vertical directions are x and z, and the corresponding velocity components are u and w. The density is denoted by ρ and the viscosity by μ. The dimensionless velocity of the top surface is V_0. Note that V_0 plays the role of a Reynolds number, Re. Provided $\epsilon\mathrm{Re} \ll 1$, inertial effects may be neglected in the lubrication approximation (Oron et al., 1997).

Time and pressure are non-dimensionalized as follows:

$$t = \frac{\epsilon\tilde{t}\mu_1}{h_{tot}^2\rho_1}, \qquad (p_i, \phi_i) = (\tilde{p_i}, \tilde{\phi_i})\frac{\epsilon h_{tot}^2\rho_1}{\mu_1^2} \tag{2.2}$$

Here, p_i is the hydrodynamic pressure and ϕ_i is a potential associated with disjoining pressure.

The dimensional momentum balance for liquid i is given by

$$\rho_i(\partial_t\tilde{\mathbf{u}}_\mathbf{i} + \tilde{\mathbf{u}}_\mathbf{i}\cdot\nabla\tilde{\mathbf{u}}_\mathbf{i}) = -\nabla(\tilde{p_i} + \tilde{\phi_i}) + \mu_i\nabla^2\tilde{\mathbf{u}}_\mathbf{i} + \rho_i\tilde{\mathbf{B}} - \Delta\tilde{P}\mathbf{e}_x \tag{2.3}$$

In the above equation $\tilde{\mathbf{u}}_\mathbf{i}$ is the velocity vector of liquid i, $\tilde{\mathbf{B}} = \tilde{B}\mathbf{e}_x$ is a body force vector with units of force per unit mass, $\Delta\tilde{P}$ is an imposed pressure gradient, and $\mathbf{e}_x$ is the unit vector in x-direction. The momentum balance equation is simplified using the lubrication scalings [(4.1) and (4.2)] and dropping terms of order ϵ or smaller. The simplified equation is then considered together with the appropriate forms of the no-slip and no-penetration boundary conditions at the solid surfaces, tangential and normal stress balances at the liquid-liquid interface, kinematic condition at the interface, and continuity equation. Through a procedure similar to that in prior work (Lenz and Kumar, 2007a), an equation relating the dimensionless interface height, $h(x,t)$, and the flow rate of liquid 1, $\int_0^h u_1 \mathrm{d}z$, is obtained. This equation is solved simultaneously with the flow rate condition (2.5), described below, to yield an evolution equation for the interface height, $h(x,t)$.

In the absence of shear, body forces, and imposed pressure gradients, there is no mean flow in the x-direction. In their presence, however, each contributes to the mean flow rate and we denote these contributions in dimensionless form by Q_{shear},

Q_b, and Q_{pg}. For example, Q_{shear} can be evaluated by considering a steady two-layer flow with a flat interface through a parallel plate channel subject to shear:

$$Q_{shear} = \frac{V_0}{1 + h_0(\mu_r - 1)} \left[\frac{1}{2} + (\frac{h_0^2}{2} - h_0)(1 - \mu_r) \right], \tag{2.4}$$

where h_0 is the height of the liquid-liquid interface from the bottom plate (here, constant). Using a similar approach, one can also derive expressions for Q_b and Q_{pg}. These expressions are then substituted into the flow rate condition:

$$\int_0^h u_1 \mathrm{d}z + \int_h^1 u_2 \mathrm{d}z = Q_{shear} + Q_b + Q_{pg}; \tag{2.5}$$

note that the right-hand side is a constant.

The flow rate condition is used to obtain an evolution equation for the interfacial height $h(x,t)$ as mentioned earlier:

$$\begin{aligned} 0 = \partial_t h + \partial_x \Bigg\{ & \frac{[1 + (\mu_r - 1)h](1 - h)^3 h^3}{3 f(h, \mu_r)} [\partial_x (\phi_2\big|_{z=h} - \phi_1\big|_{z=h}) + 3\gamma \partial_x^3 h] \quad + \frac{\mu_r V_0 h^2}{2(h\mu_r - h + 1)} \\ & + \frac{B(h^4\mu_r - 4h^4 + 3h^4\rho_r - 6h^3\rho_r + 4h^3 + 12h^2\rho_r)}{12(h\mu_r - h + 1)} \\ & + \frac{\Delta\hat{P}(h^4 - h^4\mu_r + 6h^3\mu_r - 4h^3 - 6h^2\mu_r + 3h^2)}{12\mu_r(h\mu_r - h + 1)} \Bigg\}. \end{aligned} \tag{2.6}$$

with $f(h, \mu_r)$ given by:

$$f(h, \mu_r) = h^4\mu_r^2 - (2h^4 - 4h^3 + 6h^2 - 4h)\mu_r + (h - 1)^4. \tag{2.7}$$

Here γ is the dimensionless interfacial tension, and B and $\Delta\hat{P}$ are the dimensionless body force and the imposed pressure gradient, defined as:

$$\gamma = \frac{\epsilon^3 \tilde{\gamma} \rho_1 h_{tot}}{3\mu_1^2}, \qquad B = \frac{\tilde{B}\rho_1^2 h_{tot}^3}{\epsilon \mu_1^2}, \qquad \Delta\hat{P} = \frac{\Delta\tilde{P}\epsilon h_{tot}^2 \rho_1}{\mu_1^2}. \tag{2.8}$$

In the absence of shear, imposed pressure gradients, and body forces ($V_0 = 0$, $\Delta\hat{P} = 0$, $B = 0$), (3.3) reduces to the same evolution equation as derived by Lenz and Kumar (2007a). On the right-hand side of (3.3), the terms within the spatial derivative represent contributions from the disjoining pressure, surface tension, shear, body force and pressure gradient respectively. The potentials ϕ_i for the disjoining

pressure are represented by:

$$\phi_1\Big|_{z=h} = \frac{A_1}{h^3}, \qquad \phi_2\Big|_{z=h} = \frac{A_2}{(1-h)^3}, \tag{2.9}$$

where A_1 and A_2 are dimensionless constants. The above expressions have also been used by Joo and Hsieh (2000) in their study of two-layer flows. Note that A_1 and A_2 will depend on the Hamaker constants characterizing the interactions between materials 1, 2, 3, and 4 (Kumar and Matar, 2004; Maldarelli et al., 1980; Israelachvili, 1992, 1972). Using (2.9), the contribution from disjoining pressure in (3.3) can be explicitly written in terms of A_1 and A_2 as:

$$\partial_x(\phi_2\big|_{z=h} - \phi_1\big|_{z=h}) = 3\partial_x h\left[\frac{A_2}{(1-h)^4} + \frac{A_1}{h^4}\right] + \frac{\partial_x A_2}{(1-h)^3} - \frac{\partial_x A_1}{h^3}. \tag{2.10}$$

Here $\partial_x A_1$ and $\partial_x A_2$ denote wettability gradients which arise when the surfaces 3 and 4, respectively, are chemically patterned. If we take the single layer limit $\mu_r \to 0$ in (3.3), assume A_1 is constant, and set $\phi_2\big|_{z=h} = 0$, (3.3) reduces to the evolution equation for a single liquid layer. That equation was studied in previous works (Williams and Davis, 1982; Burelbach et al., 1988) in the absence of pressure gradients, body forces, and shear. The results presented and discussed in this work are all for the case $\phi_2\big|_{z=h} = 0$.

Nonlinear simulations were performed for the two-layer case by Lenz and Kumar (2007a) in the absence of shear, pressure gradients, and body forces ($V_0 = 0$, $\Delta\hat{P} = 0$, $B = 0$) for both homogeneous surfaces ($\partial_x A_1 = 0,\ \partial_x A_2 = 0$) and for the case where wettability gradients exist ($A_2 = 0,\ \partial_x A_1 \neq 0$). In the present work, we extend those simulations paying specific attention to the effect of shear ($V_0 \neq 0$, $\Delta\hat{P} = 0$, $B = 0$). We expect that the effects of body forces ($B \neq 0$) and imposed pressure gradients ($\Delta\hat{P} \neq 0$) would follow the same trends as the effects of shear.

For homogeneous bounding surfaces (constant A_1 and A_2) with $\Delta\hat{P} = B = 0$, (3.3) reduces to the following:

$$0 = \partial_t h + \partial_x\left\{\frac{[1+(\mu_r-1)h]}{f(h,\mu_r)}\left[\partial_x h\left(A_2\frac{h^3}{1-h} + A_1\frac{(1-h)^3}{h}\right) + \gamma(1-h)^3h^3\partial_x^3 h\right] + \frac{\mu_r V_0 h^2}{2(h\mu_r - h + 1)}\right\} \tag{2.11}$$

The term within the braces in (2.11) is the flow rate of liquid 1 and it has components due to wettability (the term involving constants A_1 and A_2), capillarity (the term involving surface tension γ), and shear (the term involving velocity V_0).

For heterogeneous surfaces (variable A_1 and A_2), the gradients of A_1 and A_2 will appear in the evolution equation to capture the effect of wettability gradients. For this case, if we set $\phi_2\big|_{z=h} = 0$, the evolution equation (3.3) becomes:

$$0 = \partial_t h + \partial_x \left\{ \frac{[1+(\mu_r-1)h](1-h)^3 h^3}{3f(h,\mu_r)} \left[3\partial_x h \left(\frac{A_1}{h^4} \right) - \frac{\partial_x A_1}{h^3} + 3\gamma \partial_x^3 h \right] + \frac{\mu_r V_0 h^2}{2(h\mu_r - h + 1)} \right\} \tag{2.12}$$

To describe the gradient of A_1 we use the arctangent function employed by Lenz and Kumar (2007a):

$$A_1(x) = \frac{A_1^{Im}}{\pi} \left[\arctan\left(\frac{x + I/2}{\delta}\right) - \arctan\left(\frac{x - I/2}{\delta}\right) \right]. \tag{2.13}$$

In the above equation, A_1^{Im} is the value of A_1 in the image area, I denotes width of the image area, and δ is the width of the transition region between the image and non-image areas. Smaller values of δ imply steeper wettability gradients. Motivated by the discussion in prior work (Lenz and Kumar, 2007a) regarding appropriate values for δ within the lubrication approximation, we use $\delta = 0.01$ in our simulations.

2.2.2 *Numerical methods*

Simulations were performed using (2.11) for homogeneous surfaces and (2.12) for heterogeneous surfaces. Differential Algebraic System Solver (DASSL) was used for time integration because it adjusts time steps automatically according to the stiffness of the problem. Spatial discretization was done using fourth-order centered finite differences. About 400-500 spatial nodes per the most dangerous wavelength (see section 2.2.3) were used to obtain results independent of node spacing, similar to Ref. [7]. Mass conservation during the simulation was maintained by ensuring that the average interface height varied by less than 0.02% at all times during the simulation. Rupture was declared when the film thinned below a minimum height of 10^{-3}.

A typical perturbation of the interface consists of many different wavelengths, out of which one will grow the fastest. This is known as the most dangerous wavelength, λ_{md}. To incorporate a typical disturbance, the initial condition in all cases was chosen to be a perturbation consisting of a series of Fourier modes with random phases and amplitudes, with a maximum amplitude of 0.1. The range of wavelengths of these waves varied from $3\lambda_{md}$ to $\lambda_c/100$, where λ_c is the wavelength for which the growth rate from linear stability analysis (section 2.2.3) is zero. The random initial condition resulted in the same rupture behavior when different random-number-generator seeds were used. For heterogeneous surfaces ($I \neq P$ in figure 2.1), the λ_{md} used to generate the initial conditions was that associated with the corresponding homogeneous case ($I = P$). For all simulations, the domain length was taken to be $3\lambda_{md}$.

2.2.3 *Linear stability analysis*

The effect of small amplitude perturbations on the system for the case of homogeneous surfaces can be studied using a standard linear stability analysis. Applying this to (2.11) yields the following expression for the growth rate of perturbations, α:

$$\alpha = \frac{k^2[h_0(\mu_r - 1) + 1]}{f(h_0, \mu_r)} \left[A_1 \frac{(1-h_0)^3}{h_0} + A_2 \frac{h_0^3}{1-h_0} - k^2 \gamma h_0^3 (1-h_0)^3 \right]$$

$$+ i \ \frac{\mu_r k V_0 h_0 (h_0 \mu_r - h_0 + 2)}{2(h_0 \mu_r - h_0 + 1)^2}. \tag{2.14}$$

Here k is a dimensionless real-valued wavenumber of the perturbations and h_0 is the dimensionless initial height of the interface. The growth rate is complex, indicating that the system admits traveling waves. The imaginary component of the growth rate gives the wave speed which, in (4.14), is arising from effect of shear alone. At the same time the real part of the growth rate, which gives the magnitude of the growth rate, is unaffected by shear. The critical wavenumber, k_c, is defined as that wavenumber for which the perturbations neither grow nor decay. This is obtained by setting the real part of the growth rate to zero. Similarly, the most dangerous wavenumber, $k_{md} = 2\pi/\lambda_{md}$, is calculated by setting $\frac{\partial \alpha}{\partial k} = 0$. The results are:

$$k_c = \left[\frac{1}{\gamma} \left(\frac{A_1}{h_0^4} + \frac{A_2}{(1-h_0)^4} \right) \right]^{1/2}, \tag{2.15}$$

$$k_{md} = k_c / 2^{1/2}. \tag{2.16}$$

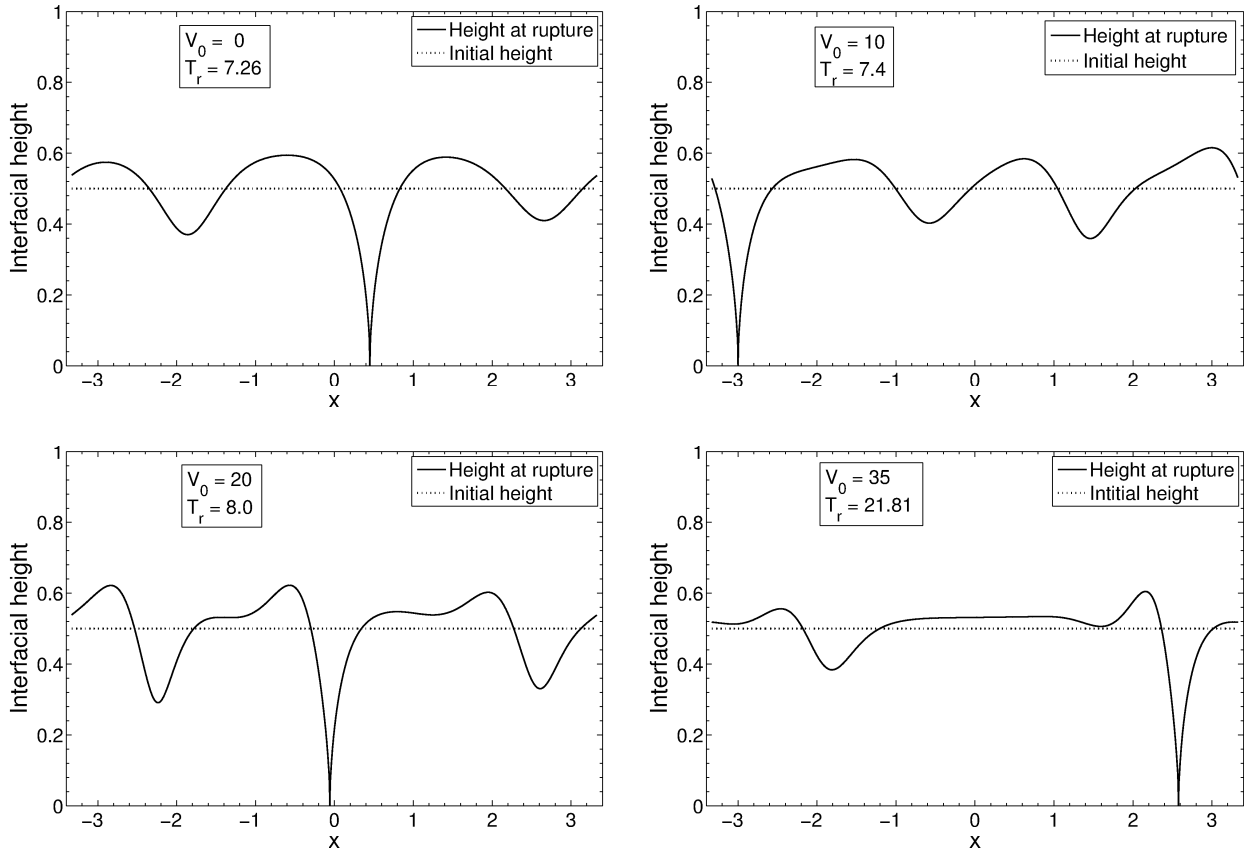

Figure 2.2: Initial and rupture-time interface profiles for different shear velocities when $A_1 = 1$, $A_2 = 0$, $\mu_r = 1$, $h_0 = 0.5$, and $\gamma = 1$.

2.3 Rupture behavior on homogeneous surfaces

In this section, results of nonlinear simulations of (2.11) are discussed. This is the case of homogeneous surfaces and corresponds to $I = P$ in figure 2.1. The attraction of the liquid-liquid interface to surfaces 3 and 4 is determined by the relative values of A_1 and A_2.

2.3.1 *Delay in rupture and parametric study*

Figure 2.2 shows height profiles of the interface at $t = 0$ and $t = T_r$, the rupture time, for four different shear velocities ($V_0 = 0$, 10, 20, and 35). Attraction of the interface to the bottom surface alone is being considered ($A_1 = 1$, $A_2 = 0$). Both liquids 1 and 2 are assumed to have equal viscosities ($\mu_r = 1$) and the liquid layers are of equal initial thickness ($h_0 = 0.5$). The interface is assumed to have a dimensionless surface tension of unity ($\gamma = 1$). It is seen that rupture occurs in all these cases, with

rupture being progressively delayed with increasing imposed shear velocities. The interface profile is seen to become more distorted as the shear velocity is increased. For $V_0 > 35$, rupture is not observed within the time frame of the simulations (dimensionless time $t = 50$). It was found that for a given set of problem parameters (h_0, γ, μ_r, A_1, A_2), there always exists a certain critical velocity at which this suppression of rupture occurs. Although values of A_1 smaller than unity are physically more realistic (see Table 1), using such values will not change the qualitative results of our simulations. Smaller values of A_1 will simply cause an increase in the rupture time, and thus a reduction in the critical velocity needed to suppress rupture.

The non-ruptured parts of the interface profiles for $V_0 = 20$ and $V_0 = 35$ resemble interface profiles obtained by Thiele et al. (2001, 2002) in their studies of drops sliding down inclined planes. The profiles in these regions have a flat shape with a capillary ridge at the downstream end. Although the model studied by Thiele et al. is different from ours (it does not allow for film rupture and is based on diffuse-interface theory), the common element appears to be an interaction between intermolecular forces and shear. The former tends to distort the interface (leading to rupture or drop formation) while the latter tends to convect and steepen interfacial perturbations.

Figure 2.3 shows the rupture time as a function of the shear velocity for various viscosity ratios, μ_r, on a natural logarithmic scale, with $A_1 = 1$, $A_2 = 0$, $h_0 = 0.5$, and $\gamma = 1$. For $\mu_r = 0.5$ and $\mu_r = 1$, we see that there is a steep increase in rupture time at finite shear velocities, virtually resulting in suppression of rupture. The critical velocity of suppression of rupture decreases as μ_r increases for $0.1 < \mu_r < 3$, and increases thereafter for $\mu_r > 3$. This non-monotonic behavior is explained in section 2.3.2. We note that the critical velocity for suppression of rupture will decrease as the initial interface height h_0 is increased. In the absence of attraction to the top surface ($A_2 = 0$), increasing h_0 also increases the rupture time as the van der Waals forces, proportional to A_1/h^3, become weaker.

2.3.2 *Mechanisms*

As mentioned in section 2.2.1, the flow rate in liquid 1 has components associated with wettability, capillarity, and shear. Besides, (2.11) suggests that flow rate components whose gradients are positive assist rupture, whereas those gradients are negative oppose rupture.

Figure 2.4 shows the variation of gradients of flowrate components at each instant of time at the location of minimum interfacial height for $V_0 = 25$ with parameters $A_1 = 1$, $A_2 = 0$, $h_0 = 0.5$, $\gamma = 1$, and $\mu_r = 1$. Also shown is the overall gradient.

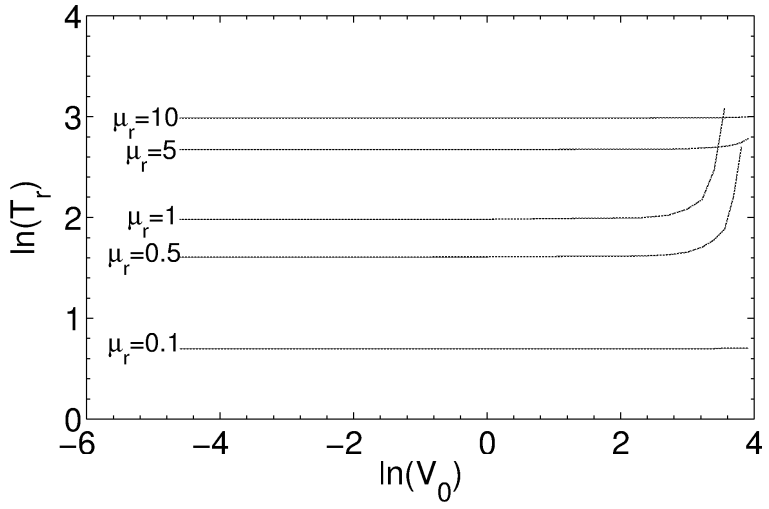

Figure 2.3: Effect of shear on rupture time for various viscosity ratios when $A_1 = 1$, $A_2 = 0$, $\mu_r = 1$, $h_0 = 0.5$, and $\gamma = 1$. Suppression of rupture occurs at a critical velocity at which there is a steep increase in rupture time (the point where the curves become vertical). This critical velocity decreases as μ_r increases for $0.1 < \mu_r < 3$, and increases thereafter for $\mu_r > 3$.

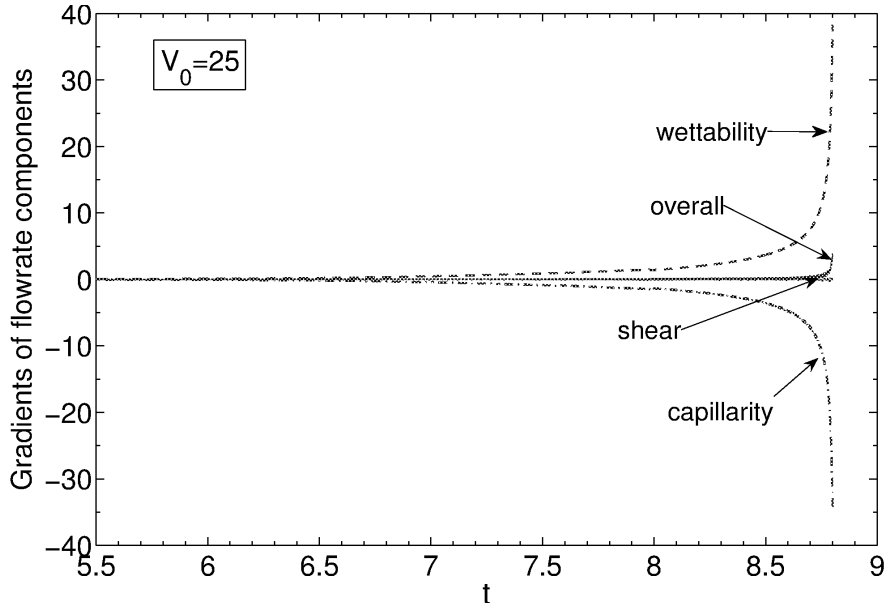

Figure 2.4: Gradients of flowrate components at the rupture location plotted against time, t for $V_0 = 25$. In both plots $A_1 = 1$, $A_2 = 0$, $h_0 = 0.5$, $\gamma = 1$, and $\mu_r = 1$. Rupture occurs at $t = 7.26$ for $V_0 = 0$ and at $t = 8.81$ for $V_0 = 25$.

For $V_0 = 0$, the case of no imposed shear ($T_r = 7.26$), the results are found to be very similar to those in Figure 2.4, indicating that there is a competition between wettability and capillarity as the rupture time is approached. While wettability assists rupture with a positive gradient, capillarity has a negative gradient and it opposes rupture by driving liquid towards the rupture location. When shear is incorporated, with $V_0 = 25$, rupture occurs at $t = 8.81$. Recall from section 2.3.1 that for the given set of parameters, rupture is not suppressed until $V_0 > 35$. For $V_0 = 25$ it is still the same competition between wettability and capillarity that determines rupture. The shear component has approximately zero gradient until rupture is approached. Very close to the rupture time, the gradient of the shear component becomes positive at the rupture location, indicating that liquid 1 is being driven away on either side from the location of rupture. Yet the contribution of shear in assisting rupture is far smaller than that of wettability, and is present for a shorter period. These findings are consistent with the self-similar nature of the dynamics close to rupture, where shear is predicted to become negligible relative to wettability and capillarity (Bielarz and Kalliadasis, 2003).

A schematic describing the mechanism for rupture delay is outlined in figure 2.5. When shear is imposed, it propagates a traveling wave along the liquid-liquid interface. Perturbations along the interface move in the direction of imposed shear even as rupture is being assisted by van der Waals forces. They also steepen due to the hh_x term that would arise from the shear term in (3.3). Consequently, when the perturbation at the location of minimum interfacial height moves to a new location, the interface height at the original rupture location goes up, and van der Waals forces are weakened here. Thus, at any instant, the fluid element at the location of minimum interface height moves to a higher position on the interface. A new fluid element at a new location having the minimum interface height becomes the most susceptible to rupture. It is, of course, harder for rupture to occur when the fluid element at the lowest point on the interface is being constantly moved to a higher location, compared to the case where the fluid element at the lowest point on the interface remains at the same location. The final rupture is a consequence of the flow due to wettability, which drives liquid away from either side of the rupture location. This interplay between shear, wettability and capillarity is very much in the nonlinear regime of flow. When V_0 exceeds a critical velocity, van der Waals forces are unable to cause rupture.

The above mechanism can be analyzed in light of the results from linear stability analysis (section 2.2.3). The growth rate obtained from linear stability analysis has both a real and an imaginary component, indicating the presence of a traveling

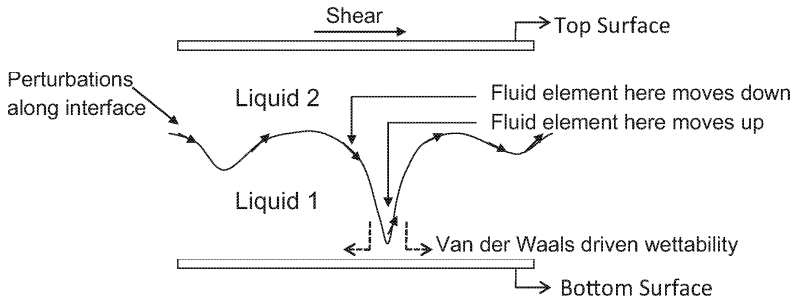

Figure 2.5: Schematic showing the mechanism by which shear delays rupture. Shear propagates a traveling wave, causing a fluid element at the location of minimum interface height to move to a higher position on the interface. Van-der-Waals-assisted rupture wins so long as V_0 is less than a critical velocity.

wave. The imaginary component of the growth rate in (4.14) represents the angular frequency ω of the wave, which is proportional to V_0, as is the wave speed. Thus, increasing the imposed shear velocity increases the wave speed and causes interfacial perturbations to travel faster. The time period of the wave can be obtained using equation (4.14):

$$T_{wave} = \frac{2\pi}{\omega} = \frac{2\pi}{\mathrm{Im}(\alpha)} = \frac{4\pi(h_0\mu_r - h_0 + 1)^2}{h_0\mu_r V_0 k_{md}(h_0\mu_r - h_0 + 2)}, \tag{2.17}$$

where k_{md} is given by (2.16). In general, our calculations suggest that rupture is delayed significantly when $T_{wave}/T_{r0} \ll 1$, where T_{r0} is the rupture time in the absence of shear. From this condition it follows that the critical velocity, V_c for suppression of rupture is of the order:

$$V_c \sim \frac{(h_0\mu_r - h_0 + 1)^2}{h_0\mu_r k_{md}(h_0\mu_r - h_0 + 2)T_{r0}} \tag{2.18}$$

Figure 2.6 shows the variation of T_{wave} with the viscosity ratio μ_r for $V_0 = 20$, $A_1 = 1$, $A_2 = 0$, $h_0 = 0.5$, and $\gamma = 1$. This curve exhibits a minimum at $\mu_r = 3$, explaining the non-monotonic variation of the critical velocity with the viscosity ratio in figure 2.3. It can also be shown that T_{wave} decreases with increasing h_0, which is consistent with the decrease in critical velocity with increasing h_0 observed in nonlinear simulations.

Figure 2.7 shows the time variation of the minimum interface height at various shear velocities for the case where $A_1 = 1$, $A_2 = 0$, $\mu_r = 1$, $\gamma = 1$, and $h_0 = 0.5$. The delay in rupture due to shear, and eventual suppression of rupture for $V_0 = 40$, is seen. For $V_0 = 40$, the interface height decreases to $\sim 80\%$ of its original value. For $t > 32$,

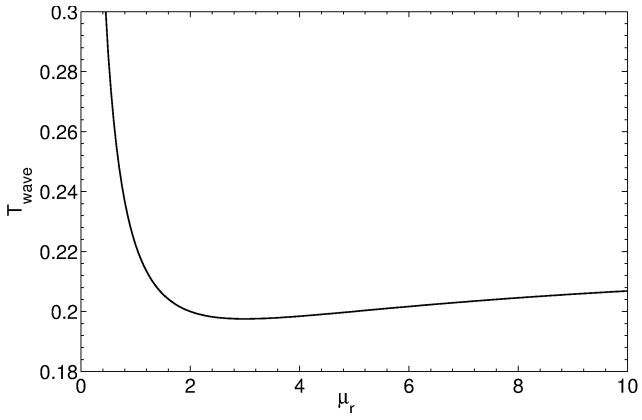

Figure 2.6: Time period of the interface wave versus the viscosity ratio for $V_0 = 20$. The curve exhibits a minimum at $\mu_r = 3$. Here $A_1 = 1$, $A_2 = 0$, $h_0 = 0.5$, and $\gamma = 1$. This curve explains the trend in figure 2.3 where the critical velocity for suppression of rupture also exhibits a minimum.

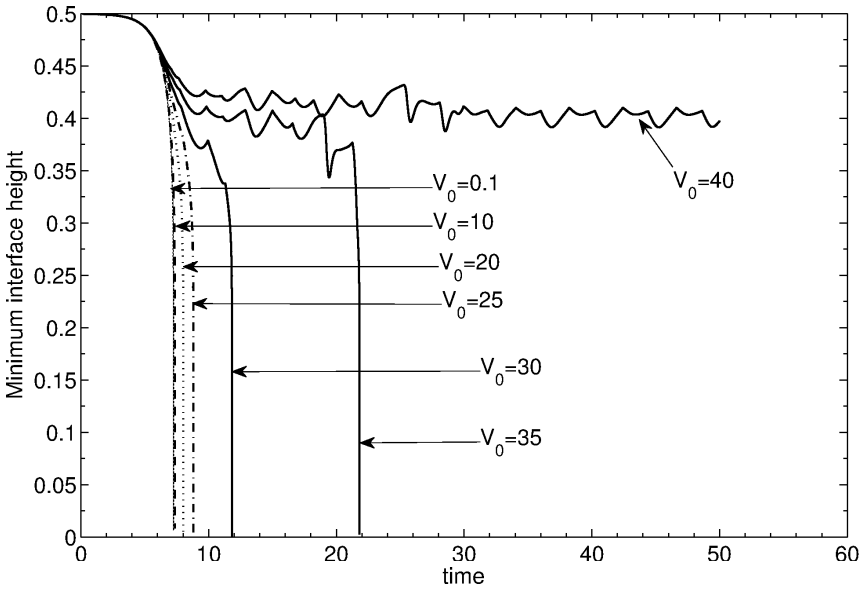

Figure 2.7: Minimum interfacial height at various velocities. Here $A_1 = 1$, $A_2 = 0$, $\mu_r = 1$, $\gamma = 1$, and $h_0 = 0.5$ in all cases. For $V_0 = 40$ rupture is suppressed, and the minimum interface height oscillates around $h = 0.4$.

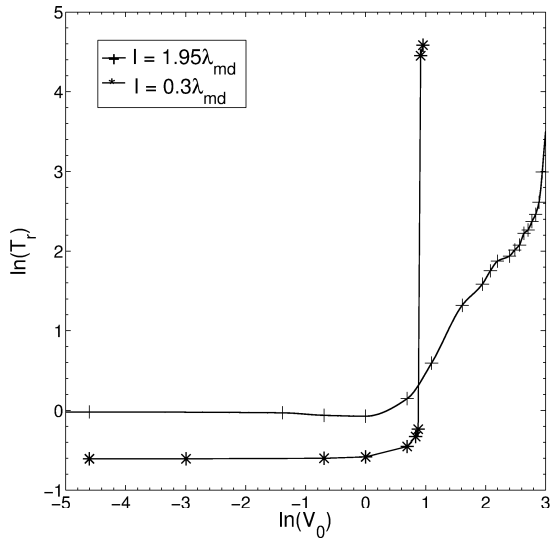

Figure 2.8: Effect of imposed shear on rupture time in the case of heterogeneous surfaces for image sizes $I = 1.95\lambda_{md}$ and $I = 0.3\lambda_{md}$. In both cases $A_2 = 0$, $h_0 = 0.5$, $\gamma = 1$, and $\mu_r = 1$.

the minimum interface height oscillates periodically. A Fourier transform of these oscillations shows that the dominant frequency of these oscillations is about 0.2% of the frequency of interface waves obtained from linear theory (2.17). The difference in these frequencies is perhaps a result of nonlinear evolution of perturbations. Within the time scale of the simulations, wettability-driven flow is dominated by the opposing capillary forces and rupture is prevented.

2.4 Rupture behavior in presence of wettability gradients

In this section, results for surfaces with wettability gradients are presented and discussed based on nonlinear simulations of (2.12). Such surfaces correspond to the case of $I \neq P$ in figure 2.1, and we use (2.13) for A_1 while setting $A_2 = 0$. In (2.13) we set $A_1^{Im} = 1$ and $\delta = 0.01$.

Figure 2.8 shows the effect of imposed shear on the rupture time for two different image sizes, $I = 1.95\lambda_{md}$ and $I = 0.3\lambda_{md}$, with $h_0 = 0.5$, $\gamma = 1$ and $\mu_r = 1$. As in the case of homogeneous surfaces, a delay of rupture and suppression beyond a critical velocity within the simulation time scale is observed. For the image size $I = 1.95\lambda_{md}$, the initial and rupture-time interfacial height profiles for four different

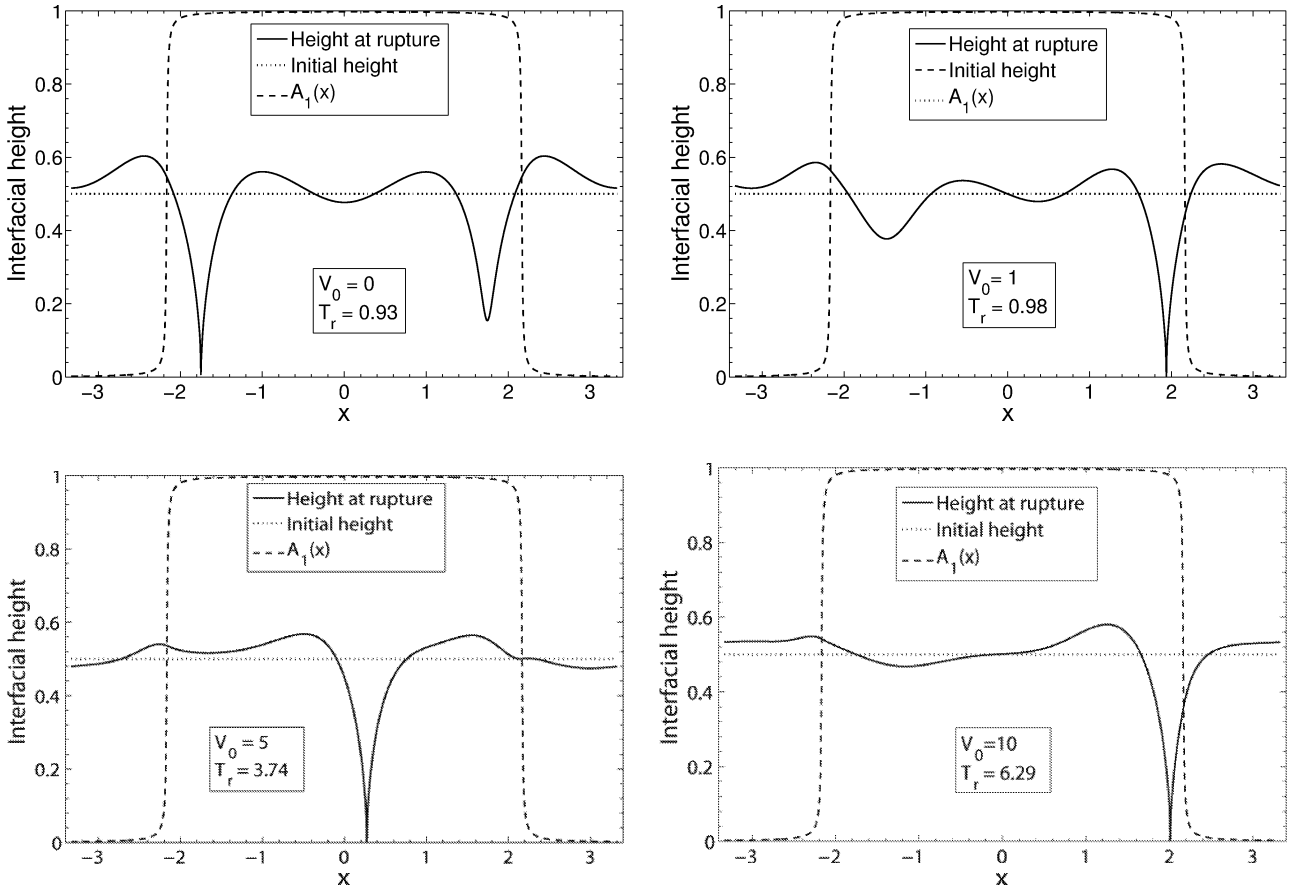

Figure 2.9: Initial and rupture-time interfacial height profiles on heterogeneous surfaces for different imposed velocities when $I = 1.95\lambda_{md}$, $A_2 = 0$, $h_0 = 0.5$, $\gamma = 1$, and $\mu_r = 1$.

velocities; $V_0 = 0$, $V_0 = 1$, $V_0 = 5$, and $V_0 = 10$, are shown in figure 2.9. For the case of no shear ($V_0 = 0$), rupture occurs at the two ends of the image area. When shear is imposed ($V_0 = 1, V_0 = 5, V_0 = 10$), a mean flow to the right (positive x-direction) is introduced and rupture now occurs primarily at one location only. The dimensionless velocity at which this effect is prominently seen first is $V_0 = 1$. Varying the initial condition by changing the random-number-generator seed produced no significant changes in the interface profile at rupture. To confirm that the change in two rupture points to one is a result of the mean flow and not the initial conditions, simulations were also performed in which the direction of the imposed velocity V_0 was reversed. This resulted in interface profiles which are mirror images around $x = 0$ of those in figure 2.9.

Figure 2.10 shows the flowrate components plotted against the domain length at different stages of rupture for $V_0 = 0$ and image size $I = 1.95\lambda_{md}$. The other

parameters are same as those in figure 2.9. From (2.12), we see that there are now four flow rate components: wettability (A_1 term), capillarity (γ term), wettability gradients ($\partial_x A_1$ term) and shear (V_0 term). Wettability gradients cause the layer of fluid 1 to thin locally near the edges of the image area. These are represented by the flowrate spikes in figure 2.10. Capillary forces oppose rupture by driving liquid onto the image area. As the film is thinned further, the wettability contribution increases near these image edges, and that of wettability gradients decreases. Hereafter, there is a competition between wettability and capillary forces, in which wettability succeeds and causes rupture of the interface (Lenz and Kumar, 2007a).

Figure 2.11 shows plots similar to those in figure 2.10 but with $V_0 = 10$. Wettability gradients drive liquid 1 from the left end of the image to the left, and from the right end of the image to the right. Now there is a mean flow in the positive x-direction due to imposed shear, so that shear tends to reinforce the gradient-driven film-thinning at the right, and oppose it at the left. Consequently, we see longer spikes in wettability gradients at the right and shorter spikes at the left when rupture proceeds from 50% to 90% completion. The mechanism by which shear delays the rupture is the same as that illustrated in figure 2.5. As in the case of $V_0 = 0$, competition between wettability gradients and opposing capillary forces determines film thinning for a major part of rupture. Eventually wettability-driven flows cause rupture, but with a delay.

When the image size is reduced to $I = 0.3\lambda_{md}$, the image is narrow enough to cause cooperative film-thinning from both ends of the image, so that rupture occurs at the center of the image for $V_0 = 0$. As V_0 is increased, the rupture time increases gradually for $0 < V_0 < 2.4$, but beyond this velocity range the rupture time increases sharply from $T_r = 0.72$ for $V_0 = 2.3$ to $T_r = 97.92$ for $V_0 = 2.6$, as is shown in figure 2.8. Rupture is thus suppressed for $V_0 > 2.6$ within the time scale of the simulations. Due to the narrow image size, the film is not thinned sufficiently by wettability gradients for wettability-driven flows to take over and cause eventual rupture.

2.5 Application to printing and nanofluidics/ microfludics

As mentioned in section 2.1, one of the motivations of this study is to examine the effect of shear in a lithographic printing nip. In the lithographic printing process, a highly viscous oil-based ink is transferred from a roller onto a chemically patterned

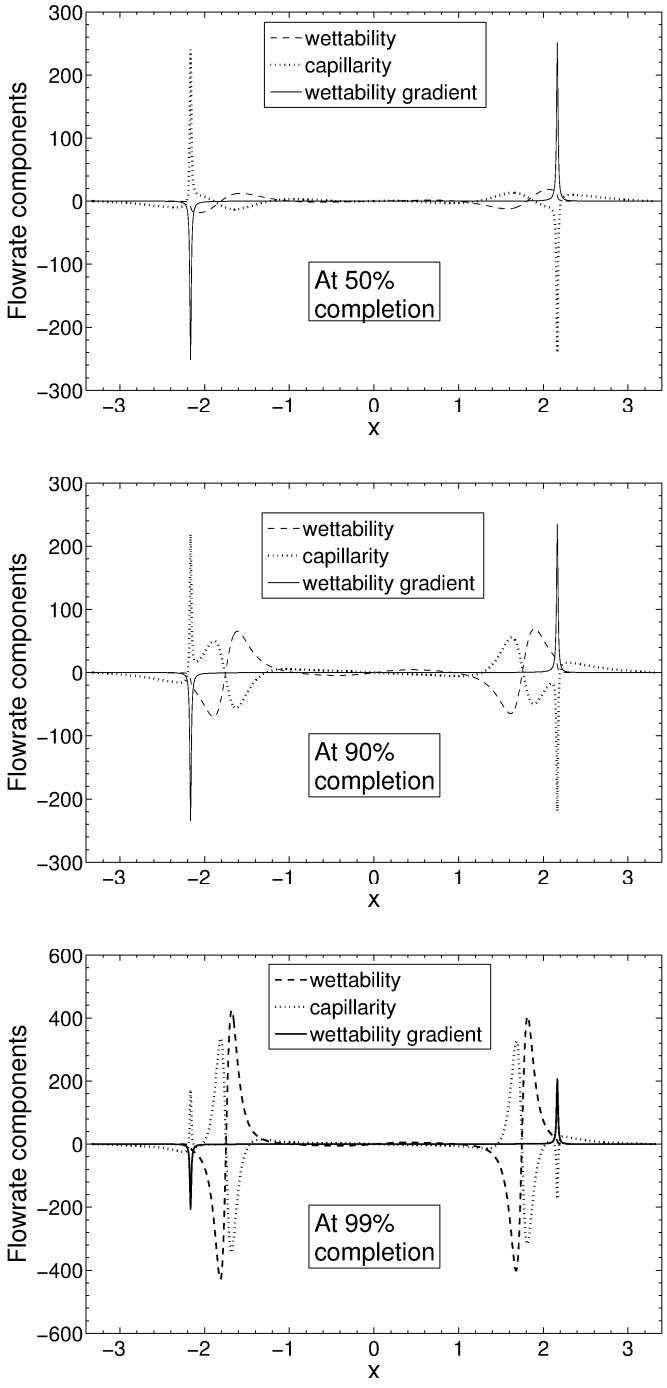

Figure 2.10: Flowrate components versus x at 50% completion, 90% completion and 99% of the time to rupture when $V_0 = 0$ and $I = 1.95\lambda_{md}$. Here $A_2 = 0$, $h_0 = 0.5$, $\gamma = 1$, and $\mu_r = 1$.

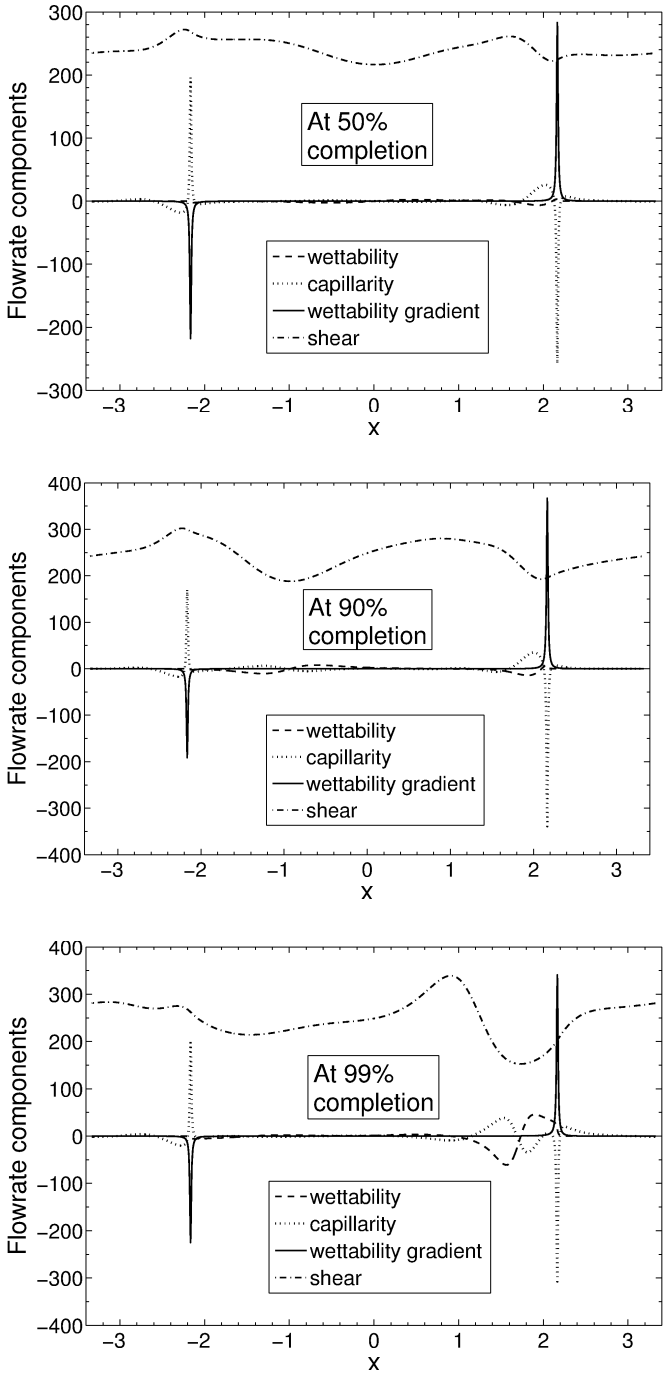

Figure 2.11: Flowrate components at 50% completion, 90% completion and 99% completion of the time to rupture when $V_0 = 10$ and $I = 1.95\lambda_{md}$. Here $A_2 = 0$, $h_0 = 0.5$, $\gamma = 1$, and $\mu_r = 1$.

printing cylinder surface through a thin barrier film of water-like fountain solution. Although the ink-carrying roller and the printing cylinder have the same linear velocities to begin with, deformation of the more resilient ink-roller surface over time can cause relative motion between the printing cylinder and the roller surfaces. Typical shear rates that result are estimated to be of the order of 10^4 s^{-1} [Ref. 6].

As was done by Lenz and Kumar (2007a), it is useful to idealize the ink roller and cylinder surfaces as flat plates, given that the gap between them is much smaller than their respective radii. This leads to the configuration shown in figure 1, with the water-like fountain solution as liquid 1 and the oil-based ink as liquid 2. Typical parameter values associated with lithographic printing are given in table 1 [Ref. 6]. Using these values, simulations similar to those in section 2.3 were performed (For simplicity, we consider the case where the bottom surface is chemically homogeneous.) For a shear rate of $\dot{\gamma} = 10^4$ s^{-1} and an image size of ~ 1 μm, a rupture time of 130 μs is obtained. In dimensionless terms, this turns out to be $T_r = 2.54$. For the parameter values used, it is easily verified that the Reynolds number $\mathrm{Re} = \tilde{h}_i \tilde{V}_0 \tilde{\rho}_i / \tilde{\mu}_i$ is much smaller than unity in each liquid, where $\tilde{h}_i$ is the initial thickness of liquid layer i. This allows neglect of inertial effects in the lubrication approximation (for which one can have $\mathrm{Re} \sim 1$ at most). For the long-wave approximation used here to be valid, the surface slopes need to be small as well. In the absence of imposed shear, the rupture time is found to be 129 μs under these conditions, which is about the same as that when the shear rate is $\dot{\gamma} = 10^4$ s^{-1}. The rupture time in the absence of shear is equivalent to a rupture rate of $\sim 8 \times 10^3$ s^{-1}, which is close to estimated shear rates in lithographic printing. Thus, at first glance, one might anticipate that shear will influence the rupture time significantly since the rupture rate is comparable to the shear rate. However, our more detailed analysis shows that the shear rates in lithographic printing are not large enough to cause significant changes in rupture behavior. This implies that the process by which ink displaces fountain solution can be well understood without accounting for imposed shear.

In principle, there could be other physical systems such as nanofluidic/microfluidic channels, where the effects of shear significantly influence the rupture time. Consider the case of two liquid layers each having an initial thickness of 100 nm, with an interfacial tension of $\tilde{\gamma} = 20$ mN/m, and having viscosity ratios $\mu_r = 10$, 1, and 0.1 with $\mu_1 = 10^{-3}$ Pa.s. Assuming the Hamaker constants to be $A_1 = 5 \times 10^{-20}$ J and $A_2 = 0$, we obtain the fastest growing wavelength to be ~ 32 μm, or in dimensionless terms, $k_{md} \sim 38$ from linear stability analysis. The above calculation results in $\epsilon = 6 \times 10^{-3}$, suggesting that the lubrication approximation is valid for

Table 2.1: Typical parameter values relevant to printing (MacPhee, 1998)

Quantity	Dimensionless value	Dimensional value
Hamaker constant 1	$A_1 = 2 \times 10^{-7}$	$\tilde{A_1} = 10^{-13}$ erg
Hamaker constant 2	$A_2 = 0$	—
Water-layer viscosity, μ_1	—	0.01 poise
Ink-layer viscosity, μ_2	—	35-400 poise
Viscosity ratio, μ_2/μ_1	$\mu_r = 10000$	—
Interfacial tension	$\gamma = 2.5 \times 10^{-5}$	9 dyne/cm
Ink-layer thickness in the nip	—	1 μm
Water-layer thickness in the nip	—	10 nm
Initial interface height	$h_0 = 0.01$	—
Shear rate	$V_0 = 0.01$	$\dot{\gamma} = 10^4$ s^{-1}
Rupture time	$T_r = 2.54$	$\tilde{T_r} = 1.30 \times 10^{-4}$ s

this system. Using these values, we performed simulations for increasing velocities of the top plate. Figure 2.12 shows the dimensional rupture time plotted against the speed of the top plate for different viscosity ratios. As before, rupture is delayed when the speed of the top plate is increased, and suppressed when the speed is sufficiently large. The typical speeds at which the imposed shear begins to have a pronounced effect on the rupture time is in the range 5 μm/s - 25 μm/s, which is well within the operating regime of nanofluidic/microfluidic devices (Squires and Quake, 2005; Eijkel and van den Berg, 2005). As for the printing regime, here too it is easily verified that Re $\ll 1$, and hence the lubrication approximation may be used.

2.6 Conclusions

We have studied the effect of shear on van-der-Waals-driven rupture of a confined bilayer thin-film flow between parallel horizontal surfaces. We have considered the cases where the surfaces are homogeneous as well as where one of the surfaces is chemically patterned, to account for wettability gradients. A one-dimensional nonlinear evolution equation incorporating shear is derived to desribe the height of the liquid-liquid interface.

Linear stability analysis reveals that growth rate of perturbations of the interface has an imaginary component in the presence of shear, which suggests that shear leads to traveling waves. The speed of these waves is proportional to the shear velocity. Nonlinear simulations show delay in rupture when shear is imposed, and suppres-

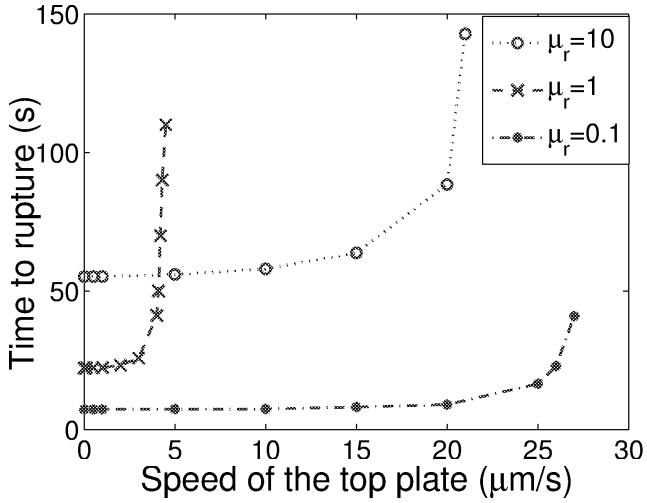

Figure 2.12: Effect of shear on rupture time in bounded two-layer flows computed using parameters typical of microfluidic flows. Here μ_r is the ratio of top layer viscosity to bottom layer viscosity.

sion of rupture occurs beyond a critical velocity. When rupture is suppressed, the minimum interface height oscillates periodically with time. We have identified a possible mechanism to explain shear-induced delay in rupture. As traveling waves are admitted along the interface, perturbations along the interface continuously move in the direction of imposed shear, carrying with them the fluid elements at the location of minimum interface height. These perturbations also steepen, increasing the interfacial height at the location of the original minimum height. Consequently, van der Waals forces are weakened at the original location which was most susceptible to rupture. A new fluid element at a new location then becomes most susceptible to rupture. Competition between wettability-driven flows and capillary forces determine the eventual rupture for flow on homogeneous surfaces. When wettability gradients are introduced, rupture is initiated by these gradients, both in presence and absence of shear, and later taken over by wettability-driven flows. Suppression of rupture requires the wave period to be much less than the rupture time in the absence of shear.

The present work enriches fundamental understanding of thin-film rupture by investigating the contribution of mean flow in bounded two-layer flows, which was not explored in earlier work (Lenz and Kumar, 2007a). Through nonlinear simulations and linear stability analysis, a closer examination of the mechanism by which mean flow stabilizes van-der-Waals-driven rupture is presented, thereby generalizing prior

work (Bielarz and Kalliadasis, 2003). The results of the present work are also useful in examining shear effects in practical applications of bounded two-layer flows like lithographic printing. High shear rates in lithographic printing might lead one to initially think that shear may significantly alter the rupture process. However, our research suggests that emulsification mechanisms in the lithographic printing process could be understood without incorporating shear. On the other hand, our simulations using parameter values typical of nanofluidic/microfluidic devices indicate that shear could be relevant in these systems.

CHAPTER 3

Thin film models of liquid displacement on chemically patterned surfaces for lithographic printing processes

We examine in this work a model problem relevant to the liquid displacement that occurs in lithographic printing processes. The model problem consists of two stratified thin liquid films confined between parallel plates, one of which is chemically heterogeneous. The films are assumed to be thin enough so that intermolecular forces are important and the lubrication approximation can be invoked. Both linear stability analysis and nonlinear simulations are applied to a partial differential equation governing the behavior of the liquid-liquid interface. The results provide physical insights into and numerical estimates of the smallest and largest feature sizes that can be printed, as well as the minimum spacing between feature sizes that can be tolerated. The results also provide insight into experimental observations on a closely related process, wire-wound rod coating on chemically patterned surfaces. The work presented here has important implications for the production of electronic devices and displays by lithographic printing, as well as for other processes that rely on coating and printing on chemically patterned surfaces.

3.1 Introduction

Thin-liquid-film behavior on chemically patterned surfaces is important for a number of emerging applications such as manufacturing of printed electronics (Noh et al.,

2007; Wang et al., 2004), operation of microfluidic devices (Squires and Quake, 2005), and ordered growth of nanotubes and nanowires (Xiong et al., 2006; Ko et al., 2004; Arase and Nakagawa, 2009). When a thin liquid film ($<\sim$ 100 nm) dewets on a solid surface, intermolecular forces (e.g., van der Waals and polar forces) play a central role in driving the resulting flow. If the solid surface is chemically patterned, gradients in wettability serve as an additional driving force for flow (Lenz and Kumar, 2007a; Kargupta et al., 2000; Kargupta and Sharma, 2002b,c, 2003; Thiele et al., 2003; Brusch et al., 2002; Kao et al., 2006). This additional feature leads to more complex stability behavior and dynamics, and makes the study of thin liquid films on chemically patterned surfaces a particularly rich topic.

Traditional printing methods offer great promise for fabrication of electronic devices and displays on flexible substrates. An especially promising route for the mass production of such devices is the lithographic printing process (Leyland et al., 2002; Hay et al., 2005; Southee et al., 2007; Ramsey et al., 2007; Hay et al., 2007), which is based on dewetting of thin liquid films on chemically patterned surfaces. As illustrated in Figure 3.1, conventional lithographic printing relies on the displacement of a thin barrier film of an aqueous solution on a printing plate cylinder by an oil-based ink film. The aqueous solution is applied by a 'dampening' system and the ink is applied by a 'form roll' connected to a series of cylindrical rollers. The printing plate surface is chemically patterned with 'image' and 'non-image' areas such that the ink film wets the image areas and is repelled from the non-image areas. As a result of this difference in wettability, the ink displaces the aqueous solution on the image areas (forming an emulsion) but not on the non-image areas, leaving the printing plate with ink only on the image areas (MacPhee, 1998). The inked cylinder is then contacted with a 'blanket' cylinder and the image is transferred to a substrate.

Because of the importance of wettability and wettability gradients in lithographic printing, it is natural to construct models of this process that are based on the theory of thin liquid films. The first effort in this direction was that of Lenz and Kumar (2007a), who assumed that the ink and water (i.e., aqueous solution) films on the printing plate are squeezed down to thicknesses on the order of 100 nm (from thicknesses $\sim$ 1-2 μm (MacPhee, 1998)) in the region where the form roll contacts the aqueous-solution-covered printing plate. At these thicknesses, van der Waals forces are assumed to become active and drive liquid displacement. Because the film thicknesses are much smaller than the roll radii, Lenz and Kumar idealized the liquid displacement process as a stratified two-layer thin-film flow near a chemically patterned surface, where the upper layer represents ink and the lower layer water

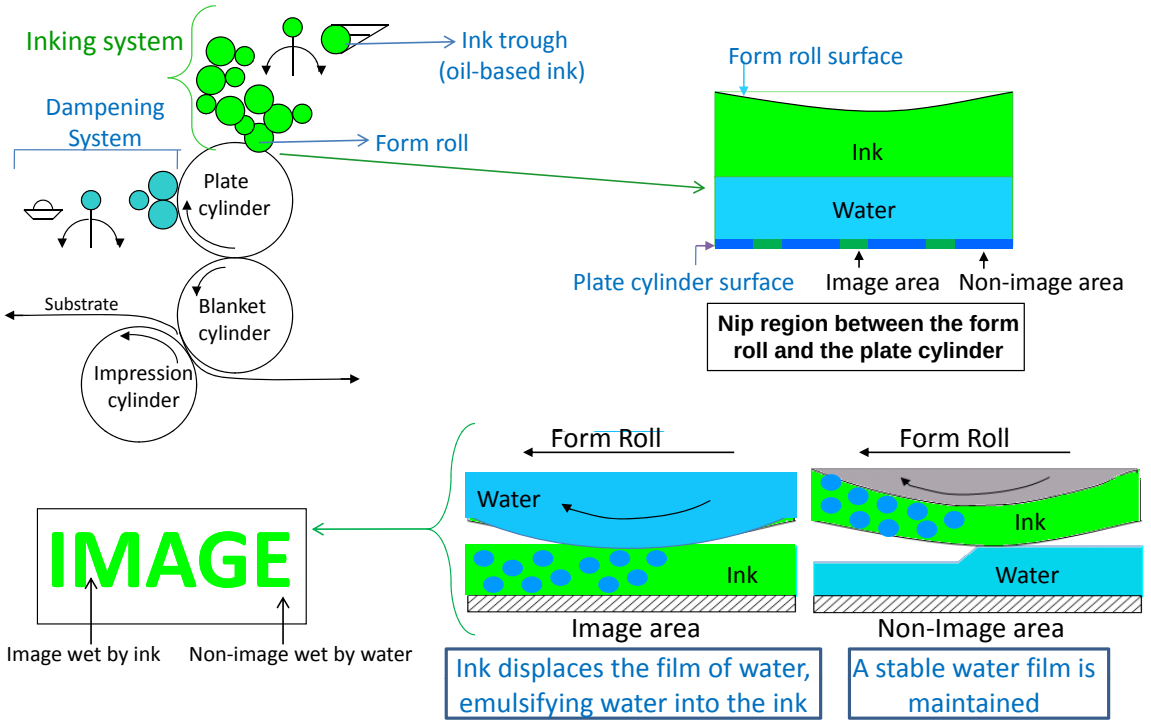

Figure 3.1: The lithographic printing process

(Figure 3.2).

Using principles of lubrication theory Lenz and Kumar (2007a), derived a nonlinear evolution equation for the liquid-liquid interface that accounted for intermolecular forces only through an attractive van der Waals component. The equation was solved numerically on a periodic domain for different image sizes, with the sum of the image and non-image sizes (i.e., period length) held constant. The authors found that if the image size is sufficiently small, the water film will rupture in only one place in the image areas, whereas if it is sufficiently large, it will rupture in two places (near

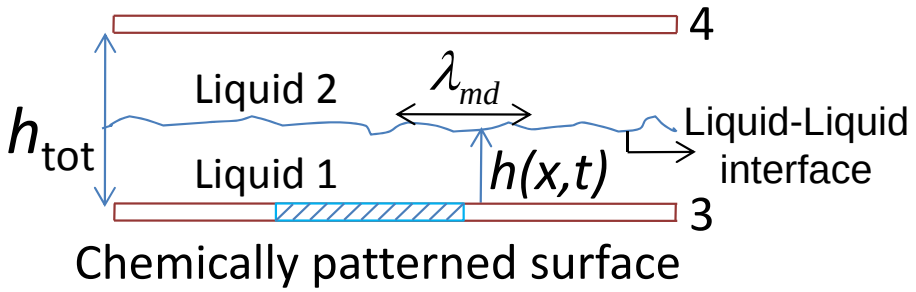

Figure 3.2: Model geometry used to study liquid displacement. Liquid 1 represents water and Liquid 2 represents ink.

the edges) due to flows driven by wettability gradients. Although the simulations could not be continued beyond the point of rupture, the authors hypothesized that once rupture occurred, the ink would spread on the image area and trap a water droplet. Their results thus suggest a mechanism by which aqueous solution becomes emulsified in ink, a key feature of the lithographic printing process that had not been explained prior to their work. An extension of the model that accounts for shear flow predicts that the shear rates present in lithographic printing are not large enough to significantly modify rupture behavior (Kalpathy et al., 2010).

Although the work of Lenz and Kumar (2007a) provides some initial insight into the mechanics of liquid displacement that occur during lithographic printing, it has two important shortcomings. First, it does not include a repulsive component of the intermolecular force, which prevents the simulations from proceeding beyond the point of rupture. Second, both image and non-image sizes are varied simultaneously, making it difficult to determine the distinct role of each length scale. Addressing the first issue would provide further insight into the mechanics of emulsification, including the spreading of ink on the image areas hypothesized by Lenz and Kumar (2007a). Addressing the second issue would allow one to obtain estimates of the smallest image and non-image sizes one can use in lithographic printing. The smallest image size provides a measure of the resolution of the process and the smallest non-image size determines how densely features can be printed, both of which are important considerations in applying lithographic printing to fabricate electronic devices. The purpose of the present work is to address the above two issues.

Before proceeding, we point out that there has been a considerable amount of prior work on the modeling of thin liquid film behavior on chemically patterned surfaces (Kargupta et al., 2000; Kargupta and Sharma, 2003; Konnur et al., 2000; Zope et al., 2001; Kargupta and Sharma, 2002c,b; Sharma et al., 2003; Kargupta et al., 2001). However, in these studies, the liquid film is bounded from above by a passive gas, making it different from the confined liquid-liquid system examined here. Indeed, it is not apparent how quantitative estimates relevant to lithographic printing can be extracted from this prior work unless one accounts for the presence of the second liquid phase and a bounding solid surface. Liquid film bilayers on chemically patterned substrates have also been studied (Bandyopadhyay and Sharma, 2010), but there a passive gas bounds the top layer resulting in a problem with two free interfaces rather than a single one in the configuration examined here. In addition, liquid film trilayers between solid surfaces have been examined to understand the role of residual ink on the image areas of the printing plate in lithographic printing (Lenz and Kumar,

2007b).

The rest of the paper is organized as follows. In section 3.2, we discuss our interfacial evolution equation, its linear stability, and the numerical methods used. Results from an extensive numerical study are presented in section 3.3. In section 3.4, we discuss the application of our results to lithographic printing and the closely related process of wire-wound rod coating on chemically patterned substrates. Conclusions are given in section 3.5.

3.2 Model

3.2.1 *Evolution equation*

Figure 3.2 depicts the model geometry. Two Newtonian liquids (1 and 2) are confined between flat parallel plates. The bottom plate (3) may be either chemically homogeneous or chemically patterned in such a way that liquid 2 preferentially wets the hatched area on the bottom plate (termed 'image area' hereafter). The unhatched areas (termed 'non-image areas' hereafter) are neutral to both liquids. We assume that the gap between the two plates, h_{tot}, is much smaller than the characteristic horizontal length scale λ_{md}, which is the wavelength of a typical perturbation of the interface that grows the fastest on a chemically homogeneous surface (see section 3.2.2). Since $\epsilon = \frac{h_{tot}}{\lambda_{md}} \ll 1$, we can apply the lubrication approximation to develop an evolution equation for the interface.

For convenience, we non-dimensionalize the problem in the same way as Lenz and Kumar (2007a):

$$x = \frac{\epsilon\tilde{x}}{h_{tot}}, \qquad z = \frac{\tilde{z}}{h_{tot}}, \qquad u_i = \frac{\tilde{u_i}\rho_1 h_{tot}}{\mu_1}, \qquad w_i = \frac{\tilde{w_i}\rho_1 h_{tot}}{\epsilon\mu_1}. \tag{3.1}$$

Here x and z are position variables in the horizontal and the vertical directions, respectively, and u and w are the corresponding velocity components. Variables with a tilde are dimensional and the subscript i denotes that the variable belongs to liquid i. The density is denoted by ρ and the viscosity by μ. Time and pressure are non-dimensionalized as follows:

$$t = \frac{\epsilon\tilde{t}\mu_1}{h_{tot}^2\rho_1}, \qquad (p_i, \phi_i) = (\tilde{p_i}, \tilde{\phi_i})\frac{\epsilon h_{tot}^2\rho_1}{\mu_1^2}. \tag{3.2}$$

Here, t denotes time, p denotes the dynamic pressure, and ϕ is the dimensionless

potential for the disjoining pressure for each liquid.

The non-dimensional equation governing the evolution of the liquid-liquid interface is obtained by substituting the above scalings in to the governing equations (mass and momentum conservation) and boundary conditions (no-slip and no-penetration on the solid walls, stress balance and kinematic condition on the interface). After rescaling the interfacial tension (assumed constant), only the leading order terms are retained. Since the details of the derivation have been presented in previous work (Joo and Hsieh, 2000; Lenz and Kumar, 2007a; Kalpathy et al., 2010), we choose to simply present the final result:

$$0 = \partial_t h + \partial_x \left\{ \frac{[1 + (\mu_r - 1)h](1-h)^3 h^3}{3f(h, \mu_r)} [\partial_x (\phi_2\big|_{z=h} - \phi_1\big|_{z=h}) + 3\gamma_{12}\partial_x^3 h] \right\}, \tag{3.3}$$

with $f(h, \mu_r)$ given by:

$$f(h, \mu_r) = h^4\mu_r^2 - (2h^4 - 4h^3 + 6h^2 - 4h)\mu_r + (h-1)^4. \tag{3.4}$$

Here $h(x,t)$ is the dimensionless height of the liquid-liquid interface, μ_r is the ratio of the viscosity of liquid 2 to that of liquid 1, and γ_{12} is the dimensionless interfacial tension between liquids 1 and 2, which has been scaled as follows:

$$\gamma_{12} = \frac{\epsilon^3 \tilde{\gamma_{12}} \rho_1 h_{tot}}{3\mu_1^2}. \tag{3.5}$$

Motivated by prior work (Oron and Bankoff, 1999a) which models the evolution of thin liquid films under the action of attractive and repulsive intermolecular forces, we use the following power-law form to describe ϕ_i:

$$\phi_1 = \frac{A_1}{h^3} - \frac{B_1}{h^4}, \qquad \phi_2 = \frac{A_2}{(1-h)^3} - \frac{B_2}{(1-h)^4}. \tag{3.6}$$

Here A_i and B_i are dimensionless parameters (commonly referred to as Hamaker constants), and they can assume either positive or negative values. The term A_1/h^3 represents van der Waals interactions and it is derived from the specific form of London intermolecular interactions, $u \sim 1/r^6$, where u is the potential energy of interaction between two molecules and r is the distance separating two molecules (Hamaker, 1937). The term B_1/h^4 represents a short-range force arising from polar forces which are based on Lewis acid-base interactions in polar species (van Oss et al., 1987). Different mathematical representations have been used by previous authors

(Teletzke et al., 1987; Khanna et al., 1996; Schwartz and Eley, 1998; Sharma and Khanna, 1998; Kargupta and Sharma, 2002b) to incorporate such short-range forces and the exact expression would depend on material properties such as wettability and microscopic surface roughness. The form B_1/h^4 is chosen here for computational convenience. As in Lenz and Kumar (2007a), the results discussed in this paper are all for the case $\phi_2 = 0$, for which (3.3) will reduce to

$$0 = \partial_t h + \partial_x \left\{ \frac{[1 + (\mu_r - 1)h](1-h)^3 h^3}{3f(h, \mu_r)} [\partial_x \Big(\frac{B_1}{h^4} - \frac{A_1}{h^3} \Big) + 3\gamma_{12} \partial_x^3 h] \right\}. \tag{3.7}$$

Note that for chemically homogeneous surfaces, A_1 and B_1 are constants, whereas for chemically heterogeneous surfaces A_1 and B_1 are functions of x. Because the viscosity ratio enters (7) in a highly nonlinear way, it is not obvious how the presence of the upper fluid layer and solid surface will influence system stability and dynamics.

Depending on the signs of A_1 and B_1, the choice of potential for ϕ_1 in (4.3) could give rise to four distinct system types (Sharma, 1993). The combination $A_1 > 0, B_1 < 0$ corresponds to systems of Type 1 in which both the short-range and the long-range terms of the potential are attractive. These systems will rupture completely when subject to small-amplitude initial disturbances. Type 2 systems correspond to $A_1, B_1 > 0$, where a long-range attraction combines with a shorter range repulsion. Such systems also tend to be unstable to small-amplitude disturbances, but instead of rupturing completely they approach an equilibrium film thickness due to the effect of short-range repulsive forces. Type 3 systems ($A_1 < 0, B_1 > 0$) are always stable as both the long- and short-range interactions are repulsive. As opposed to systems of Type 2, the combination $A_1, B_1 < 0$ is classified as Type 4 where a long-range repulsion combines with a short-range attraction. With initially small-amplitude perturbations, the long-range repulsive forces would dominate and such systems would tend to remain stable, but would thin down to an equilibrium film thickness with larger amplitude perturbations. In the present work, we consider systems of Type 2, so that A_1 describes long-range attraction and B_1 describes short-range repulsion. In the limit $B_1 = 0$, (4.13) reduces to the evolution equation considered by Lenz and Kumar (2007a) where only the long-range attraction is present.

3.2.2 *Linear stability analysis*

Application of standard linear stability analysis to the nonlinear evolution equation (4.13) gives the dimensionless growth rate s of interfacial perturbations in terms of the

initial interface height h_0, μ_r, γ_{12}, and the disjoining pressure potential parameters A_1 and B_1:

$$s = \frac{k^2(h_0(\mu_r - 1) + 1)}{f(h_0, \mu_r)}\Big(\frac{A_1(1-h_0)^3}{h_0} - \frac{4B_1(1-h_0)^3}{3h_0^2} - k^2\gamma_{12}h_0^3(1-h_0)^3\Big), \quad (3.8)$$

where $f(h, \mu_r)$ corresponds to the function in (3.4), and k is the wavenumber of the interfacial perturbation. The most dangerous wavelength λ_{md} is obtained by maximizing the growth rate s with respect to the wavenumber k:

$$\lambda_{md} = \frac{2\pi}{\sqrt{\frac{1}{2\gamma_{12}}\Big(\frac{A_1}{h_0^4} - \frac{4B_1}{3h_0^5}\Big)}}. \quad (3.9)$$

In dimensional terms, this expression is:

$$\tilde{\lambda}_{md} = \frac{2\pi\tilde{h}_0^2}{\sqrt{\frac{3\tilde{A}_1}{2\tilde{\gamma}_{12}} - \frac{2\tilde{B}_1}{\tilde{h}_0\tilde{\gamma}_{12}}}} \quad (3.10)$$

where $\tilde{\lambda}_{md}$ denotes the dimensional most dangerous wavelength, $\tilde{h}_0$ is the initial dimensional height of the interface, and $\tilde{A}_1$ and $\tilde{B}_1$ are the power-law constants in the dimensional expression for $\tilde{\phi}$, given by (3.11):

$$\tilde{\phi} = \frac{\tilde{A}_1}{\tilde{h}_0^3} - \frac{\tilde{B}_1}{\tilde{h}_0^4}. \quad (3.11)$$

In order for instability of the liquid-liquid interface to occur, the most dangerous wavelength described by (4.16) needs to be real, which yields the criterion

$$\frac{B_1}{A_1} < \frac{3h_0}{4}. \quad (3.12)$$

The ratio B_1/A_1 represents the minimum height of the interface at equilibrium.

An estimate of the time T_e that is required for the interface to thin down to the equilibrium film thickness may be obtained as: (Williams and Davis, 1982)

$$T_e = \frac{1}{s}\ln\Big(\frac{h_0}{\epsilon}\Big), \quad (3.13)$$

where s is the growth rate defined by (4.14), and ϵ is the amplitude of the interfacial perturbation. Accordingly, we expect T_e, to increase monotonically with an increase

in the viscosity ratio μ_r as well as the height ratio h_0. Interfacial perturbations would grow more slowly owing to viscous dissipation when μ_r is higher, causing T_e to increase. As the van der Waals forces between the liquids and the bottom surface decrease as h^{-3}, they are more effective when h_0 is smaller, which would again result in an increase in T_e with increasing h_0 (Note that we neglect any attraction or repulsion from the top surface 3 (see Figure 3.2)).

3.2.3 *Numerical methods*

Nonlinear simulations were performed with (4.13) to obtain interface height profiles $h(x,t)$. A centered finite-difference scheme was used to discretize the evolution equation in space, and time integration was done using DASSL (Differential Algebraic System Solver) to adequately address the numerical stiffness of the problem. The simulations described in sections 3.3.1 and 3.3.2, required ∼400 and ∼600 nodes respectively per most dangerous wavelength λ_{md} to ensure mass conservation. A domain length as wide as $3\lambda_{md}$ was deemed sufficient in these calculations to ensure results independent of node spacing. Periodic boundary conditions were used in all cases. Mass conservation was addressed using the criterion that the mean interface height was always within 0.02% of the initial interface height during the course of the simulations. With an initially flat interface, a random perturbation of small amplitude (~ 0.1) consisting of different wavelengths ranging from $3\lambda_{md}$ to $\lambda_{md}/100$ was used as the initial condition.

To describe the spatial variation of A_1 and B_1 that is necessary in order to model chemically patterned surfaces, we use an arctangent function (Stillwagon and Larson, 1988; Lenz and Kumar, 2007a). For surfaces consisting of a single image area in the center bordered by non-image areas on its sides (section 3.3.2), as in figure 3.2, we used the following dimensionless expressions:

$$A_1(x) = \frac{A_1^{Im}}{\pi}\left[\tan^{-1}(\frac{x+I/2}{\delta}) - \tan^{-1}(\frac{x-I/2}{\delta})\right], \tag{3.14a}$$

$$B_1(x) = \frac{B_1^{Im}}{\pi}\left[\tan^{-1}(\frac{x+I/2}{\delta}) - \tan^{-1}(\frac{x-I/2}{\delta})\right], \tag{3.14b}$$

where A_1^{Im} and B_1^{Im} are constants, I is the size of the image area in the center, and δ is the dimensionless transition width between an image and a non-image area, which was chosen to be 0.01 (as in Lenz and Kumar (2007a)). The functions on the right-

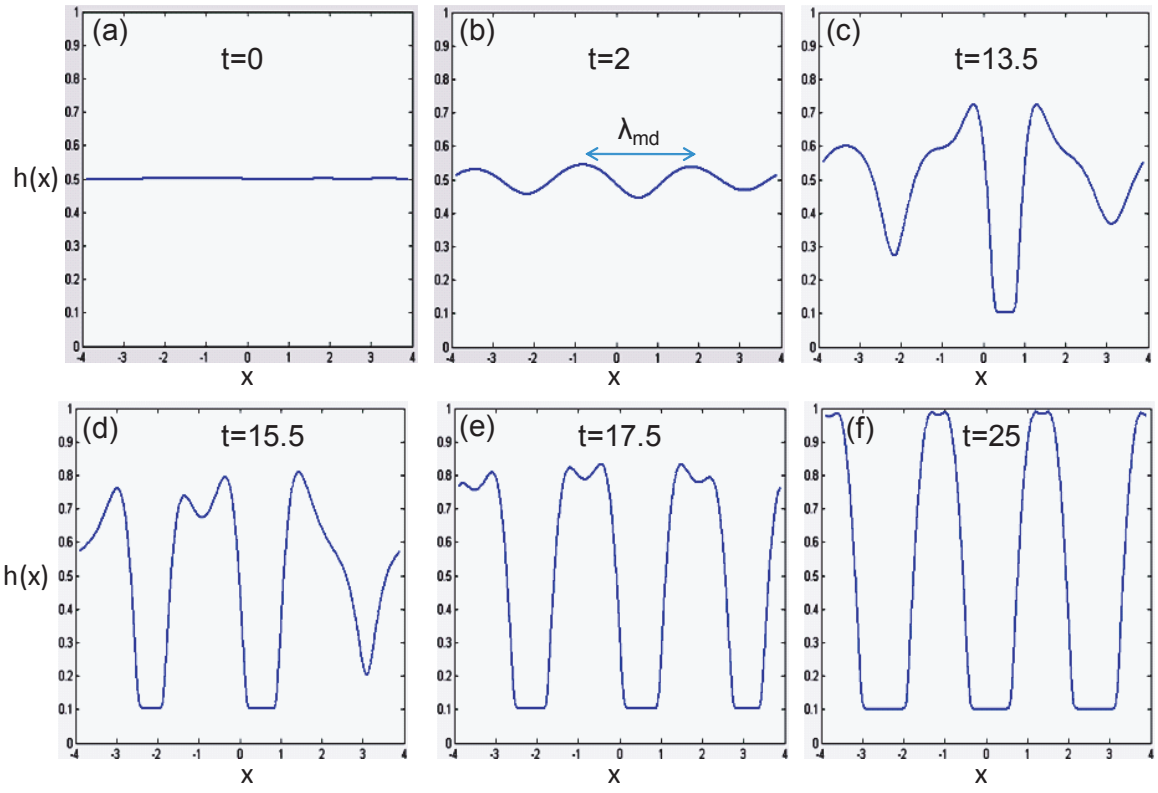

Figure 3.3: Time evolution of the interface on chemically homogeneous surfaces.

hand sides in (3.14) approach 0 on the non-image areas, and the values represented by the constants A_1^{Im} and B_1^{Im} on the image areas. A modified form of these functions (see Appendix 1) was used to study cases where a single domain can accommodate multiple image and non-image areas (section 3.3.3). Such arrangements were probed to study how densely features can be printed. These functions were mathematically more complex and hence required ∼1000 spatial nodes per most dangerous wavelength in order to ensure mass conservation.

3.3 Results and Discussion

3.3.1 *Chemically homogeneous surfaces*

To fully appreciate the results involving chemically heterogeneous surfaces that will be discussed later, we first briefly consider the case of chemically homogeneous surfaces. Lenz and Kumar (2007a) considered the case where $B_1 = 0$, which leads to interfacial rupture, i.e., the interface height approaches zero at some point in the domain due to long-range van der Waals attraction. Here, we set $B_1 = 0.1$ and take the other

parameters to be $\mu_r = 1$, $\gamma = 1$, $h_0 = 0.5$, and $A_1 = 1$. These parameters are a representative set; runs with different sets show qualitatively similar behavior.

Figure 3.3 shows a typical time evolution of the interface, obtained by solving (4.13). Initially, small-amplitude fluctuations imparted to the interface begin to grow with the waves exhibiting a wavelength on the order of λ_{md} (from linear stability analysis, see section 3.2.2). The presence of the short-range repulsion prevents a complete rupture, and instead the depressions begin to grow until the minimum equilibrium film thickness B_1/A_1 is reached ($t = 13.5$). We will use the term 'rupture-like event' throughout this paper to describe this step. After the first rupture-like event, the liquid in the top layer displaces some of the liquid in the bottom layer toward the sides ($t = 15.5$, $t = 17.5$) at the point where the equilibrium film thickness was first reached. As a result, liquid 1 forms two droplets in the center of the domain in equilibrium with a very thin film and two near-ruptures continue to grow. After three rupture-like events have occurred ($t = 17.5$), the three corresponding thin films of thickness B_1/A_1 continue to grow until an effective steady-state is reached ($t = 25$).

The time required for the first rupture-like event, T_e, is found to increase monotonically with an increase in both μ_r and h_0. This is consistent with the predictions from linear stability analysis (see section 3.2.2) as well as the qualitative behavior noted by Lenz and Kumar (2007a) when the short-range repulsion term is absent ($B_1 = 0$).

3.3.2 *Chemically patterned surfaces: Effect of image size*

We now turn to the case of chemically heterogeneous surfaces. In particular, we consider the case where the bottom surface is chemically patterned (i.e., A_1 and B_1 vary with x), and systematically vary the size of the image area with the total domain length fixed at $3\lambda_{md}$. This extends the work of Lenz and Kumar (2007a) to the case where short-range repulsion is present. Equation (4.13) is solved with $h_0 = 0.5$, $\gamma = 1$, and $\mu_r = 1$. The variation of A_1 and B_1 is described by (3.14), with $A_1^{Im} = 1$ and $B_1^{Im} = 0.1$.

Figure 3.4 shows the time required for the first rupture-like event as a function of image size I. The shape of this curve is similar to that obtained by Lenz and Kumar (2007a) in the absence of the short-range repulsion. Four important limits of T_e occur at $I_a = 0.3\lambda_{md}$, $I_b = 0.8\lambda_{md}$, $I_c = 1.15\lambda_{md}$, and $I_d = 2.5\lambda_{md}$, where the curve goes through either a maximum or a minimum; the corresponding steady-state interface profiles are depicted in Figure 3.5. Note that when $I = 0$, T_e becomes infinite because

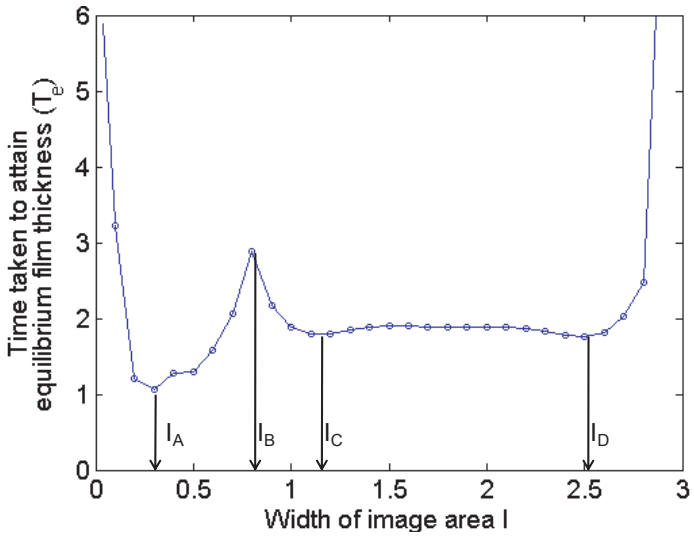

Figure 3.4: Time taken to reach the equilibrium film thickness as a function of image size (in units of λ_{md}).

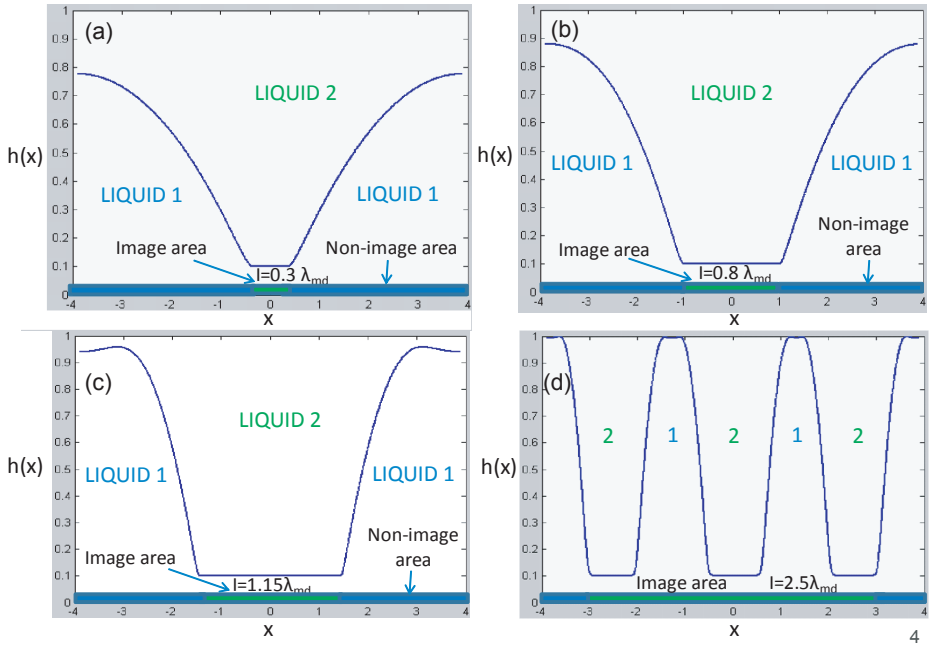

Figure 3.5: Steady-state interface profiles on chemically patterned surfaces for (a) $I_a = 0.3\lambda_{md}$, (b) $I_b = 0.8\lambda_{md}$, (c) $I_c = 1.15\lambda_{md}$, and (d) $I_d = 2.5\lambda_{md}$.

there is no driving force for dewetting. When $I = 3\lambda_{md}$, T_e takes the value it would have on a chemically homogeneous surface.

As with chemically homogeneous surfaces, small-amplitude fluctuations imparted to the interface begin to grow and thin the interface until the interface reaches an equilibrium film thickness, B_1/A_1. Thereafter, wettability gradients become active, causing the liquid layers to spread away from the image area, and consequently the width of equilibrium film increases. This would correspond to the spreading of the ink film on the image areas hypothesized by Lenz and Kumar (2007a), although here the ink is separated from the image area by a thin water film. For image sizes I_a, I_b, and I_c, this process continues until the thin equilibrium film of liquid 1 covers the entire image area, as seen in Figure 3.5(a)-(c). However, for image size $I_d = 2.5\lambda_{md}$, the liquid in the lower layer beads up to form two large droplets within the image area (Figure 3.5(d)). (Steady-state profiles for image sizes $I > 2.5\lambda_{md}$ are similar to that seen in Figure 3.5(d).)

From the perspective of lithographic printing, where intentional rupture is desired, the interface profiles corresponding to I_a, I_b, and I_c in Figure 3.5 would correspond to the formation of a thin water layer on the image area. If a dust particle or some other artifact is present, the water film may rupture due to a heterogeneous nucleation mechanism not described by our model. This rupture event would cause trapping of small droplets of the aqueous layer within the film of ink, whose size would be on the order of the equilibrium film thickness or smaller. In contrast, a similar rupture event on larger image area (e.g., $I = 2.5\lambda_{md}$) would lead to larger globules of water trapped within the image area. This may diminish the quality of the final image if the amount of trapped water is large enough to produce a faded image. Steady-state interface profiles resembling Figure 3.5(d) have been seen in our simulations using dimensional parameter values relevant to lithographic printing applications; these results are discussed in section 3.4.

We now discuss the dynamics of the dewetting process described above. For $I = 0.3\lambda_{md}$, the rupture-like event occurs at the image center (results not shown). As in the case where short-range repulsion is absent (Lenz and Kumar, 2007a), it is driven by wettability gradients that drive the lower liquid off the less wettable image area onto the more wettable non-image area. A minimum in T_e is observed (Figure 3.4) because the wettability gradients are cooperating to displace the lower liquid.

As the image size is increased, the first rupture-like event occurs near an edge of the image area. A typical example is shown in the time sequence plot in Figure 3.6

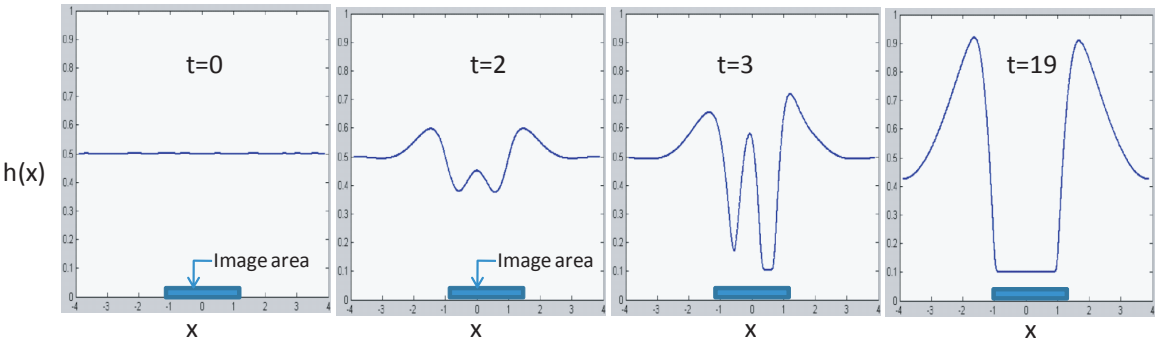

Figure 3.6: Time evolution of the interface on a chemically patterned surfaces with a single image area of size $I = 0.8\lambda_{md}$.

Table 3.1: Comparison between the time it takes for the interface to first reach the equilibrium film thickness with the time it takes to reach the equilibrium film thickness at the center of the image area.

Image size	Time of initial rupture-like event	Time of rupture-like event at the image center
$0.3\lambda_{md}$	1.062	1.062
$0.8\lambda_{md}$	2.881	16.876
$1.15\lambda_{md}$	1.790	76.378
$2.5\lambda_{md}$	1.761	4.784

for $I = 0.8\lambda_{md}$. Here, the wettability gradients drive the liquid off the image area, but this is resisted by the flow generated by the high-curvature regions of the interface. As a consequence, a local maximum in T_e is observed (Figure 3.4). The off-center rupture-like events cause liquid 1 to be trapped at the center of the image area for some time until the entire liquid is driven out toward the non-image areas. This results in a situation where the dynamics of the interface at the center of the image are much slower than the dynamics at the image edges for certain image sizes. Table 1 compares the times for the initial rupture-like event and that at the image center. A significant difference of about two orders of magnitude is found for the intermediate image sizes $I = 0.8\lambda_{md}$ and $I = 1.15\lambda_{md}$. Such a difference may prove significant for lithographic printing if the entrapped water at the image center remains on the image area for a longer period than the ink residence times within the printing nip (see section 3.4).

The system has a natural length scale characterized by the most dangerous wavelength for a homogeneous surface, λ_{md}. As the image size approaches this value from below, the system becomes less constrained and T_e decreases (Figure 3.4). For large enough image size (e.g., $I = 2.5\lambda_{md}$), the system is nearly chemically homogeneous and multiple, large water droplets form on the image area (Figure 3.5(d)). Eventually, wettability gradients become less important and T_e begins to increase as I increases (Figure 3.4).

3.3.3 *Chemically patterned surfaces: Effect of non-image size*

In the previous section, we varied the image and non-image sizes simultaneously on a domain of fixed length as was done by Lenz and Kumar (2007a). In this section, we address the issue of how closely image areas can be placed to each other by varying the non-image size for a fixed image size.

To do this, we performed a series of simulations where a single domain accommodates multiple image and non-image areas packed in an alternating manner. The image and the non-image areas are small enough so that the total length of one image area and two bordering non-image areas is less than $3\lambda_{md}$. We used periodic boundary conditions similar to those in sections 3.3.1 and 3.3.2, and the results were verified to be independent of the total domain length, which was at least 4 times the sum of the image size and the non-image size for the results shown in this section. For these simulations, we set $h_0 = 0.5$, $\mu_r = 1$, and $\gamma = 1$. The variation of A_1 and B_1 is described by the expressions in Appendix 1, with $A_1^{Im} = 1$, $B_1^{Im} = 0.1$, I and N being varied in the range $0.1\lambda_{md} - 3\lambda_{md}$.

Figure 3.7 shows time-evolution of the interface for an image size $I = 0.5\lambda_{md}$ and non-image size $N = 0.1\lambda_{md}$. The initial rupture-like event and consequent film spreading for this case ($t = 2.1$) has occurred on an image area as expected. However, the size of the non-image area between adjacent image areas is too small such that the subsequent thinning of the interface is frustrated. Such structures have been observed by Kargupta (Kargupta and Sharma, 2002c) in their study on the effects of substrate periodicity in single-layer flows. However, these are quasi-stable structures which evolve further in time. At $t = 3.6$, a second rupture-like event has occurred and the interface has spread over a non-image area forming a thin film of equilibrium thickness $B_1^{Im}/A_1^{Im} = 0.1$. At steady state ($t = 6.2$), a third rupture-like event has occurred and a film has spread partly over an adjacent non-image area. If a rupture

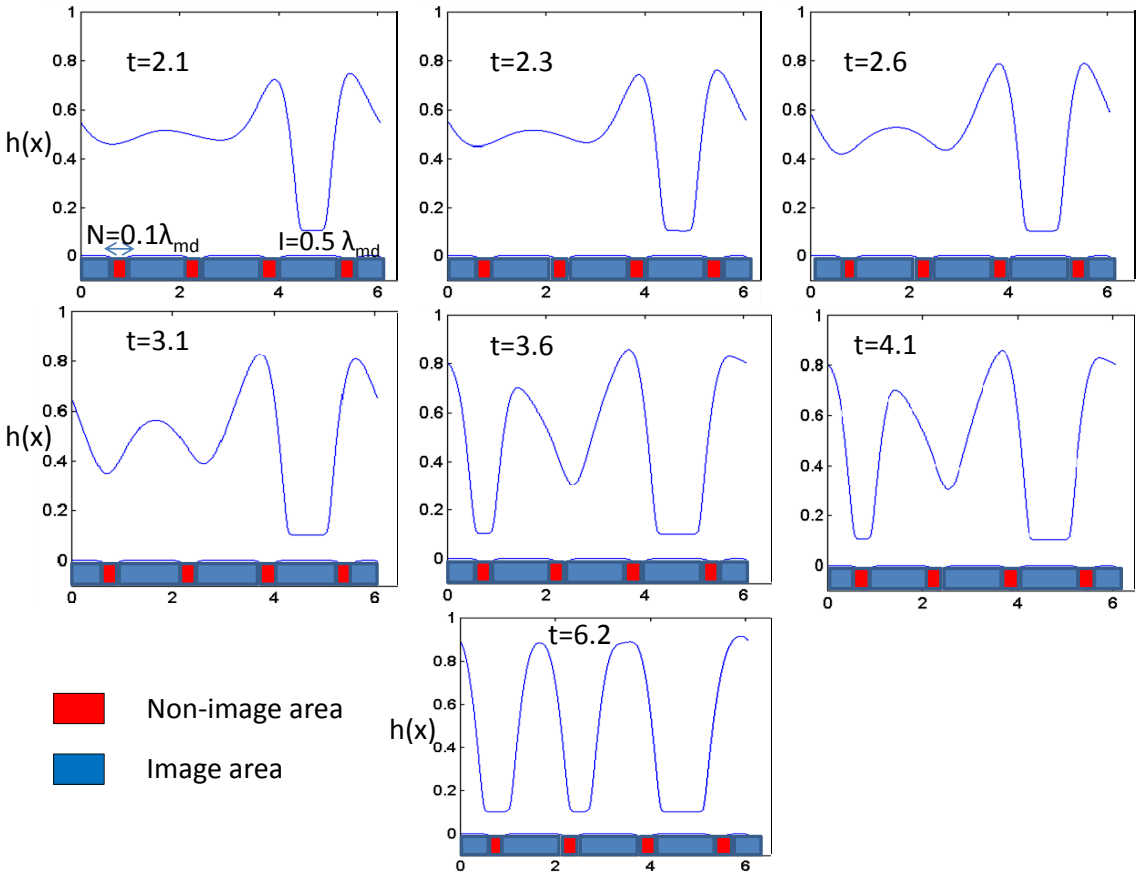

Figure 3.7: Time evolution of the interface on a domain with alternating image and non-image areas with image size $I = 0.5\lambda_{md}$ and non-image size $N = 0.1\lambda_{md}$.

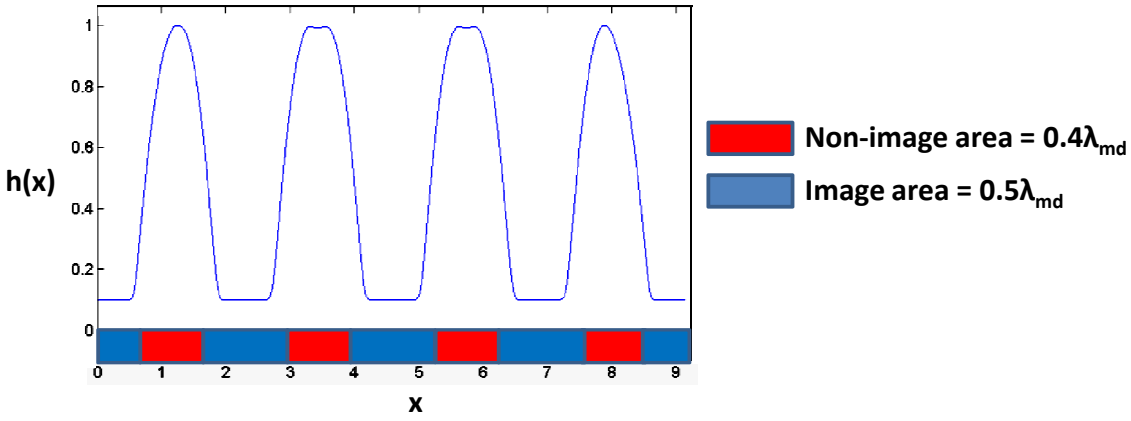

Figure 3.8: Steady-state interface profile for a domain with alternating image and non-image areas with image size $I = 0.5\lambda_{md}$ and non-image size $N = 0.4\lambda_{md}$.

were to occur at either of these locations by a heterogeneous nucleation mechanism similar to that discussed in section 3.3.2, the top layer would wet the non-image areas.

In contrast, Figure 3.8 shows the interface profile for image size $I = 0.5\lambda_{md}$ and nonimage size $N = 0.4\lambda_{md}$, where the equilibrium film has formed only on the image areas at steady state. From the viewpoint of lithographic printing, a structure such as that shown in Figure 3.8 would lead to near-perfect templating, whereas that in Figure 3.7 ($t = 6.2$) would cause the ink to spill over onto the non-image areas and thus undermine print quality. These results suggest that there exists a limitation on the smallest non-image size or the closest packing that can be achieved while printing images on a chemically patterned surface.

In order to probe how the film spreading onto non-image areas mentioned above is influenced by the actual sizes of the image and non-image areas used, we constructed the map in Figure 3.9, which demarcates regions where the possible 'spill-over' event occurs on the non-image areas, as a function of the image and non-image sizes. The figure shows two boundaries which are critical non-image sizes for a given image size. The bottom boundary lies between $N \sim 0.3\lambda_{md} - 0.6\lambda_{md}$; below this boundary, film spreading onto non-image areas is always seen. The shape of this boundary resembles Figure 3.4, indicating that the underlying mechanisms are similar to those discussed in section 3.3.2 (see also Lenz and Kumar (2007a)). For certain image sizes it was observed that even as the non-image size is increased above the value represented by the bottom boundary, film spreading onto non-image areas occurs at repeated intervals of non-image size ranges (see below for further discussion). This re-entrant behavior is terminated by a top boundary ($N \sim 2\lambda_{md} - 3\lambda_{md}$), so that this phenomenon is completely eliminated for non-image sizes larger than the values represented by this boundary.

The exact location of these boundaries in units of λ_{md} was determined to be sensitive to the viscosity ratio μ_r and the initial interface height h_0. For instance, a reduction in viscosity ratio by a factor of 1000 increases the minimum non-image size suggested by the bottom boundary by ∼60%. Similarly, an increase in the initial height by a factor of 2 increases the minimum non-image size suggested by the bottom boundary by ∼10%. However, a general heuristic that may be extracted from these calculations is that for liquid layers with comparable viscosities and thicknesses, spill-over events would occur for non-image sizes $N < B$, where $B \sim 0.3\lambda_{md} - 0.6\lambda_{md}$. Such events would not be observed for non-image sizes $N > T$, where $T \sim 2\lambda_{md} - 3\lambda_{md}$. The intermediate regime $B < N < T$ would correspond to non-image sizes where the re-entrant behavior discussed above is observed.

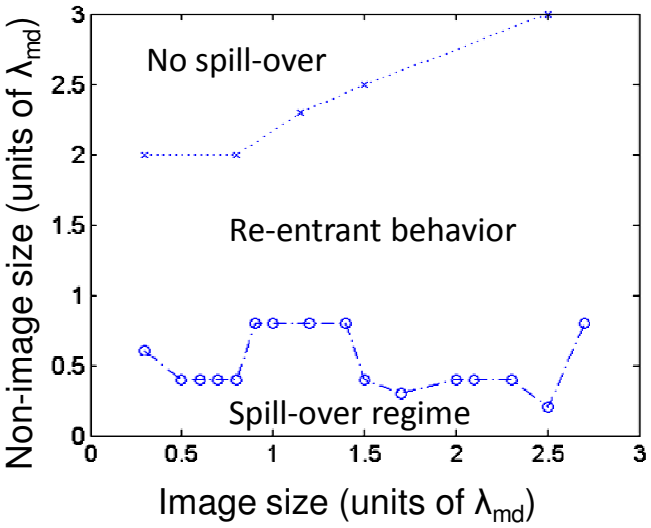

Figure 3.9: Map demarcating the regions where 'spill-over' events are observed.

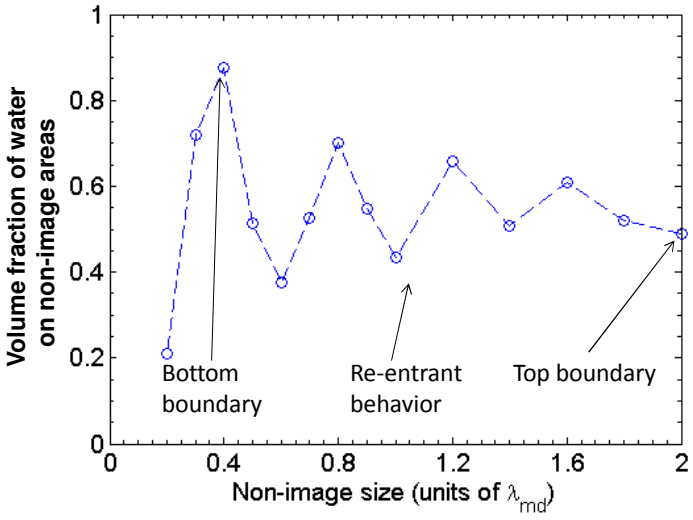

Figure 3.10: Volume fraction of the bottom liquid 1 present on the non-image areas for $I = 1.5\lambda_{md}$. The plotted data is at time $t = 17.1$ when steady state has been reached. The labels 'top boundary' and 'bottom boundary' correspond to the boundaries of Figure 3.9.

In order to understand better the mechanism behind the spill-over events, the volume fraction of the bottom liquid present on the non-image areas was calculated using the steady-state interface profiles. Figure 3.10 shows this quantity as a function of the non-image size for a fixed image size $I = 1.5\lambda_{md}$. The plot shows that the volume fraction of liquid varies in a zig-zag manner and finally plateaus when the non-image size reaches the value represented by the top boundary shown in Figure 3.9. The minima in the curve denote points where the re-entrant behavior of film spreading on non-image areas is seen, i.e., when the bottom liquid collects on the image areas. The occurrence of the spill-over events may be rationalized by considering free-energy minimization. Since the bottom liquid is on a chemically patterned surface, there are preferential locations where the liquid tends to dewet and other places where it tends to collect. At long times, the system will tend to evolve to a state of minimum free energy. However, a perfectly templated structure with very high interfacial curvatures may incur higher energy penalties as compared to a structure similar to that in Figure 3.7 ($t = 6.2$), where the film spreads onto the non-image areas for small non-image sizes.

3.4 *Application to lithographic printing and wire-wound rod coating*

3.4.1 Lithographic printing

To understand how the general results presented in the previous section can provide further insight into lithographic printing processes, we performed a set of simulations using parameters characteristic of these processes (MacPhee, 1998). Typically, the ink is much more viscous than the aqueous solution, so we have chosen the viscosity ratio μ_r to be 1000 and assumed that the viscosity of the lower layer is 0.001 Pa s. The interfacial tension $\tilde{\gamma}$ was set to a value of 30 mN/m. We set the ink thickness at 500 nm, and consider two different thicknesses for the aqueous layers, 20 nm and 100 nm. We note that there is a considerable amount of uncertainty about the thickness of the aqueous layer because these have not (to our knowledge) been directly measured. However, the thickness of the aqueous layer can be controlled in practice through adjustment of the dampening system, so we expect that our results will at least provide some qualitative guidance. The constants in the potential for the disjoining pressure are estimated to be $A_1 = 10^{-20}$ J, $B_1 = 5$ x 10^{-29} J m (see Appendix 2). With these values, we find that $\lambda_{md} = 7.5$ μm for a 20 nm aqueous layer, and

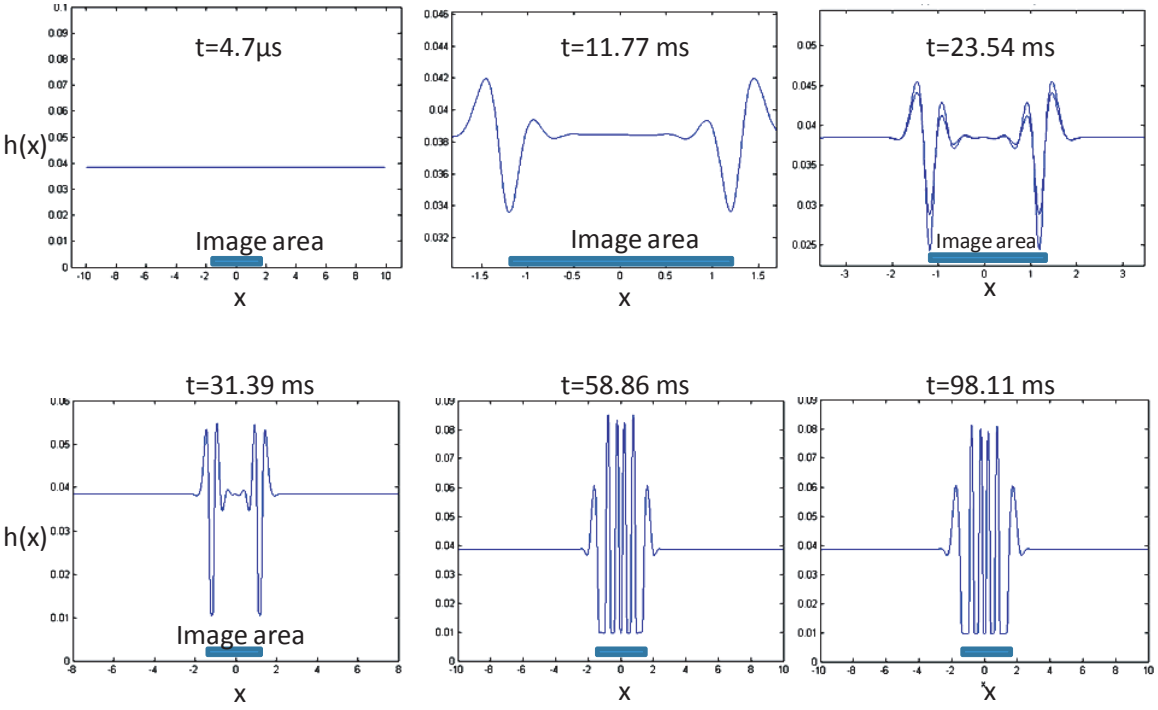

Figure 3.11: Time evolution of the interface using parameter values characteristic of lithographic printing. Note that the scale of the x-axis is changing in each plot.

$\lambda_{md} = 52.5$ μm for a 100 nm aqueous layer.

Figure 4.20 shows a time sequence of the interface evolution for an image size $I = 20$ μm and an aqueous layer thickness of 20 nm. It is seen that structures with multiple rupture-like events have resulted between $t = 10$ ms and $t = 100$ ms, causing multiple water globules to be trapped on the image area at steady state, as in Figure 3.5(d). Given that that typical residence times in the printing nip (region between the form roll and plate cylinder; Figure 3.1) may be ∼20-50 ms(U.S., Jul 14, 1981), our simulations suggest that there is a critical image size above which excess aqueous solution will be trapped on an image area. Using the general heuristic of $2.5\lambda_{md}$ from Figure 3.5 yields an estimate of ∼20 μm for the critical image size. For an aqueous layer of 100 nm, the critical image size would be ∼130 μm. Given that typical image sizes used in practice are in the range of $10 - 50$ μm (U.S., Aug 23, 1994), entrainment of excess aqueous solution would be expected for an initial aqueous layer thickness of 20 nm but not 100 nm.

Because the time for the first rupture-like event to occur increases as the image size decreases, the smallest image size one can use in practice will be determined by the residence time in the printing nip. If the time for the first rupture-like event is much larger than the residence time, the aqueous film will not be displaced and the

ink will not wet the image areas. For the results shown in Figure 4.20, where the aqueous layer thickness is 20 nm, the time for the first rupture-like event is ~ 20 ms. With typical residence times of $20 - 50$ ms (U.S., Jul 14, 1981), this suggests that $I \sim 20$ μm is the smallest printable image size. This is consistent with known values for typical feature sizes ($10 - 50$ μm) used in practice (U.S., Aug 23, 1994). However, if the aqueous layer thickness is 100 nm, the time for the first rupture-like event is in the range $700 - 800$ ms for image sizes $I = 10 - 50$ μm. These time scales are much longer than the estimated residence times of $20 - 50$ ms (U.S., Jul 14, 1981), suggesting that precise control of the aqueous layer thickness is crucial for obtaining good print quality.

We can also comment on how closely image areas can be placed together. If the image areas are placed too closely together, then ink may spill over onto the non-image areas (Figure 3.9). For an aqueous layer thickness of 20 nm and an image size of 20 μm, the top boundary in Figure 3.9 would occur at a non-image size of $\sim 3\lambda_{md} = 22.5$ μm, and the bottom boundary would occur at $\sim \lambda_{md} = 7.5$ μm. The former represents the minimum spacing needed to avoid any spill-over events.

We can summarize the above discussion in terms of some general principles. The problem parameters set the value of the most dangerous wavelength for a chemically homogeneous surface, λ_{md} (cf. equation (4.16)). For a given set of physical properties, λ_{md} can be adjusted through control of the aqueous layer thickness. The largest image size that can be printed without entraining excess aqueous solution is $\sim 2 - 3\lambda_{md}$. Similarly, the closest the image areas can be placed together in order to get near-perfect templating (i.e., avoid spill-over of ink onto the non-image areas) is $\sim 2-3\lambda_{md}$. The smallest image size that can be printed is set by the residence time in the nip, and the above considerations suggest that this value is $\sim \lambda_{md}$ (so as to avoid the large increase in T_e at small image sizes seen in Fig. 3.4). These principles may be useful for printing practitioners because they allow for relatively quick estimates of key quantities.

3.4.2 Wire-wound rod coating

Direct visualization liquid displacement in the lithographic printing nip is difficult because of the narrowness of the nip (< 1 μm) and the high speeds of the rollers ($\sim$1-10 m/s) (MacPhee, 1998). However, a closely related process with similar dynamics is the dewetting of a single liquid layer on a chemically patterned substrate. Here, the upper layer is air and the system does not have a bounding surface above.

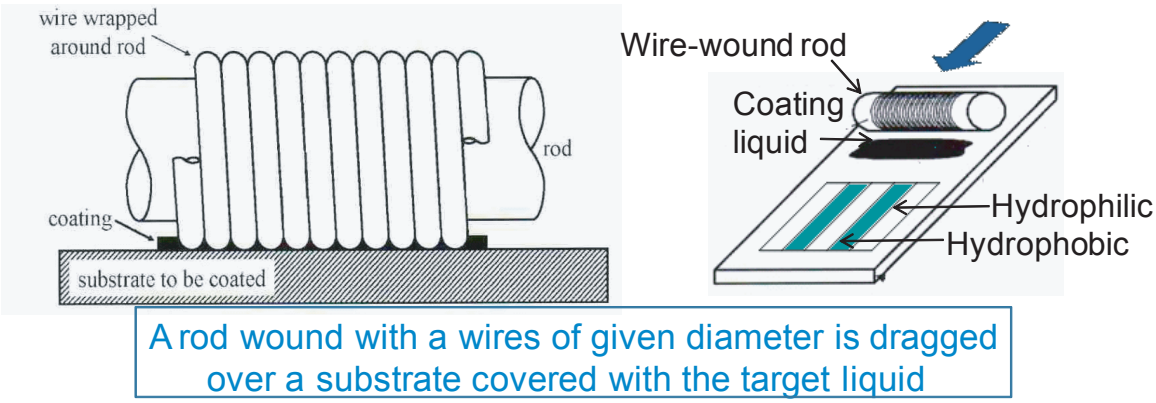

Figure 3.12: Illustration of the wire-wounding rod coating process for coating on chemically patterned surfaces.

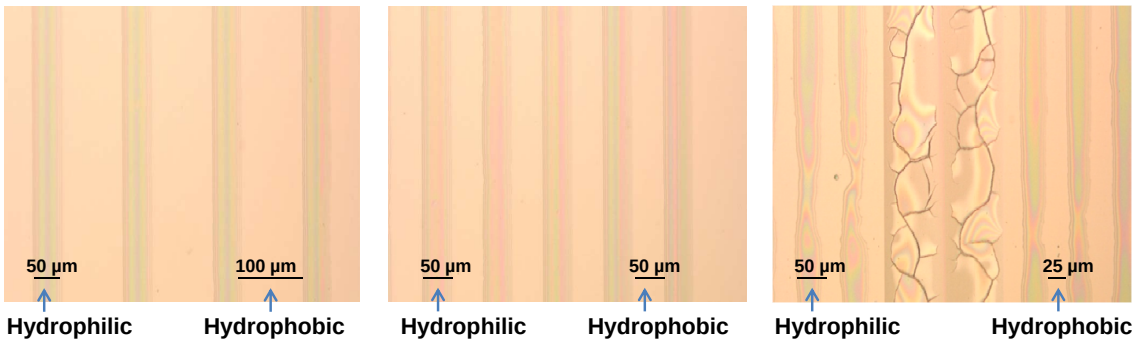

Figure 3.13: Optical microscope images of wire-wound rod coating experiments. In all images the width of the hydrophilic stripes is 50 μm. The widths of the hydrophobic stripes are 100 μm (left image), 50 μm (center image), and 25 μm (right image).

In order to better conceptualize this process, we performed a set of experiments using the wire-wound rod coating process (MacLeod, 2006), in which a thin film of coating liquid was deposited onto on a chemically patterned substrate using metering rods wound with wires of known diameters (Figure 3.12). In our experiments we used silicon substrates patterned by standard photolithographic techniques (see Ref. [42]) and coated them using a 15 wt% aqueous dispersion of silica, obtained from Cabot Corporation. Details from the manufacturer reveal that the dispersion is composed of 20 nm individual particles in open clusters with a median aggregate diameter of 150 nm. The dispersion shear thins slightly, with an average viscosity of ∼5 mPa s as reported in experimental measurements elsewhere (Reynolds et al., 2010). The solvent evaporates after coating and the dried films are imaged with an optical microscope. Figure 3.13 shows images of these coatings on substrates having hydrophilic stripes 50 μm wide, and hydrophobic stripes of given width. While a coating covering only the hydrophilic patches was obtained with substrates having hydrophobic patch widths of 100 μm and 50 μm, the coating was found to bridge two or more hydrophilic patches when the hydrophobic patch width was reduced to 25 μm or smaller. This suggests that there is a minimum spacing required to prevent the coating from bridging over the hydrophobic regions that separate adjacent hydrophilic regions.

To rationalize the experimental observations, we performed a set of nonlinear simulations for the case of dewetting of a single liquid layer on a chemically patterned surface. The viscosity ratio, μ_r, was set to zero in (3.3), and it was assumed the coating liquid had viscosity 0.001 Pa s and interfacial tension 72.8 mN/m. For the constants A_1 and B_1 we use dimensional values $A_1 = 10^{-20}$ J and $B_1 = 5$ x 10^{-29} J m, which is consistent with the range of values for most materials (see Ref. [47] and Appendix 2). Assuming that the target liquid has properties similar to water, we use $\tilde{\gamma} = 72.8$ mN/m. The initial thickness of the liquid layer was taken to be 40 nm, which yields a value of $\lambda_{md} \sim 34$ μm.

The smallest non-image size required to avoid spill-over was calculated by nonlinear simulations similar to those of section 3.3.3. For an image size of 50 μm, the non-image size at which spill-over is first eliminated (e.g., Figure 3.9, bottom boundary) was found to be ∼40 μm. The non-image size at which spill-over is completely eliminated (e.g., Figure 3.9, top boundary) was found to be ~ 160 μm. The variation of the non-image size at which spill-over is first eliminated is plotted as a function of the initial film thickness in Figure 3.14. The plot shows that the required non-image size increases monotonically as the film thickness increases. For the set of parameters used here, the non-image size is $\sim 2\lambda_{md}$ at a given film thickness.

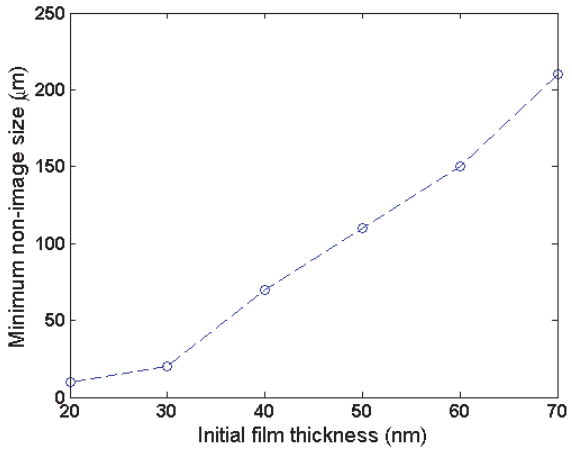

Figure 3.14: Effect of film thickness on the non-image size at which spill-over is first eliminated.

The simulation results described above are qualitatively consistent with our experimental observations. The micrographs in Figure 3.13 depict coatings on 50 μm wide hydrophilic patches using rod #18 (R. D. Specialties Inc., Webster, NY, USA), with wire spacings of 460 μm. The hydrophobic spacings in these patterns are 25 μm, 50 μm, and 100 μm. When wire-wound rod #10 with a narrower wire spacing (250 μm), leading to a smaller wet film thickness, was used to coat the same set of patterns, the bridging of coatings over the hydrophobic areas did not occur. Instead, the bridging was seen at a smaller hydrophobic spacing of 10 μm (results not shown). The behavior is therefore consistent with the simulation results in Figure 3.14 where the minimum non-image size increases with increasing film thickness. The actual values of the non-image sizes calculated from the simulations ($10 - 200$ μm) are also comparable to the width of the hydrophobic spacings in the experiments. We note that in order to comprehensively model dewetting in wire-wound rod coating, one would have to account for the larger wet thickness of the film deposited by the wire-wound rods (on the order of 10s of microns). There would then be drying, which reduces the film thickness to a point where disjoining pressure becomes active. Nevertheless, the model results are qualitatively consistent with the experimental observations, indicating that model may be a useful tool for making first estimates of various quantities in coating and printing processes involving dewetting of liquid films on chemically patterned surfaces.

3.5 Conclusions

Motivated by the process of lithographic printing, we have considered a model problem of stratified bounded two-layer flow near a chemically patterned surface. By including a repulsive component to the disjoining pressure, we have extended the prior work of Lenz and Kumar (2007a) to address the important issues of (i) post-rupture dynamics, and (ii) the influence of non-image area size.

Our results indicate that if the image areas are too wide relative to the most dangerous wavelength on a chemically homogeneous surface, large globules of water can be trapped during the liquid displacement process. If the non-image areas are too narrow relative to the most dangerous wavelength, then near-perfect templating can be destroyed. Our results enable us to obtain estimates for the smallest and largest image sizes that can be used in lithographic printing, and the smallest distances features can be separated by before print quality is compromised. In particular, the results indicate the importance of precisely controlling the aqueous layer thickness. Our results are also qualitatively consistent with experimental observations from the closely related process of wire-wound rod coating on chemically patterned surfaces.

The results presented here have important implications for the printing of electronic devices and displays, a process for which lithographic printing is an especially promising route. The results should also be applicable to other coating and printing processes involving chemically patterned surfaces. While a number of simplifications necessarily had to be made, the model we develop provides a relatively simple way to obtain estimates for important process parameters, and can serve as the basis for the development of more sophisticated models. In particular, it will be important to account for the mechanics of liquid transfer from one surface to another (e.g., from printing plate to blanket roll) as the surfaces separate, residual ink on the image areas (Lenz and Kumar, 2007b), and the influence of liquid additives on surface wettability (Hohne et al., 2008).

3.6 Appendix 1: Hamaker constants for multiple image areas on a domain

To represent a case where a domain has 4 image areas and 4 non-image areas in an alternating manner, the following expressions were used to calculate $A_1(x)$ and $B_1(x)$:

$$A_1(x) = \frac{A_1^{Im}}{\pi}\Bigg[-\tan^{-1}\Big(\frac{x-I/2}{\delta}\Big)+\tan^{-1}\Big(\frac{x-(N+I/2)}{\delta}\Big)-\tan^{-1}\Big(\frac{x-(N+3I/2)}{\delta}\Big)+$$
$$\tan^{-1}\Big(\frac{x-(2N+3I/2)}{\delta}\Big)-\tan^{-1}\Big(\frac{x-(2N+5I/2)}{\delta}\Big)+\tan^{-1}\Big(\frac{x-(3N+5I/2)}{\delta}\Big)-$$
$$\tan^{-1}\Big(\frac{x-(3N+7I/2)}{\delta}\Big)+\tan^{-1}\Big(\frac{x-(4N+7I/2)}{\delta}\Big)-\tan^{-1}\Big(\frac{x-(4N+4I)}{\delta}\Big)\Bigg], \tag{3.15a}$$

$$B_1(x) = -\frac{B_1^{Im}}{\pi}\Bigg[\tan^{-1}\Big(\frac{x-I/2}{\delta}\Big)+\tan^{-1}\Big(\frac{x-(N+I/2)}{\delta}\Big)-\tan^{-1}\Big(\frac{x-(N+3I/2)}{\delta}\Big)+$$
$$\tan^{-1}\Big(\frac{x-(2N+3I/2)}{\delta}\Big)-\tan^{-1}\Big(\frac{x-(2N+5I/2)}{\delta}\Big)+\tan^{-1}\Big(\frac{x-(3N+5I/2)}{\delta}\Big)-$$
$$\tan^{-1}\Big(\frac{x-(3N+7I/2)}{\delta}\Big)+\tan^{-1}\Big(\frac{x-(4N+7I/2)}{\delta}\Big)-\tan^{-1}\Big(\frac{x-(4N+4I)}{\delta}\Big)\Bigg]. \tag{3.15b}$$

In the simulations described throughout this paper we have used dimensionless values $A_1^{Im} = 1$, $B_1^{Im} = 1$, and $\delta = 0.005$ with expressions (3.15).

3.7 Appendix 2: Values of Hamaker constants for lithographic printing systems

The constants A_1 and B_1 characterizing the disjoining pressure are functions of surface energies of the liquids and the solid surfaces. For example, the interfacial tension γ_{ij} between any two species (solid or liquid) i and j is the sum of contributions from several components (Fowkes, 1962) such as van der Waals forces, polar forces, hydrogen bonding, and metallic bonding:

$$\gamma_{ij} = \sum_{k=1}^{n} \gamma_{ij}^{k}, \tag{3.16}$$

where k represents a particular interaction type.

The relationships between constants like A_1 and the van der Waals or polar components of surface tension has been explained in detail by Oss et al. (1988). The constant A_1 that measures the van der Waals interaction between the liquid-liquid interface and the surface 3 may be related to the van der Waals component of the

spreading coefficient S^{VW} as:

$$A_1 = -12\pi d_0^2 S^{VW}, \tag{3.17}$$

where d_0 is the equilibrium molecular separation and S^{VW} is defined by:

$$S^{VW} = \gamma_{23}^{VW} - \gamma_{12}^{VW} - \gamma_{13}^{VW} \tag{3.18}$$

Analogous to (3.18), the polar spreading coefficient S^P is defined as:

$$S^P = \gamma_{23}^P - \gamma_{12}^P - \gamma_{13}^P. \tag{3.19}$$

In order to relate B_1, which denotes the short-range repulsion which may arise due to polar forces, to the polar spreading coefficient S^P, we use the expression for the polar component of the excess free energy described in prior work (Sharma, 1993; Oss et al., 1988; Sharma and Khanna, 1999; Kargupta and Sharma, 2002b; Sharma et al., 2003; Israelachvili and Adams, 1978). The derivative of the excess free energy gives the disjoining pressure potential, which we have modeled in this current work using the term $\frac{B_1}{h^4}$ which incorporates the fourth power alone. A best-fit estimate for B_1 may be obtained by plotting the two expressions as function of h for various values of B_1:

$$\frac{S^P}{l_p}\exp\Big(\frac{d_0 - h}{l_p}\Big) = \frac{B_1}{h^4}, \tag{3.20}$$

where l_p in (3.20) is a characteristic length scale known as a correlation length.

The surface energetics of lithographic printing plates, inks, and aqueous fountain solutions have been characterized experimentally by Kaelble and Dynes (1975). We use values from these reported measurements for obtaining the polar and van der Waals components of lithographic plates, inks, and fountain solutions as listed in Table 2.

Table 3.2: Estimates of surface tension values from Kaelble and Dynes (1975)

	Material	**Polar component (dyn/cm)**	**Van der Waals component (dyn/cm)**
1.	Aqueous fountain solution (20 vol%)	$\gamma_1^P = 20$	$\gamma_1^{VW} = 23$
2.	Lithographic plates	$\gamma_2^P = 20$	$\gamma_2^{VW} = 27$
3.	Inks	$\gamma_3^P = 5$	$\gamma_3^{VW} = 30$

The interfacial tension γ_{ij} between substances i and j which do not differ widely

in their polarizabilities may be represented by a harmonic mean of the individual surface tensions: (Wu, 1971)

$$\gamma_{ij} = \gamma_1 + \gamma_2 - \frac{4\gamma_1\gamma_2}{\gamma_1}\gamma_2. \tag{3.21}$$

Using (3.21) we obtain $\gamma_{12}^P = 40$, $\gamma_{13}^P = 16$, $\gamma_{23}^P = 16$, $\gamma_{12}^{VW} = 49.7$, $\gamma_{23}^{VW} = 52.1$, and $\gamma_{13}^{VW} = 56.8$ where all values are in dyn/cm. Using (3.18) and (3.19), the values of the spreading coefficients are calculated as $S^P = 8$ dyn/cm and $S^{VW} = -59.2$ dyn/cm. Further using (3.17) and (3.20), along with the values of the constants (Oss et al., 1988) $l_p = 0.6$ nm, $d_0 = 1.58$ Å, the Hamaker constants A_1 and B_1 can be estimated as $A_1 \sim 10^{-20}$ J and $B_1 \sim 5$ x 10^{-29} J m.

CHAPTER 4

Thermally induced delay and reversal of liquid film dewetting on chemically patterned surfaces

A thin liquid film resting on a solid substrate that is heated or cooled from below experiences surface tension gradients, or Marangoni effects. Here we explore the dewetting of such a film resting on a chemically patterned surface, under the combined action of Marangoni effects and intermolecular forces. A nonlinear differential equation for the film height based on lubrication theory is solved numerically incorporating both the wettability gradient effects and the Marangoni effects. The results suggest that combined localized heating and cooling may be used to modify the film rupture dynamics induced by the disjoining forces and cause rupture at desired locations. This physical phenomenon provides a handle to deposit liquids on surfaces whose wettability is difficult to control. The mechanisms of competitive dewetting in presence of Marangoni effects and the wettability gradients are analyzed by considering different spatial variations of both the effects. The work presented here has special practical relevance for manipulating liquid flow in industrial applications like templating, coating and printing processes, and microfluidics.

4.1 Introduction

Thermally-induced Marangoni flows on chemically patterned surfaces is especially important from current industrial standpoint. As printed electronic devices may

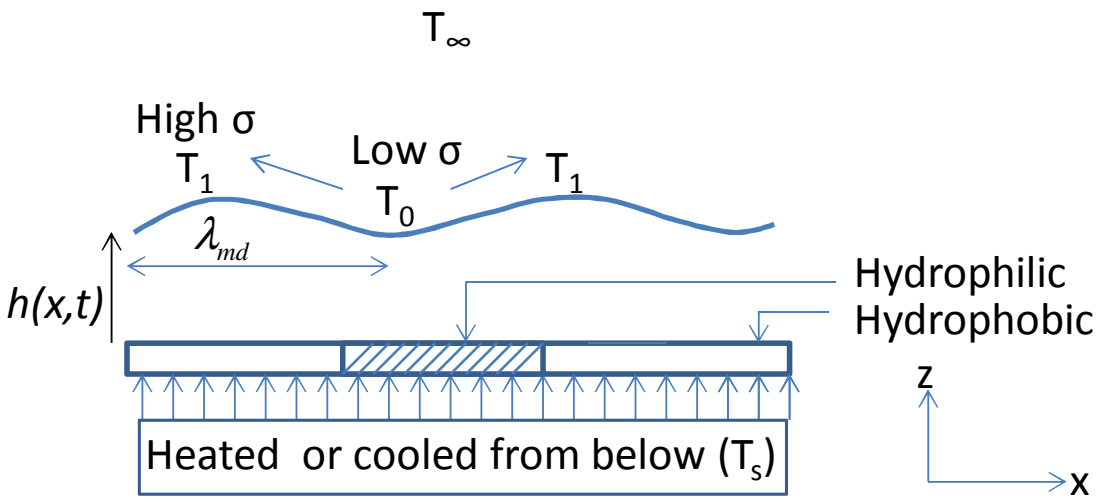

Figure 4.1: The problem setup

promisingly be fabricated on chemically patterned substrates through coating and printing processes (Leyland et al., 2002; Hay et al., 2005; Southee et al., 2007; Ramsey et al., 2007; Hay et al., 2007; Arase and Nakagawa, 2009; Nuzzo et al., Nov 24, 2009), thermal effects would significantly impact the associated liquid flow dynamics. Temperature variations can be introduced in these flows by means of programmable heating or cooling devices, resulting in surface-tension gradients, and subsequent thermocapillary-driven flows. Additionally, the potential use of thermocapillary effects for routing liquid microstreams in chemically patterned microfluidic devices is noteworthy (Darhuber et al., 2003a,b; Darhuber and Troian, 2005; Gunther and Jensen, 2006; Paik et al., 2008). In these systems the liquid is confined to selected pathways by chemical patterning, and the temperature gradients provide control over the direction, timing, and flow of liquid. Emerging applications thus provide a compelling motivation for the investigation of thermocapillary-driven flows on chemically patterned surfaces.

The dynamics of ultrathin liquid films ($<\sim$ 100 nm) is specially relevant to the applications discussed above. When these ultrathin films dewet, intermolecular forces (e.g., van der Waals forces) play a pivotal role in the dewetting process. Additionally, if the thin film were to dewet on a chemically patterned solid surface, wettability gradients would drive flow (Lenz and Kumar, 2007a; Kargupta et al., 2000; Kargupta and Sharma, 2002b,c, 2003; Thiele et al., 2003; Brusch et al., 2002; Kao et al., 2006; Brasjen and Darhuber, 2011). This situation is typically modeled in thin-film literature by spatially varying the strength of intermolecular forces (Kargupta et al.,

2000; Konnur et al., 2000; Kargupta and Sharma, 2002b,c; Zope et al., 2001; Lenz and Kumar, 2007a; Kalpathy et al., 2010), which would inform the liquid about the wettability of the surface. Further, if temperature variations are present within the film (e.g., see Figure 4.1) surface tension gradients would also drive flow from the warmer to the cooler regions. The setup therefore results in competing dewetting forces due to the wettability and its gradients, and the surface tension gradients or Marangoni flows. A mathematical model examining these competitions is the subject of the present work.

Given that thermocapillary forces can significantly affect the dynamics of thin-film evolution, temperature variations along the film surface may be introduced either by a uniform heating or cooling of the system, or through restricted heating or cooling of certain parts of the chemically patterned solid surface. The latter design offers tremendous flexibility to manipulate the stability of the film by spatially controlling the dewetting forces. In this case, the width of the heated or cooled region of the solid relative to the length scales of the wettability-based chemical pattern becomes important in determining the instability mechanism. The envisioned configuration may be implemented in practice by the use of microheaters (Darhuber et al., 2003b) or adaptive cooling techniques (Paik et al., 2008). Adaptive cooling refers to the use of cooling systems which can dynamically cool different areas of a substrate at different rates. Such techniques may be set up by the use of various cooling approaches like forced convection-based cooling (e.g., fans and nozzles), refrigerators (e.g., Peltier/thermoelectric coolers), or microfluidic-based cooling. For instance, allowing a pressurized supply of cooling liquid through minute flow channels with hydraulic diameters in the range $10 - 30$ μm has been fabricated in the past (Tuckerman and Pease, 1981) for cooling thin silicon chips used in integrated circuits. On the other hand, state-of-the art microheaters may be constructed using a series of microline resistors (Yang and Tsutsui, 2000) which are typically $50 - 100$ μm wide. These length scales are consistent with characteristic sizes of pixels in printed electronic displays or channel widths in microfluidic devices. Industrial applications as well as fundamental physics therefore make the examination of Marangoni flows of thin films on chemically patterned surfaces needful and valuable.

Before proceeding, it is important to point out that several prior researchers have addressed various nonlinear aspects of thermocapillary instabilities in thin liquid films. The review by Davis (1987) provides a good starting point description of the mechanics and behavior of thermocapillary instabilities in simple planar systems. The ideas therein have been utilized to show evidence of rupture of a thin film due to

thermocapillary-driven flows experimentally (VanHook et al., 1997; Burelbach et al., 1990) as well as numerically in both one- and two-dimensions (Burelbach et al., 1988; Oron and Rosenau, 1994; Krishnamoorthy and Ramaswamy, 1995). Oron (2000) later extended these studies to observe growing complexity in the two-dimensional interfacial evolution depending on the choice of randomness in the initial condition imposed. Notably, the combination of thermocapillary stresses and intermolecular forces (conjoining/disjoining pressures (Israelachvili, 1992)) for chemically homogeneous surfaces was studied by Burelbach et al. (1988) in a single-layer one-dimensional set up and by Merkt et al. (2005) and Nepomnyashchy and Simanovskii (2007) for two-layer systems in two dimensions. A weakly nonlinear analysis in one dimension has also been described by Oron and Bankoff (1999b). The study by Merkt et al. (2005) and Golovin et al. (2001) note the crucial result that thermocapillarity could act as both stabilizing and destabilizing factors depending on the relative strength of other effects like gravity and intermolecular forces.

Though there have been considerable amount of prior studies to understand thermocapillary effects in thin films, the configurations considered are mostly liquid films resting on chemically homogeneous solid surfaces. As described above, chemical patterning of the solid surface and the combined possibility of localized temperature variations lead to further complexity arising from competitions between the forces that cause dewetting. Optimal leveling of single-layer flows over topographically patterned surfaces by spatial control of thermocapillary effects has been demonstrated by Gramlich et al. (2002). However, the problem that we examine here is different from theirs, as we assume the surface to be chemically patterned based on wettability differences, while in their problem only variations in substrate topography was considered leading to capillary ridges and troughs.

The rest of the paper is organized as follows: Section 2 describes the problem formulation along with details about the numerical methods used. A brief summary of the linear stability analysis is also presented. Section 4.3 presents and discusses key results from nonlinear simulations, and conclusions are noted in section 4.4.

4.2 Mathematical model

4.2.1 *Governing equations*

As a model problem, we consider a thin film of a Newtonian liquid on a solid surface which may be chemically patterned, with a passive gaseous layer above the liquid

(Figure 4.1). The solid surface is maintained at a temperature T_s, different from the ambient gas phase temperature T_∞, leading to temperature differences within the film. We assume the mean height of the liquid film h_{tot} to be much smaller than λ_{md}, the wavelength of a typical interfacial perturbation that grows the fastest on a chemically homogeneous surface, i.e., $\epsilon = \frac{h_{tot}}{\lambda_{md}} \ll 1$. This assumption allows us to employ the lubrication approximation which would considerably simplify the governing equations. For convenience, we non-dimensionalize the physical quantities in the problem as follows:

$$x = \frac{\epsilon\tilde{x}}{h_{tot}}, \qquad z = \frac{\tilde{z}}{h_{tot}}, \qquad u = \frac{\tilde{u}\tilde{\rho}h_{tot}}{\tilde{\mu}}, \qquad w = \frac{\tilde{w}\tilde{\rho}h_{tot}}{\epsilon\tilde{\mu}}. \tag{4.1}$$

Here x and z are position variables in the horizontal and the vertical directions, respectively, and u and w are the corresponding velocity components. Variables with a tilde are dimensional quantities. The density is denoted by $\tilde{\rho}$ and the viscosity by $\tilde{\mu}$. Time, temperature, pressure, and surface tension are non-dimensionalized as follows:

$$t = \frac{\epsilon\tilde{t}\mu}{h_{tot}^2\tilde{\rho}}, \qquad T = \frac{\tilde{T} - \tilde{T}_\infty}{\tilde{T}_s - \tilde{T}_\infty}, \qquad (p, \phi) = (\tilde{p}, \tilde{\phi})\frac{\epsilon h_{tot}^2\tilde{\rho}}{\tilde{\mu}^2}, \qquad \sigma = \frac{\epsilon\tilde{\sigma}\tilde{\rho}h_{tot}}{\tilde{\mu}^2} \tag{4.2}$$

Here, t denotes time, T denotes temperature, p denotes the dynamic pressure, σ denotes the surface tension, and ϕ is the dimensionless potential for the disjoining pressure.

Motivated by prior work (Oron and Bankoff, 1999b; Brasjen and Darhuber, 2011) which models the evolution of thin liquid films under the action of attractive and repulsive intermolecular forces, we use the following power-law form to describe ϕ:

$$\phi = \frac{H_1}{h^3} - \frac{H_2}{h^4}, \tag{4.3}$$

where H_1 and H_2 are dimensionless parameters (commonly referred to as Hamaker constants) governing the magnitude of attraction between the liquid-air interface and the solid substrate. The scalings for the Hamaker constants are $H_1 = \epsilon\tilde{H}_1\tilde{\rho}/\tilde{\mu}^2 h_{tot}$ and $H_2 = \epsilon\tilde{H}_2\tilde{\rho}/\tilde{\mu}^2 h_{tot}^2$, and they can in general assume either positive or negative values. The intermolecular force potential ϕ is therefore a sum of long-range and short-range forces. For H_1, $H_2 > 0$, the term $\frac{H_1}{h^3}$ would in general denote an attractive force that has its origin in the $\frac{1}{r^6}$ form of the London van der Waals molecular interactions,(Hamaker, 1937) where r is a molecular separation distance. On the other hand, $\frac{H_2}{h^4}$ is a short-range repulsive potential arising from polar forces (van

Oss et al., 1987) (e.g., hydration pressure, structural forces, hydrophobic interactions). The power h^4 is chosen here as a representative value, while higher powers like h^8 have also been used by previous authors (Kargupta et al., 2000; Khanna and Sharma, 1997). As well known in thin film literature, the repulsive force potential would prevent a complete interfacial rupture and instead thin the interface down to an equilibrium film thickness H_1/H_2.

The dimensionless x and z components of the momentum balance for the liquid in the lubrication limit are respectively given by:

$$\partial_z^2 u = \partial_x p + \partial_x \phi, \tag{4.4}$$

$$0 = \partial_z p + \partial_x \phi. \tag{4.5}$$

The dimensionless form of the normal and tangential stress balance conditions in the lubrication limit are expressed as:

$$-p = \bar{C}\partial_x^2 h, \tag{4.6}$$

$$\partial_z u = \partial_x \sigma, \tag{4.7}$$

where $\bar{C} = \frac{\tilde{\rho} h_{tot} \tilde{\sigma_0} \epsilon^3}{\tilde{\mu}^2}$ is a dimensionless parameter, commonly referred to as an inverse capillary number. The inverse capillary number $\bar{C}$ is expressed in terms of the parameter $\tilde{\sigma_0}$, the dimensional surface tension at the free interface of the liquid layer corresponding to the region of maximum temperature. Since the surface tension in this problem is temerature-dependent, the normal stress boundary condition would in reality consist of two terms arising from capillarity and the Marangoni effects. However, the potential effects of Marangoni stresses is ignored and only the capillary term is retained in (4.6) by scaling the inverse capillary number by ϵ^3. A similar procedure has been adopted by Kumar and Matar (2002) in the investigation of instabilities due to Marangoni effects arising from surfactants.

In order to determine the thermocapillary stress $\partial_x \sigma$, an energy equation and the appropriate boundary conditions related to heat transfer are needed. The energy equation in lubrication form is

$$\partial_z^2 T = \partial_t T + u\partial_x T + w\partial_z T, \tag{4.8}$$

where $T = 1$ for $z = 0$. The Newton's cooling law boundary condition is invoked at

$z = h(x,t)$, which reads: (Oron et al., 1997)

$$\partial_z T + BT = 0 \tag{4.9}$$

in dimensionless form when simplified by the lubrication approximation. Here $B = \frac{\alpha_{th} h_{tot}}{k_{th}}$ is a dimensionless Biot number where α_{th} is the heat transfer coefficient describing the rate of heat transfer from the liquid to the ambient gas phase at temperature T_∞ while k_{th} is the thermal conductivity of the liquid. The physical significance of the Biot number may therefore be understood as the ratio of the rate of heat convection from the liquid to the ambient gas phase to the rate of heat conduction within the liquid.

The energy equation is solved to obtain the temperature distribution, and the thermocapillary stress may be found to be:

$$\begin{aligned} \partial_x \sigma &= m \frac{d\sigma}{dT} \Big(\partial_x T + (\partial_x h)(\partial_z T) \Big) \\ &= m \frac{d\sigma}{dT} \frac{\partial_x h}{(1+Bh)^2}. \end{aligned} \tag{4.10}$$

The dimensionless parameter $m = \frac{\Delta\tilde{\sigma}\epsilon h_{tot}}{\tilde{\mu}\tilde{\kappa}}$ in (4.10) arises by virtue of the fact that the surface tension is a temperature-dependent physical quantity. Here $\tilde{\kappa}$ is the dimensional thermal diffusivity of the liquid and $\Delta\tilde{\sigma}$ is the difference in surface tension of the liquid between the temperatures T_∞ and T_s. The quantity $\Delta\tilde{\sigma}$ is positive when there is a decrease in surface tension caused by heating the solid surface from below ($T_\infty < T_s$). Likewise, $\Delta\tilde{\sigma}$ will be negative when the solid surface is cooled from below ($T_\infty > T_s$). Setting $B \ll 1$, and using the no-slip, the no-penetration, the kinematic boundary conditions, and equations (4.6),(4.7),(4.10), the momentum balance equations may be solved to obtain a single nonlinear dimensionless equation governing the height of the air-liquid interface:

$$\partial_t h + \frac{1}{2} mB \partial_x (h^2 \frac{d\sigma}{dT} \partial_x h) + \frac{1}{3} \bar{C} \partial_x (h^3 \partial_x^3 h) - \frac{1}{3} \partial_x (h^3 \partial_x \phi) = 0. \tag{4.11}$$

This equation (4.11) is consistent with the evolution equation presented by Burelbach et al. (1988) in the limit of a non-volatile liquid. Assuming a standard linearly decreasing function for $\sigma(T)$ implies that the value $\frac{d\sigma}{dT}$ is constant. We set the product mB in (4.11) to a single constant M, which will be referred to henceforth as the Marangoni number:

$$M = \frac{\Delta\tilde{\sigma}\epsilon h_{tot}^2 \alpha_{th}}{\tilde{\mu}\tilde{\kappa}k_{th}}. \tag{4.12}$$

Table 4.1: Typical values of the physical quantities present in M, H_1, and H_2

Quantity	Symbol	Typical values
Hamaker constant (Israelachvili, 1992)	$\tilde{H}_1$	$10^{-19} - 10^{-21}$ J
Hamaker constant (Kaelble and Dynes, 1975)	$\tilde{H}_2$	$10^{-27} - 10^{-29}$ J m
Density	$\tilde{\rho}$	10^3 kg m^{-3}
Dynamic viscosity	$\tilde{\mu}$	1 x 10^{-3} N m s^{-2}
Lubrication parameter	ϵ	$10^{-2} - 10^{-4}$
Mean film thickness	h_{tot}	$10^{-5} - 10^{-8}$ m
Change in surface tension (Kayser, 1975)	$\Delta\tilde{\sigma}$	15 x 10^{-3} N m^{-1} for ΔT$\sim$100 K
Thermal conductivity (Ramires et al., 1994)	k_{th}	0.6 W m^{-1} K^{-1}
Heat-transfer coefficient (Wayner et al., 1976)	α_{th}	$10^2 - 10^4$ W m^{-2} K^{-1}
Thermal Diffusivity (James, 1968)	$\tilde{\kappa}$	1.4 x 10^{-7} m^2 s^{-1}

Further setting $\frac{d\sigma}{dT} = 1$ in 4.11, and using (4.3), the evolution equation (4.11) becomes:

$$\partial_t h + \frac{1}{2} M \partial_x (h^2 \partial_x h) + \frac{1}{3} \bar{C} \partial_x (h^3 \partial_x^3 h) - \frac{1}{3} \partial_x \Big[h^3 \partial_x \Big(\frac{H_1}{h^3} - \frac{H_2}{h^4} \Big) \Big] = 0. \tag{4.13}$$

By the definition of $\Delta\tilde{\sigma}$ in (4.10), a positive value of M in (4.12) would refer to heating effects and a negative M would refer to cooling effects.

Table 1 lists typical dimensional values of the various physical quantities present in the dimensionless Marangoni number M and the Hamaker constants H_1 and H_2 for aqueous systems. Estimates for the realistic values of M may be obtained as $10^{-6} - 10^{-1}$ for thin film systems ($<$1 μm) and $10^{-1} - 10^{4}$ for thicker films. Marangoni numbers for non-aqueous systems would also typically fall in a similar range. Using the parameters listed in Table 1, realistic dimensionless values for H_1 and H_2 may be estimated to be in the range $10^{-4} - 10^{-10}$. Likewise, typical values of the capillary parameter $\bar{C}$ may be calculated to be $\sim 10^{-3} - 1$. For the results presented in this paper, we scale up the four parameters H_1, H_2, M, and $\bar{C}$ to the range $10^{-2} - 10^{2}$, while maintaining realistic ratios between them. This greatly reduces the computational cost involved in the calculations by allowing us to use a smaller simulation domain length, which is measured in terms of λ_{md}, the fastest growing wavelength of a typical interfacial perturbation on a chemically homogeneous surface (see section 4.2.2). Besides, we note that most prior discussions (Merkt et al., 2005; Oron, 2000; Nepomnyashchy and Simanovskii, 2007; Oron and Bankoff, 1999b; Burelbach et al., 1988) on thermocapillary-driven thin film instability are based on dimensionless values for M, H_1, H_2, and C in the similar range as used in the present work. However, to ensure the practical validity of these results, we conducted a limited set of runs using

realistic parameter sets determined by the values in Table 1, and found qualitative features similar to the results presented in section 4.3.

4.2.2 *Linear Stability Analysis*

Prior investigations have described in detail the application of standard linear stability analysis in similar problems involving thermocapillary instabilities (Burelbach et al., 1988; Oron and Bankoff, 1999b). For completeness, we choose to state here the key results alone.

Linearization of the evolution equation (4.13) gives the growth rate α of an interfacial perturbation on a chemically homogeneous surface

$$\alpha = -\frac{1}{3}\bar{C}k^4h_0^3 + \frac{1}{2}Mk^2h_0^2 + \frac{H_1k^2}{h_0} - \frac{4H_2k^2}{3h_0^2}, \tag{4.14}$$

where h_0 is the initial film thickness and k is the wavenumber of the perturbation. The interface is always stabilized for values $k > k_c$, and always destabilized for values $k < k_c$ where k_c is the cut-off wavenumber obtained by setting $\alpha = 0$, which gives

$$k_c = \sqrt{\Big[\frac{3M}{2} + \frac{3H_1}{h_0^3} - \frac{4H_2}{h_0^4}\Big]\frac{1}{\bar{C}h_0}}. \tag{4.15}$$

The wavenumber of the fastest growing perturbation, or the most dangerous wavenumber k_{md} is obtained by setting $\frac{\partial\alpha}{\partial k} = 0$. For a base state $h_0 = 1$, the corresponding most dangerous wavelength λ_{md} is:

$$\lambda_{md} = 2\pi\sqrt{\frac{4\bar{C}}{3M + 6H_1 - 8H_2}}. \tag{4.16}$$

As (4.14) suggests, the thermocapillary effects can have both stabilizing and destabilizing effects depending on whether the Marangoni number M is positive or negative. Positive values of M, (i.e., heating effects) would lead to accelerated growth of perturbations and broaden the range of unstable modes, while negative M (i.e., cooling effects) would narrow the range of unstable modes which arise only due to the positive Hamaker constant H_1. On a chemically homogeneous surface, a stable uniform film would always result when $M < -2H_1 + \frac{8}{3}H_2$, as the overall growth rate (4.14) would become negative.

4.2.3 *Numerical methods*

Direct nonlinear simulations were performed using the nonlinear evolution equation (4.13) using the time-integration package DASSL (Differential Algebraic System Solver), and spatial discretization was performed using the centered finite difference method. An initial condition with random phases and random wavelengths ranging from $\lambda_{md}/100$ to $3\lambda_{md}$ was used to perturb the stationary interface, with a mean wave amplitude of 0.01. Mass conservation was ensured by observing that the mean interface height varied by less than 0.2% during the course of the simulation runs. Simulation results were first validated using linear theory predictions (section 4.2.2) for chemically homogeneous surfaces and good agreement for λ_{md} and the initial growth rate were obtained. Simulations with chemically patterned surfaces, where spatial variation of H_1, H_2, and M are involved, demanded $\sim 300 - 500$ nodes per dimensionless unit of the simulation domain to ensure mass conservation. Interfacial rupture was assumed when the film height decreased to smaller than 1 x 10^{-3}. Periodic boundary conditions were used in all cases.

The spatial variation of H_1, H_2, and M was modeled by using modified forms of algebraic functions similar to that used in prior work (Stillwagon and Larson, 1988; Lenz and Kumar, 2007a; Kalpathy et al., 2010). A typical variation of $H_1(x)$ as in Figure 4.6(a) (see section 4.3.2), may be modeled by the function (4.17) below:

$$H_1(x) = \frac{H_0}{\pi}\left[\tan^{-1}(\frac{x + w_h/2}{\delta}) - \tan^{-1}(\frac{x - w_h/2}{\delta})\right]. \tag{4.17}$$

Here H_0 is a constant set to the desired maximum value of $H_1(x)$, δ is the transition width between the hydrophobic and hydrophilic patches on the chemically patterned surface, and w_h is the width of the hydrophobic patch at the center of the domain. For the simulations presented in this paper, we use $\delta = 0.01$ in all cases. The corresponding variation of the Marangoni number $M(x)$ in Figure 4.6 is modeled as:

$$M(x) = \frac{2M_0}{\pi}\left[\tan^{-1}(\frac{x + w_M/2}{\delta}) - \tan^{-1}(\frac{x - w_M/2}{\delta})\right] - M_0 \tag{4.18}$$

where w_M is the width of the heated region, δ is set to 0.01, and M_0 is a constant which may be set to the desired value of $M(x)$ at the edges of the domain.

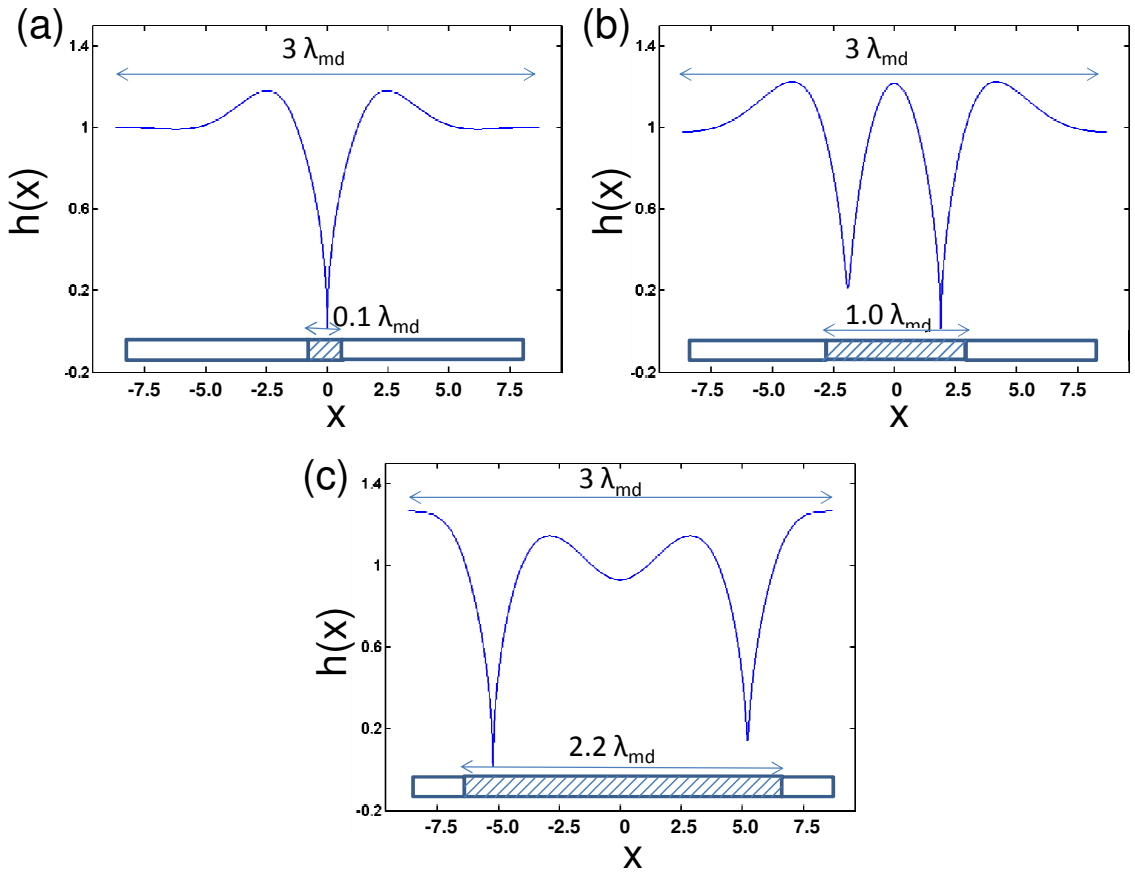

Figure 4.2: Interface profiles at rupture for three different hydrophobic patch widths: (a) $0.1\lambda_{md}$, (b) $1.0\lambda_{md}$, and (c) $2.2\lambda_{md}$. In each case, $\bar{C} = 1$, $H_2 = 0$, and $M = 0$ uniformly throughout the domain. The variation of $H_1(x)$ is represented by the function (4.17) (see section 4.2.3) with $H_1 \to 1$ at the hydrophobic patch (hatched areas) and $H_1 \to 0$ on the hydrophilic areas (unhatched areas).

4.3 Results and Discussion

The results from the nonlinear simulations are presented in this section. As noted in section 4.2.1, when a repulsive intermolecular force potential is present (i.e., $H_2 > 0$, see (4.3)) as one of the forces which drives dewetting, the interface thins down to an equilibrium film thickness instead of rupturing completely. First we present and discuss results for the case $H_1 > 0$, $H_2 = 0$. Here we distinguish between two situations where the Marangoni number is uniform across the domain corresponding to uniform heating or cooling (section 4.3.1) and when the Marangoni number is spatially varied throughout the domain (section 4.3.2). Finally, in section 4.3.3 we focus on the the case $H_2 > 0$ and the corresponding results are compared with those in the absence of any thermocapillary effects.

For the sake of completion we review the results for the case $M = 0$ discussed in prior work on instabilities driven by intermolecular forces (Kargupta et al., 2000; Zope et al., 2001). Figure 4.2 shows interface profiles at rupture for three different spatial profiles of $H_1(x)$ when $M = 0$ uniformly throughout the domain. In each case, $\bar{C} = 1$, $H_2 = 0$, and the domain size is $3\lambda_{md}$ calculated using (4.16), assuming chemically homogeneous surfaces. The strength of the attractive intermolecular force $H_1(x)$ is represented by the function (4.17) (see section 4.2.3) with $H_1 \to 1$ at the center of the domain (hatched areas) for widths $w_h = 0.1\lambda_{md}$, $1.0\lambda_{md}$, and $2.2\lambda_{md}$, in figures 4.4 (a)-(c) respectively. In each case, $H_1 = 0$ elsewhere in the domain (unhatched areas), so that the air-liquid interface is more attracted towards the center of the bottom solid surface, rendering the unhatched areas more wettable by the liquid. For convenience, we may assume that the liquid is aqueous, so that the central patch of width w_h (hatched areas) is hydrophobic, and the sides (unhatched areas) are hydrophilic. This convention will be followed throughout the rest of this paper.

As Figure 4.2(a) depicts, the film ruptures at the center in for the smallest hydrophobic patch size $w_h = 0.1\lambda_{md}$, as the wettability gradients perfectly cooperate with the wettability-driven rupture. As the hydrophobic patch is widened (figure 4.2(b)), high interfacial curvatures resulting from capillary-driven flow out of the patch traps a large droplet of the liquid in the center, and the film tends to rupture at two separate locations within the two edges of the hydrophobic patch, driven by the wettability gradients (i.e., spatial gradients in H_1). For $w_h = 2.2\lambda_{md}$, two independent ruptures form at the patch edges as the wettability gradients primarily drive flow. In what follows we probe the effect of Marangoni forces by setting M to be non-zero.

4.3.1 *Uniform heating and cooling*

Linear stability analysis (section 4.2.2) suggests that negative values of M (modeling uniform cooling) will dampen interfacial perturbations in a thin film on a chemically homogeneous surface. Prior work suggests that uniform cooling can be used as a strategy to stabilize a thin liquid film on chemically homogenous surfaces even with large amplitude perturbations, causing the free surface to stabilize into a basic flat film (Miladinova et al., 2002). However, when the solid surface is chemically patterned (as in Figure 4.1), wettability gradients drive flow. Therefore the flat film is not a steady state solution even when $M = 0$ in the evolution equation (4.13). Herein, we probe the applicability of cooling to stabilize such wettability-gradient-driven flows.

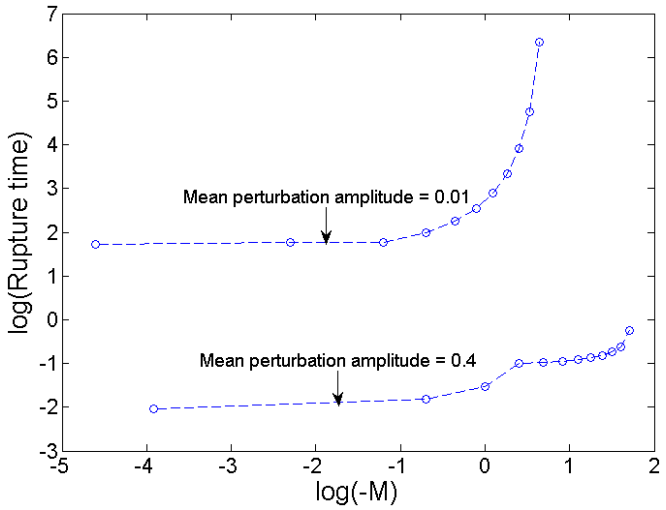

Figure 4.3: (a) Time to rupture as a function of $-M$ using initial perturbations with mean amplitudes of 0.01 and 0.4. In these calculations, the variation of $H_1(x)$ is represented by the function (4.17) (see section 4.2.3) with $H_1 \to 1$ at the hydrophobic patch (hatched areas) and $H_1 \to 0$ on the hydrophilic areas (unhatched areas). Further we set $w_h = 1.1\lambda_{md}$, $\bar{C} = 1$, and $H_2 = 0$.

Our simulations showed that for constant M, values in the range $-2H_1 < M < 0$ would only mimick the dynamics of thin film evolution subject to intermolecular forces without any Marangoni effects (Kargupta et al., 2000; Zope et al., 2001), as in Figure 4.2. However, a decrease in M beyond a point causes a sharp increase in the rupture time, by factors of 10^3 or larger, even in the presence of wettability gradients. Within the time scale of the simulations, the mean interface height in such cases was found to be always greater than 0.99 h_0 at $t = T_r'$ x 10^3, where T_r' is the corresponding rupture time for the case $M = 0$. Figure 4.3 shows the variation of rupture time as a function of the negative Marangoni number, plotted on a log-log scale for better legibility, for two different mean amplitudes of the initial perturbation. In these calculations, we used $H_2 = 0$, and $C = 1$. As for Figure 4.2, the variation of $H_1(x)$ is represented by the function (4.17) (see section 4.2.3) with $H_1 \to 1$ at the hydrophobic patch (hatched areas) and $H_1 \to 0$ on the hydrophilic areas (unhatched areas). The hydrophobic patch width w_h is set to $1.1\lambda_{md}$. The plots clearly show an increase in the rupture time with a decrease in M, and the sharp delay in rupture by factors of 10^3 is clearly seen for the smaller perturbation amplitude of 0.01. This transition occurs at $M \sim -2H_1$ for the mean amplitude of 0.01, and the corresponding critical value of M is decreased as larger amplitude perturbations are used as the initial condition. Tracking the the variation of the minimum interfacial height, as well as

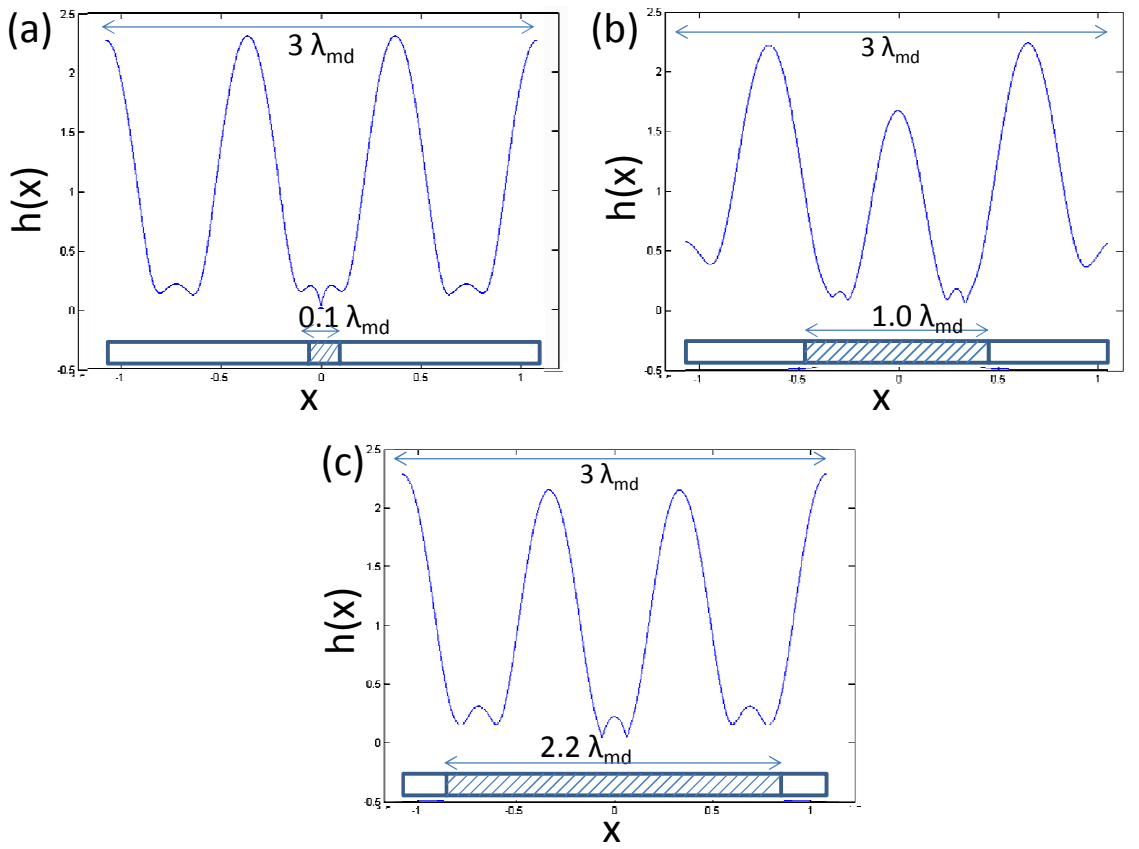

Figure 4.4: Interface profiles at rupture for three different hydrophobic patch widths: (a) $0.1\lambda_{md}$, (b) $1.0\lambda_{md}$, and (c) $2.2\lambda_{md}$. In each case, $\bar{C} = 1$, $H_2 = 0$, and $M = 100$ uniformly throughout the domain. The variation of $H_1(x)$ is represented by the function (4.17) (see section 4.2.3) with $H_1 \to 1$ at the hydrophobic patch (hatched areas) and $H_1 \to 0$ on the hydrophilic areas (unhatched areas).

the film height at a randomly chosen point on the central hydrophobic patch showed a monotonic decrease in height as a function of time. This suggests that the film may rupture in finite time, beyond the time scale of the current simulations. Nevertheless, these results indicate that cooling would still be a useful strategy to considerably delay rupture even in presence of wettability-gradients, if not completely stabilize the film. A delay in rupture by time scales of the factor of 10^3 or more as found here would prove crucial in industrial applications like continuous coating processes where intentional film rupture is engineered on chemically patterned substrates.

We now turn to a corresponding analysis with $M > 0$, modeling uniform heating of the bottom surface in Figure 4.1. While values of $M > 0$ will promote the van-der-Waals-driven instability, here we are interested in determining the extent to which heating-induced Marangoni effects influences the rupture profiles. Figure 4.4 shows

interface profiles at rupture for three different hydrophobic widths when $M = 100$ uniformly throughout the domain with $\bar{C} = 1$ and $H_1(x)$ varying as before for the case $M = 0$ (Figure 4.2). Figure 4.4 illustrates film rupture at the center in (a) ($w_h = 0.1\lambda_{md}$), with a point-like contact on the substrate, which resembles the structure in the corresponding plot with $M = 0$ (Figure 4.2(a)). For $w_h = 1.0\lambda_{md}$ also, a frustrated interface profile results as before due to the conflict between the driving forces. Here, and in Figure 4.4(c), we find that the rupture occurs with the formation of fingering-like effects instead of a point-contact rupture in Figure 4.4(a). This has been observed in prior work both numerically (Joo et al., 1991; Krishnamoorthy and Ramaswamy, 1995; Oron, 2000) and experimentally (VanHook et al., 1997). Such fingering effect is a real physical phenomenon resulting from the nonlinear thinning dynamics when the mean initial disturbance wavenumber is smaller than $0.5k_c$, where k_c is the cut-off wavenumber (Joo et al., 1991) (see section 4.2.2). For these perturbations, the evolution of the film is highly unstable and at the moment of break-up, the energy does not remain confined to the fundamental mode of instability (λ_{md}), instead spreads to its harmonic modes (such as $2\lambda_{md}$ or $3\lambda_{md}$).

The trends discussed in Figures 4.4(a) and 4.4(b) are therefore, similar to those with $M = 0$ in Figure 4.2(a) and (b), as also seen in prior work (Kargupta et al., 2000; Zope et al., 2001). However, in contrast to Figure 4.2(c) and the results observed in prior studies (Kargupta et al., 2000; Zope et al., 2001), widening the hydrophobic patch to $w_h = 2.2\lambda_{md}$ causes the interface to rupture again at the center of the patch when $M = 100$ (Figure 4.4(c)). To recall, two independent ruptures occur at the edges of the hydrophobic patch for $M = 0$ when $w_h = 2.2\lambda_{md}$ with the trapping of a big droplet at the center (Figure 4.2(c)). These independent ruptures at the patch edges are present as near ruptures for $M = 100$, but with the hydrophobic patch being wide enough, strong Marangoni flows that compete with the wettability gradients drive liquid away from the center and cause rupture there (Figure 4.4(c)). This transition to an independent rupture at the center for wide patches is seen in our simulations only when the Marangoni parameter was increased to $\sim \mathrm{O}(10^2)$ times the Hamaker constant H_1.

Figure 4.5 shows the variation of the rescaled rupture time as function of the hydrophobic patch width w_h for $M = 0$, $M = 5$, and $M = 100$. Here we plot the ratio of the absolute rupture time T_r to the corresponding rupture time in the limit of a chemically homogeneous surface, T_{r0}. In our simulations, the absolute rupture time T_r is found to be $\sim 10^3$ times smaller for $M = 0$ than for the case $M = 100$, and therefore a plot comparing the rescaled rupture times is shown for convenience to

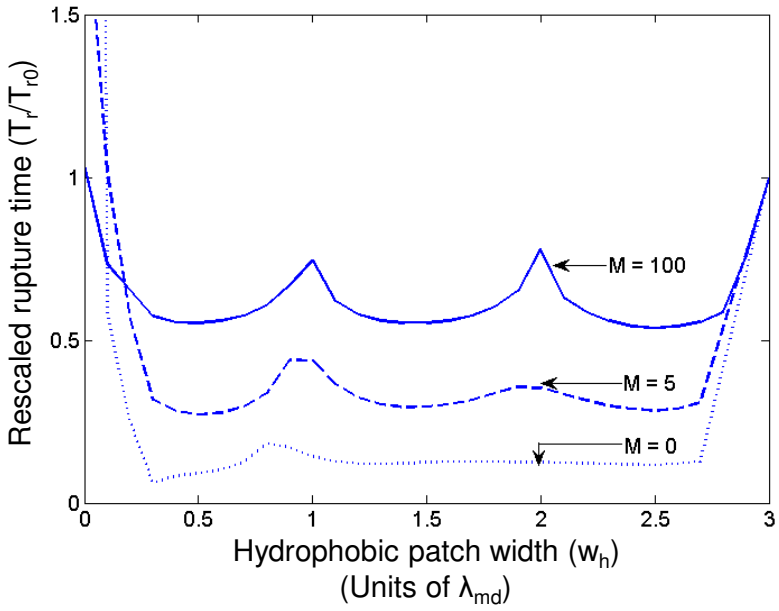

Figure 4.5: Rescaled rupture time as function of the hydrophobic patch width w_h for different values of M. Here, $\bar{C} = 1$, and $H_2 = 0$. The variation of $H_1(x)$ is represented by the function (4.17) (see section 4.2.3) with $H_1 \to 1$ at the central hydrophobic patch and $H_1 \to 0$ on the hydrophilic areas. For $w_h = 0$, the absolute rupture time values are $T_r \to \infty$, $T_r = 2.8$, and $T_r = 7$ x 10^{-3} for $M = 0$, $M = 5$, and $M = 100$ respectively.

the reader. In the limit $w_h \to 0$, which represents a uniformly hydrophilic substrate with $H_1 = 0$, the rupture time increases towards the corresponding asymptotic values for each of the cases $M = 0$, $M = 5$, and $M = 100$. These values are $T_r \to \infty$, $T_r = 2.8$, and $T_r = 7$ x 10^{-3} for $M = 0$, $M = 5$, and $M = 100$ respectively. In general, it is found that increasing the value of M decreases the absolute rupture time T_r, suggesting that uniform heating promotes the wettability-gradient-driven rupture. The cross-over between the curves for $M = 0$, $M = 5$, and $M = 100$ in figure 4.5 is due to the rescaling of the absolute rupture time T_r by T_{r0}.

As explained qualitatively by Zope et al. (2001) and later analyzed in detail by Lenz and Kumar (2007a) for two-layer systems, all three curves in Figure 4.5 show a global mimina corresponding to perfect cooperation between the wettability-driven flow and the wettability gradient-driven flow. This is followed by a local maxima (e.g., near $w_h = 0.7\lambda_{md}$ for $M = 0$ or near $w_h = 1.0\lambda_{md}$ for $M = 100$) where the opposition from capillary flows is the strongest. In contrast to the behavior for $M = 0$ and $M = 5$, instead of then plateauing to an asymptotic value, the curve for $M = 100$ shows another transition to a new local maxima near $w_h = 2\lambda_{md}$. As the patch is widened beyond the first local maxima, the previously flat region of the curve ($M = 0$ and $M = 5$) is now affected by stronger Marangoni forces that compete with the wettability gradients to trigger an independent rupture at the center. The new local maxima for $M = 100$ in Figure 4.5 arises when the opposition from capillary flows to this Marangoni-driven rupture is the strongest. The limit $w_h = 3\lambda_{md}$ represents a uniformly hydrophobic substrate for which the rupture time again asymptotically approaches the corresponding value for each Marangoni number M.

The results presented here therefore suggest cooling would prove to be a useful strategy for considerably delaying the rupture even in the presence of wettability gradients. Heating would not lead to significant changes in the rupture patterns, however, a sufficiently large hydrophobic patch can pave way for the Marangoni forces to trigger an independent rupture.

4.3.2 *Localized heating and cooling*

We now examine the instability behavior when M is varied spatially across the domain. Figure 4.6 shows two possible variations of $M(x)$ and $H_1(x)$ along the domain with $\bar{C} = 1$ and $H_2(x) = 0$. These variations are modeled using the analytical functions (4.17) and (4.18) defined in section 4.2.3. For the variation in figure 4.6(a) H_0 is set to 1 and M_0 is set to 100. This profile corresponds to intensive localized

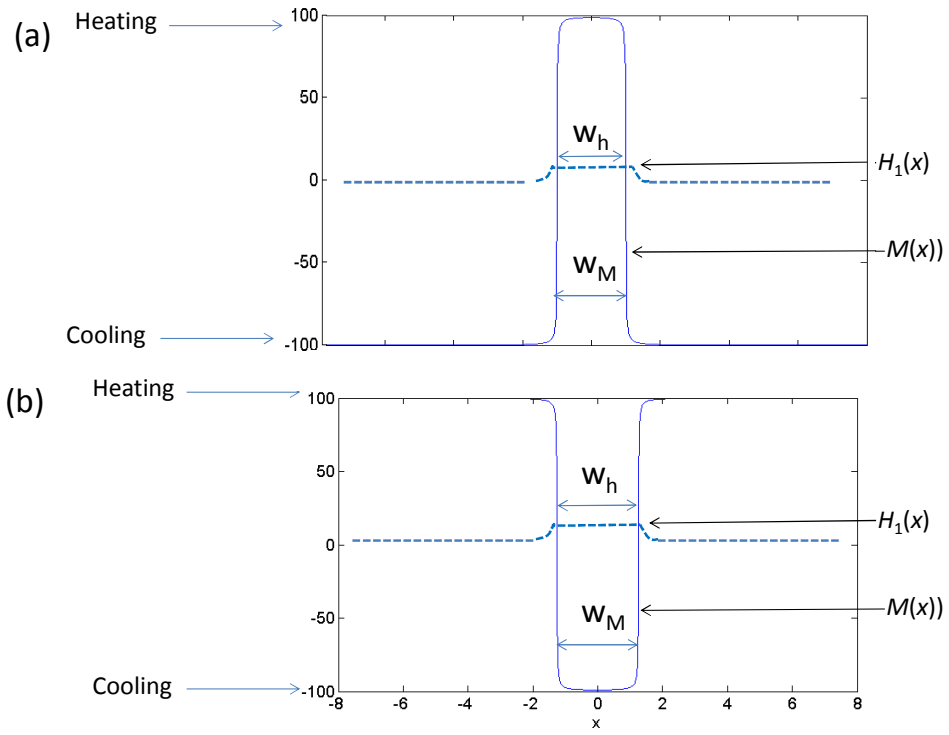

Figure 4.6: Typical spatial variations of $M(x)$ and $H_1(x)$ on a chemically patterned surface.

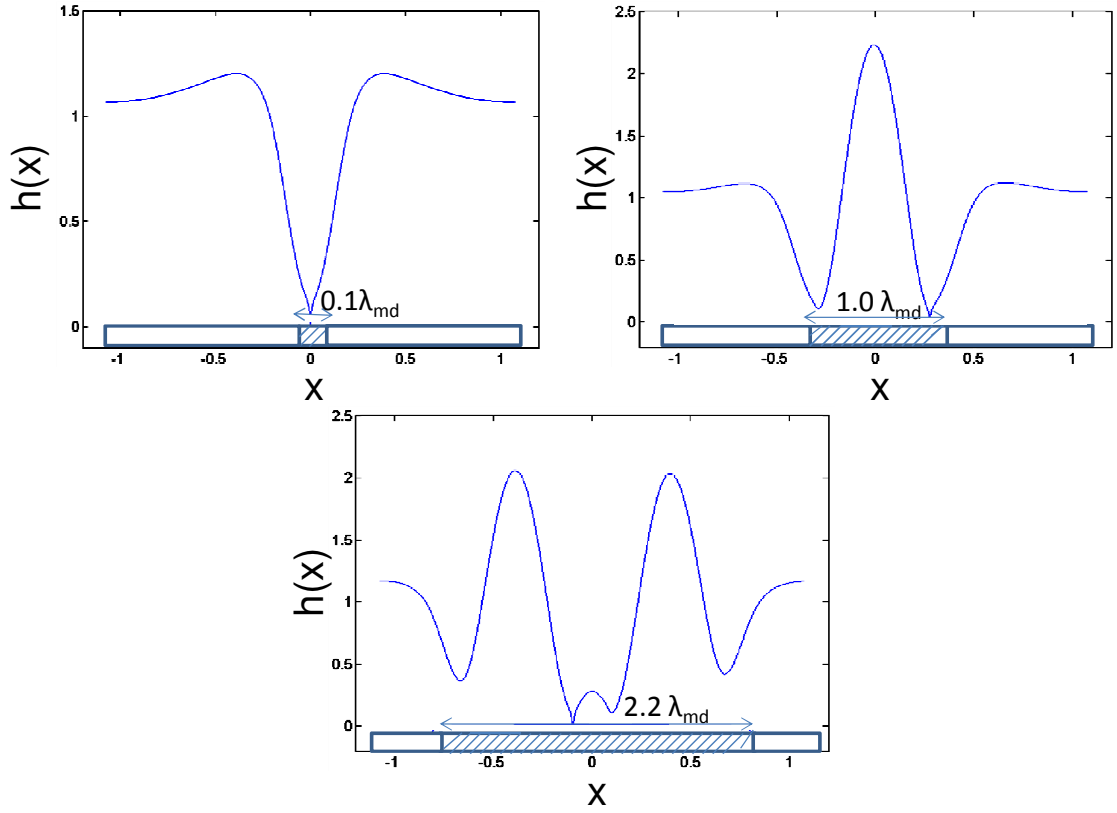

Figure 4.7: Interface profiles at rupture for three different hydrophobic patch widths. Here, $\bar{C} = 1, H_2 = 0$, $M(x)$ and $H_1(x)$ vary as in Figure 4.6(a), according to the analytical function defined in section 4.2.3.Further, we set $w_M = w_h$ in all cases.

heating from below at the central patch of width w_M along with localized cooling at the sides. The variations of $M(x)$ and $H_1(x)$ may ofcourse be suitably modified so that the widths w_h and w_M may be varied relative to each other. As opposed to the setting in Figure 4.6(a), we may also set $M_0 = -100$ in (4.18), so that a patch of width w_M at the center of the domain would be locally cooled, and the other regions would be heated. The resulting profile for $M(x)$ is depicted in Figure 4.6(b). Here $H_1(x)$ varies in the same manner as earlier, with the variation being described by the analytical function (4.17) in section 4.2.3 with $H_0 = 1$.

For the spatial variation described in Figure 4.6(a), Figure 4.7 shows interface profiles at rupture obtained for $w_h = 0.1\lambda_{md}$, $1.0\lambda_{md}$, and $2.2\lambda_{md}$ on a simulation domain of $3\lambda_{md}$ with $\bar{C} = 1$, $H_2(x) = 0$, and $w_M = w_h$ in all cases. Qualitative features similar to Figure 4.4 are observed with rupture occuring at the center for the smallest hydrophobic patch (hatched areas), followed by frustrated off-center ruptures with high interfacial curvatures at the center, and finally the transition back to rupture

at the center of the domain for wide-enough patches. Consistent with predictions from the linear theory (section 4.2.2) the thermocapillary stresses reinforce the rupture driven by the wettability gradients and the wettability forces at the center where $M = 100$. Consequently, the rupture is accelerated relative to the case $M = 0$, though the qualitative behavior of the rupture time with the patch width is similar to that in Figure 4.5. However, the allied local cooling effects at the hydrophilic ends almost leads to leveling of the film as opposed to the wavy interface patterns observed in Figure 4.4.

The width of the heated zone w_M was varied relative to the hydrophobic patch width w_h to further probe the competition between Marangoni flows and the wettability-gradient-driven rupture. The limit $w_M \to 0$ represents the case of uniform cooling with $M = -100$ throughout the domain (section 4.3.1), while $w_m \to 3\lambda_{md}$ represents the case of uniform heating, with $M = 100$ everywhere. However, when the widths w_M was varied relative to w_h, we essentially observed the same qualitative behavior of the interface evolution. This suggests that the primary mechanism driving the rupture is the wettability gradients, while the Marangoni forces only assist the rupture thus induced. Several runs with different w_h showed that there is little variation in the rupture time behavior with variations in w_M, except for a sharp transition as $w_M \to 0$ to the rupture time in the no-Marangoni limit.

The temperature profile is now reversed as in Figure 4.6(b), with $M = -100$ (corresponding to cooling) at the hydrophobic center of width w_M and $M = 100$ (corresponding to heating) at the hydrophilic ends. Figure 4.8 shows interface profiles at rupture for increasing hydrophobic patch widths ($0.1\lambda_{md}$, $1.0\lambda_{md}$, and $2.2\lambda_{md}$) where we set $w_M = w_h$. For comparison, the reader is referred to Figure 4.2 to review the corresponding plots with $M = 0$ uniformly throughout the domain. In addition, Figure 4.9 shows for comparison, the interface profiles at rupture with the same spatial variation as in Figure 4.6(b), but with the maximum and minimum values of M being 1 and -1 respectively. Figure 4.8 shows that for all the hydrophobic patch widths, the rupture pattern is reversed in comparison with Figure 4.2, with rupture driven by the high degree of heating now occuring at the hydrophilic ends, while the cooling effect at the center fights the wettability-driven flows and forces a big mound of liquid at the center. The templating as seen in Figure 4.8 is not perfect, with some spill-over of the liquid onto the hydrophilic areas. Notably, the rupture occuring in Figure 4.8 is entirely induced by Marangoni forces, as attractive van der Waals forces are assumed to be absent at the hydrophilic areas ($H_1 \to 0$ by use of the analytical function (4.17) in section 4.2.3). However, these results suggest tremendous practical

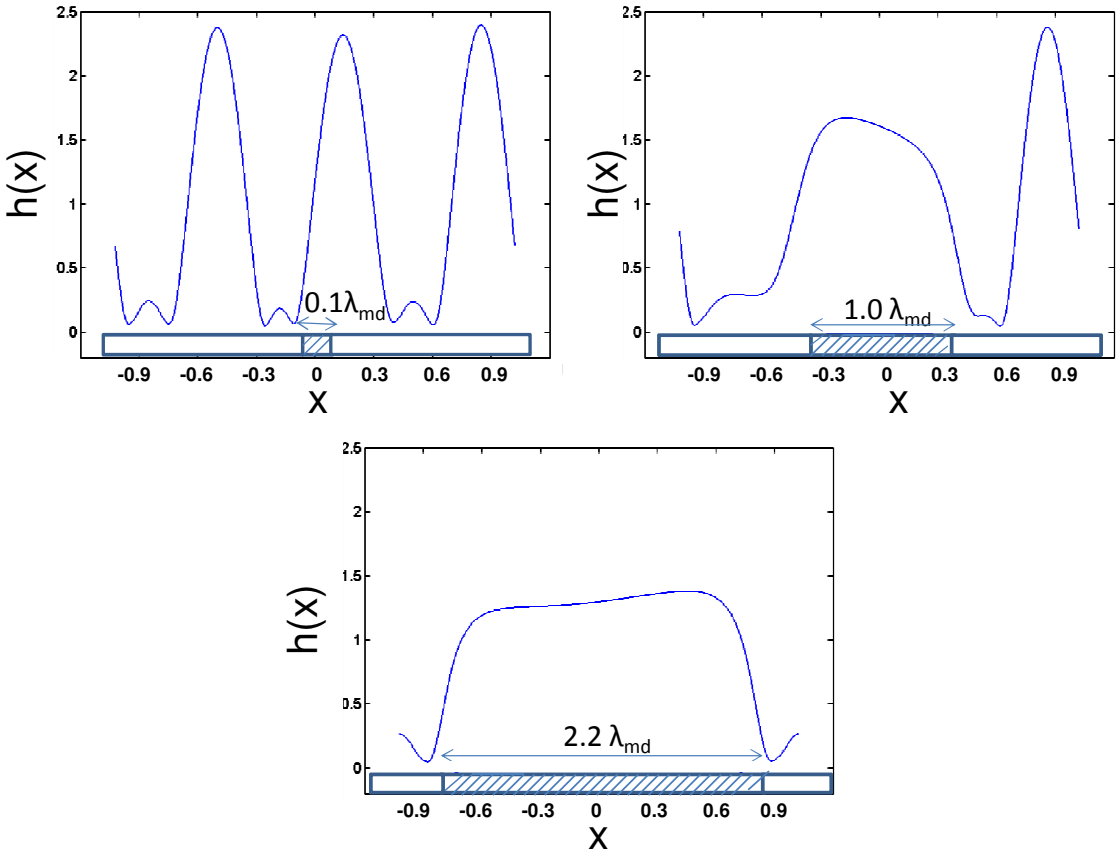

Figure 4.8: Interface profiles at rupture for three different hydrophobic patch widths. Here, $\bar{C} = 1$, $H_2 = 0$, $M(x)$ and $H_1(x)$ varies as in Figure 4.6(b), i.e., $M(x) = -100$ on the hydrophobic patches (hatched areas), and $M(x) = 100$ on the hydrophilic patches (unhatched areas). Further, we set $w_M = w_h$ in all cases.

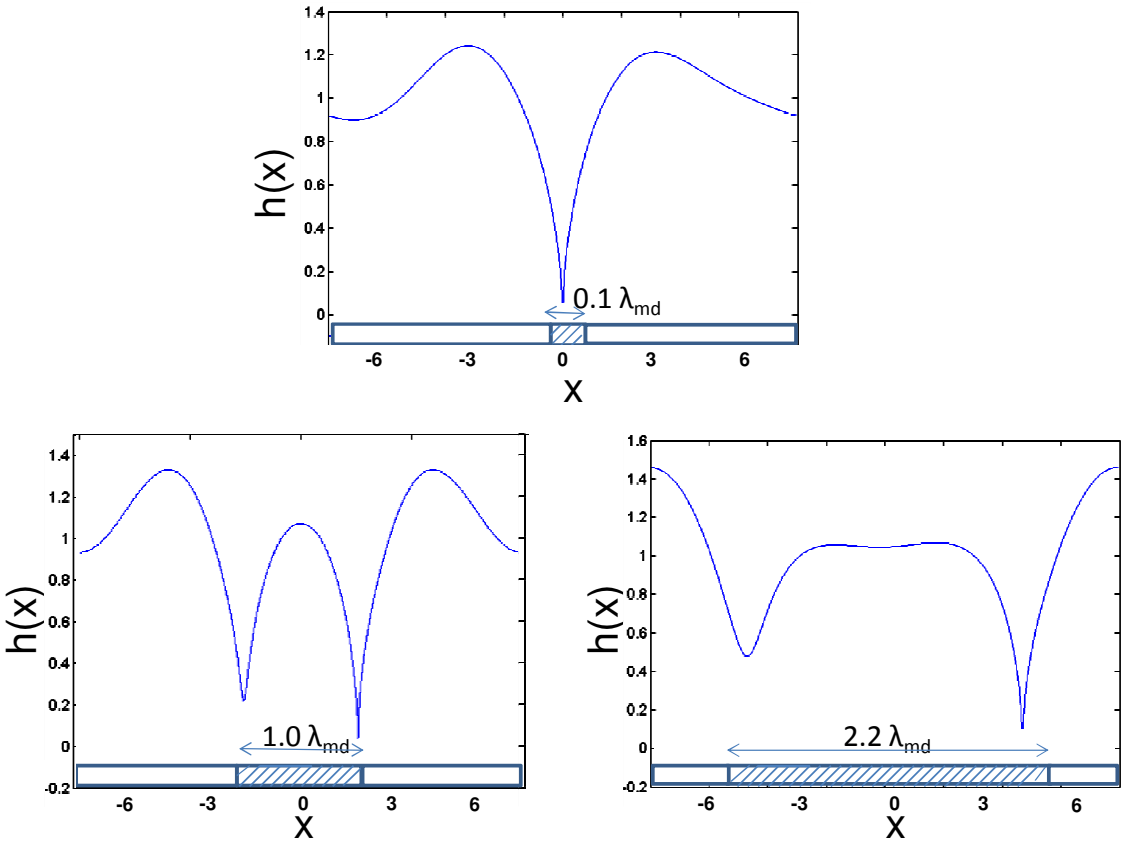

Figure 4.9: Interface profiles at rupture for three different hydrophobic patch widths. Here, $\bar{C} = 1$, $H_2 = 0$, $H_1(x)$ and $M(x)$ vary as in Figure 4.6, with $H_0 = 1$ and $M_0 = -1$. Further, we set $w_M = w_h$ in all cases.

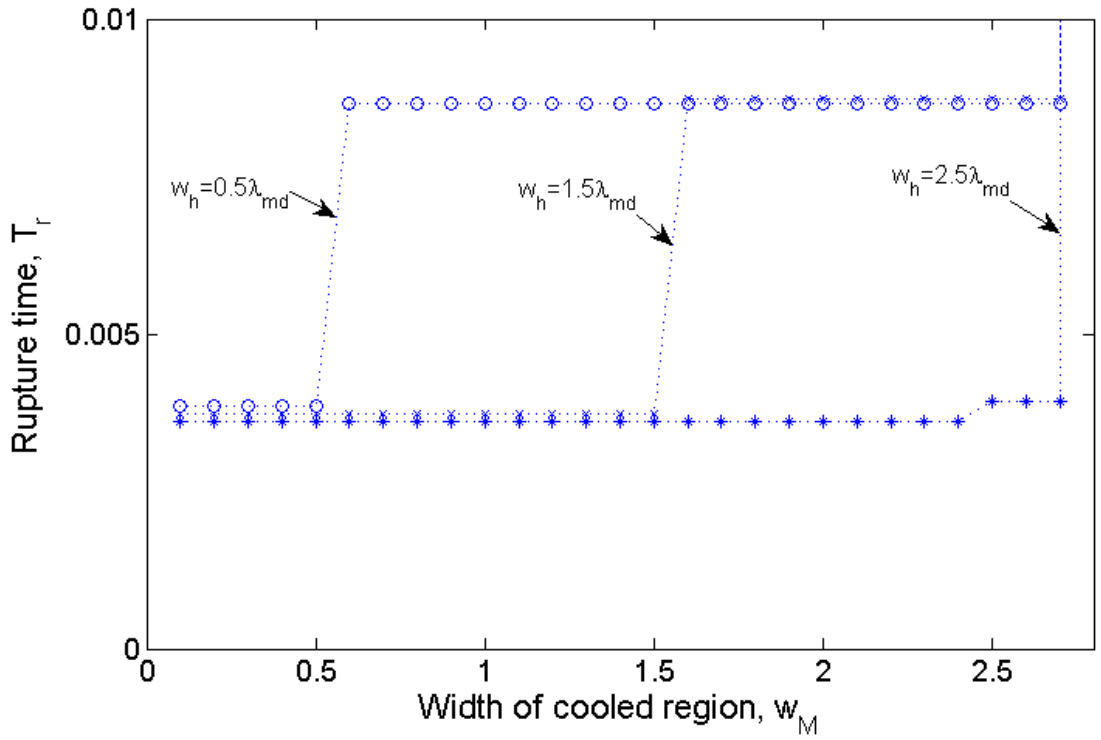

Figure 4.10: Variation of rupture time as a function of the width w_M of the cooled region of the domain for different hydrophobic patch widths w_h. Here $C = 1$, $H_2 = 0$, and $H_1(x)$ and $M(x)$ vary according to the analytical functions described in section 4.2.3, with $H_0 = 1$ and $M_0 = -100$.

significance of thermocapillary-induced dewetting on chemically patterned substrates from the viewpoint of physical applications. Given a substrate whose wettability is hard to control, the thermocapillary effects provide a handle for achieving wetting at a desired region, while forcing the formation of a big mound of liquid at the other areas. The desired result may be achieved by local heating of the zone where wetting is desired, and cooling the adjoining zones to suppress the wettability-induced rupture.

The modified rupture behavior seen in Figure 4.8 is not observed in Figure 4.9 when the degree of heating and cooling is reduced (M varying between -1 and 1). Our results here and in section 4.3.1 therefore suggest that intensive cooling or heating is required to fight the van der Waals forces and manipulate the rupture dynamics. Depending on the physical properties of the liquid and the exact temperature differences used, such heating or cooling could lead to the risk of evaporation or freezing of the liquid, or a change in its viscosity. These details are probed further in section 4.3.4 where we discuss our findings with a realistic parameter set.

The above results were analyzed to determine the dominant instability mecha-

nism by varying the Marangoni length scale w_M relative to w_h, the length scale of the wettability pattern. For a simulation domain of $3\lambda_{md}$, Figure 4.10 shows the variation of rupture time as function of the width w_M of the cooled region for different hydrophobic patch widths w_h. Since the cooling effect at the center fights the wettability-driven rupture at the center, the rupture time behaves differently unlike the monotonous behavior for the case in Figure 4.6(a) discussed above. In each case, the rupture is delayed when the width of the cooled region w_M exceeds the hydrophobic patch width w_h, and as w_M approaches the total length of the domain, a major increase in the rupture time occurs. The film would however, eventually rupture due to the wettability-gradient-driven flow. For a given hydrophobic width w_h, the interface profiles in the entire regime $w_M > w_h$ assume the shapes depicted in Figure 4.8, until the sharp rise in rupture time occurs for the limit of uniform cooling at $w_M = 3\lambda_{md}$. Likewise, within the regime $w_M < w_h$, the interface profiles in Figure 4.8 undergo transition to profiles in Figure 4.4. These results corroborate the observation that the wettability gradients are instrumental in causing the rupture, while the Marangoni forces only assist the rupture thus induced.

Apart from the competitions between the Marangoni flows and the wettability gradients in the dewetting process, the spatial variation in Figure 4.6 also contributes to high gradients in M at the edges of the hydrophobic patch. The significance of the gradients in M in the process of competitive dewetting was examined by using the same spatial variations with lower maximum and minimum values of M, but narrowing the transition width (see section 4.2.3) to maintain high gradients in M. As an example, simulations were conducted with $M_0 = 1$ and $\delta = 5$ x 10^{-5} in the analytical function (4.18) (section 4.2.3). For these values, $M(x) \to -1$ at the central hydrophobic patch, steeply increasing to $M(x) \to 1$ at the hydrophilic areas over a transition width 200 times smaller than that used for the simulation results in Figure 4.8. However, the reversal of rupture as seen in Figure 4.8 was not observed and the resulting interface profiles resembled those in Figure 4.9. Our simulations therefore suggest that the gradients in M do not play a significant role, instead it is the absolute degree of heating or cooling that competes with the wettability gradient-driven flow.

The reversal of rupture dynamics in Figure 4.8 suggests that there exists a critical Marangoni number below which the cooling effect confronts with the wettability-driven flows and the wettability gradients to cause leveling of the interface. The governing equation (4.13) provides an estimate for this critical Marangoni number for

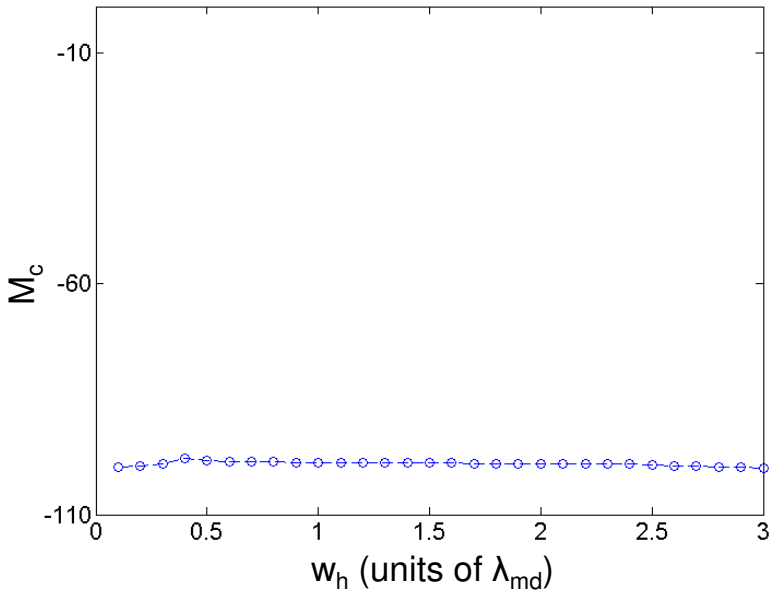

Figure 4.11: Critical Marangoni number as function of the hydrophobic patch width w_h for localized cooling at the center with with $\bar{C} = 1$, $h_0 = 1$, and $H_2(x) = 0$. Here $H_1(x)$ is modeled by the function (4.17) (section 4.2.3) with $H_0 = 1$. Further we set $w_M = w_h$.

a given value of H_1:

$$\partial_x(\frac{Mh^2}{2}\partial_x h + \frac{H_1}{h}\partial_x h - \frac{1}{3}\partial_x H_1) = 0 \Rightarrow M_c \sim -\frac{2H_1}{h^3} + f(w_h, h, H_1), \qquad (4.19)$$

where M_c is the critical Marangoni number and w_h is the width of the hydrophobic patch, so that $f(w_h, h, H_1)$ would be determined by the function which models the spatial variation of $H_1(x)$ (see section 4.2.3). Figure 4.11 shows the variation of M_c with w_h for a chosen variation of $H_1(x)$ and $M(x)$ as in (4.17) and (4.18) (see section 4.2.3) with $H_0 = 50$, while $h_0 = 1$, $H_2 = 0$, and $\bar{C} = 1$. The choice $H_0 = 50$ is used as it would facilitate the computations by allowing the use of a smaller simulation domain by decreasing the value of λ_{md} (see section 4.2.1). In all these calculations, w_h is chosen to be equal to w_M. The critical Marangoni number M_c was determined as the largest value for which the minimum interfacial height is always greater than $0.99h_0$ until $t = T_r'$ x 10^3 was reached, where T_r' is the rupture time in the absence of any Marangoni effects (i.e, $M = 0$). For the chosen set of parameters, Figure 4.11 shows that $M_c \sim -2H_1$ with minor variations for each given hydrophobic patch width. The exact profile, as suggested by the analytical expression (4.19), would vary with different heating and cooling profiles, and the profile for $H_1(x)$.

Although the results in Figure 4.8 suggest that localized heating and cooling may be used to compensate for the instability induced by intermolecular forces, investigations by Yeo et al. (2003) reveal that localized Marangoni effects can engender an instability in the transverse direction in a two-dimensional (2-D) domain. Given that surface tension in a 2-D geometry can have a destabilizing effect due to the transverse curvature, a potential spanwise instability in presence of localized heating/cooling effects can lead to the disintegration of droplets into small threads on the hydrophilic stripes (as in the Rayleigh instability of circular cylinders (Rayleigh, 1878)). Prior studies on wetting of chemically patterned surfaces (Darhuber et al., 2000; Lipowsky et al., 2000; .Speth and Lauga, 2009) suggest that such capillary instabilities occur when the contact angle formed by the deposited liquid volume on the heterogeneous stripe exceeds its natural contact angle with the liquid. Variation of liquid volume by controlling the film thickness and the heterogeneous patch widths would then provide a potential strategy for creating ordered arrays of liquid droplets or dispersed colloidal particles (Guo et al., 2001; Luo et al., 2004; Park et al., 2006). Such methods would prove valuable in the manufacture of various microelectronic and optical devices.

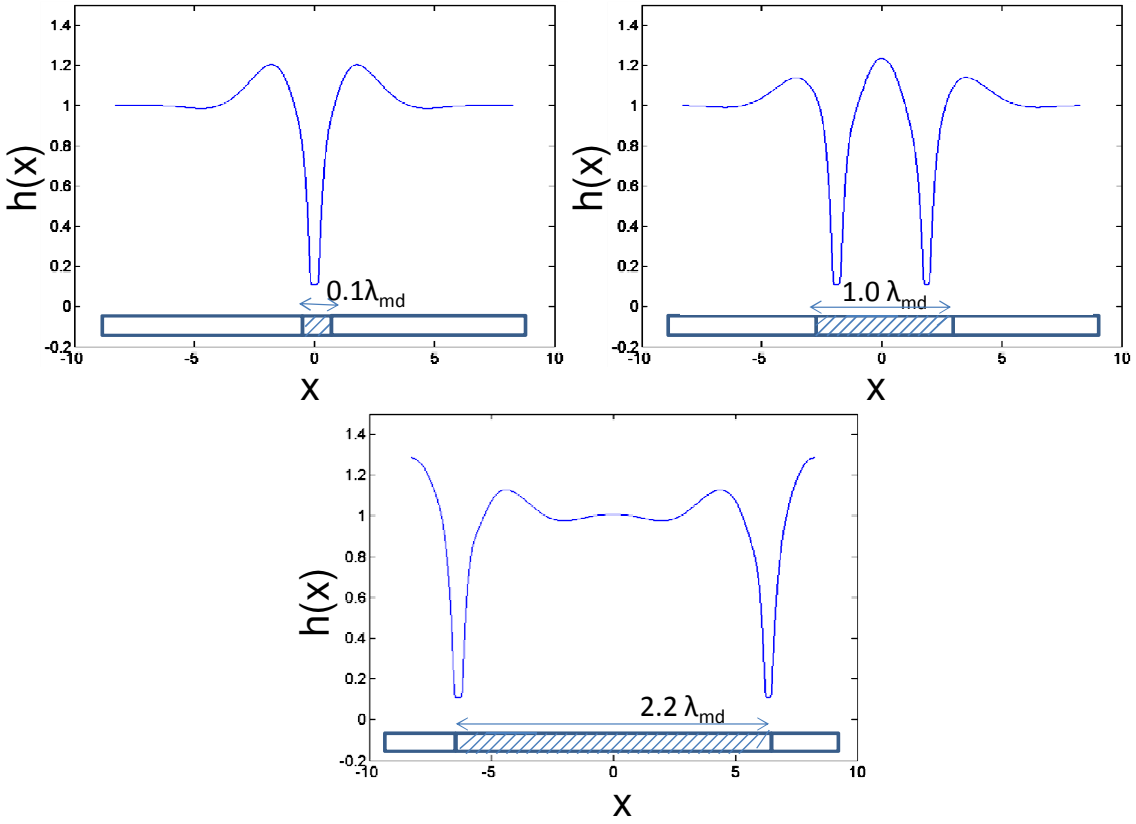

Figure 4.12: Interfacial profiles resulting from the dewetting of a film when $M = 0$ and $\bar{C} = 1$. Here $H_1(x)$ and $H_2(x)$ are modeled by the function (4.17) (section 4.2.3) with their maximum values being 1 and 0.1 respectively. Further, we set $w_h = w_M$ in all cases.

4.3.3 *Effects of repulsive intermolecular forces*

So far we have considered the case $H_2 = 0$ in sections 4.3.1 and 4.3.2. We now turn to the case $H_2 > 0$ so that repulsive intermolecular forces are operative in preventing a complete interfacial rupture, instead allowing the film to attain an equilibrium film thickness (see section 4.2.1). Figure 4.12 shows typical interfacial profiles resulting from the dewetting of a film when $M = 0$, $\bar{C} = 1$, $H_1(x)$ and $H_2(x)$ varying as in (4.17) (section 4.2.3) with $H_0 = 1$, so that $H_1(x) \to 0$ and $H_2(x) \to 0$ on the hydrophilic areas. In each case, it is observed that the qualitative features of the interface profile are similar to the case $H_2 = 0$ as seen in Figure 4.2, with the difference that the film has not ruptured, instead has thinned down to an equilibrium thickness. For larger hydrophobic patch widths, this results in the trapping of a big drop of liquid in the center.

Figure 4.13 shows interface profiles at $t = 1.0$ x 10^{-3} for three different hydropho-

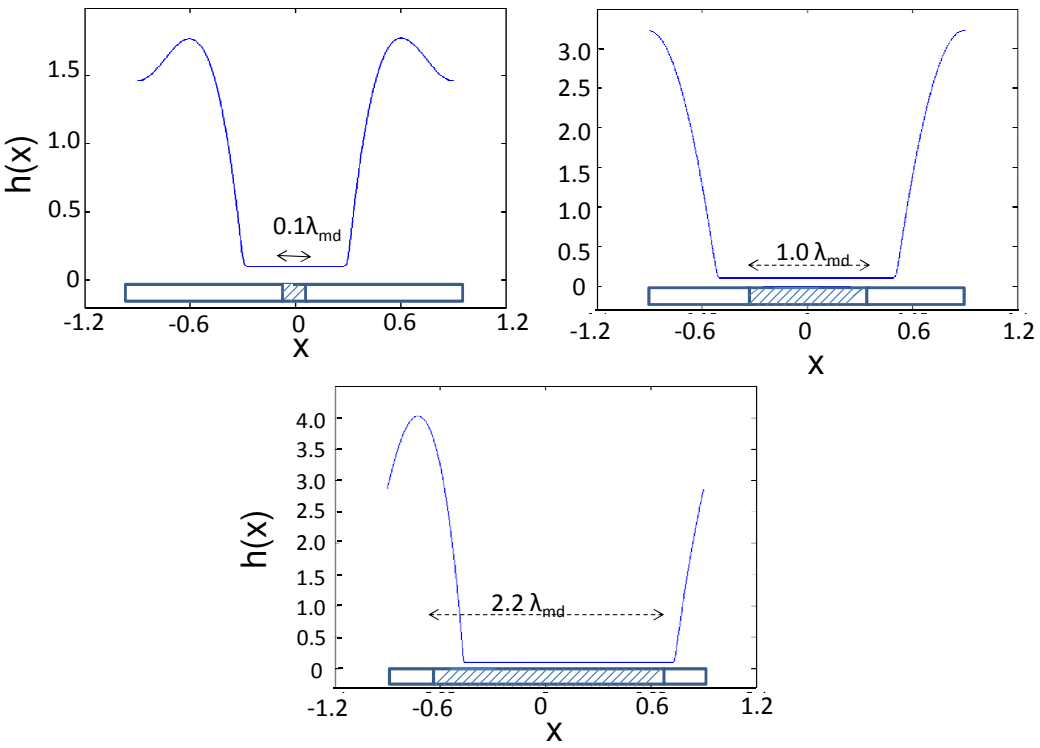

Figure 4.13: Interface profiles at $t = 1.0$ x 10^{-3} for a dewetted film with $M(x) = 1$ throughout the domain and $\bar{C} = 1$. Here $H_1(x)$ and $H_2(x)$ are modeled by the function (4.17) (section 4.2.3) with their maximum values being 1 and 0.1 respectively. Further, we set $w_h = w_M$ in all cases.

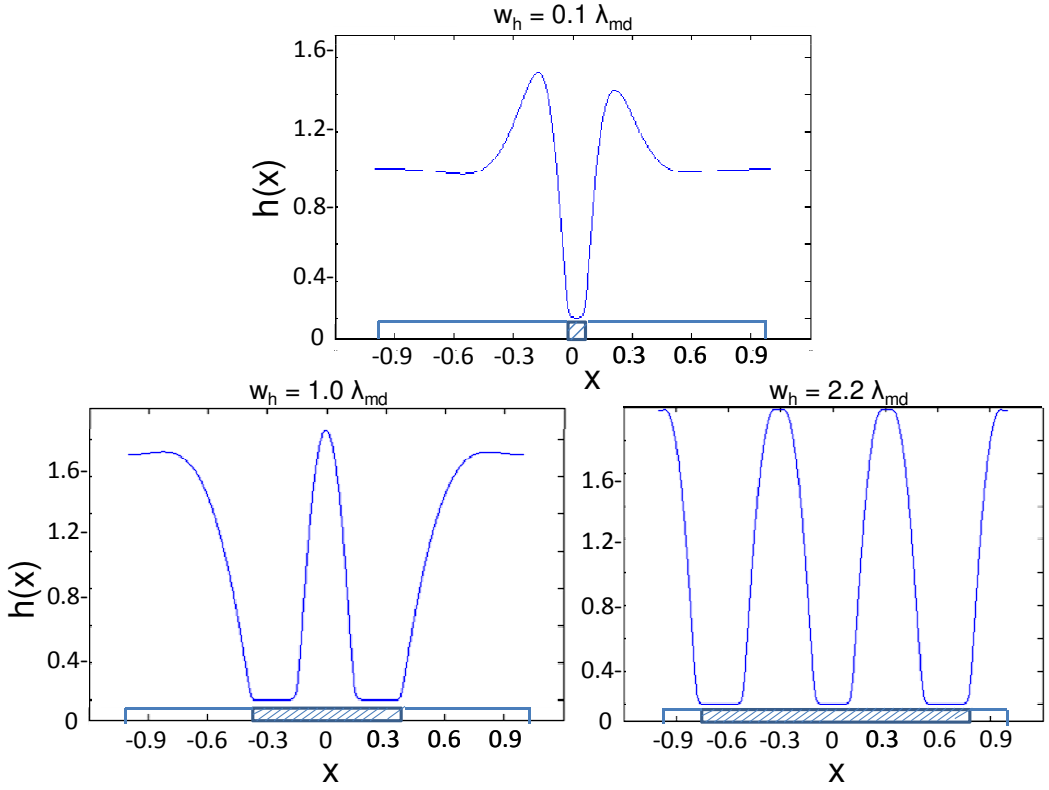

Figure 4.14: Interface profiles at t = 1.0 x 10^{-3} for a dewetted film with $\bar{C} = 1$. Here $H_1(x)$ and $H_2(x)$ are modeled by the function (4.17) (section 4.2.3) with their maximum values being 1 and 0.1 respectively. The parameter $M(x)$ is modeled using function (4.18) (section 4.2.3) with $M_0 = 100$, and $w_h = w_M$ in all cases.

bic patch widths ($w_h = 0.1\lambda_{md}$, $1.0\lambda_{md}$, and $2.2\lambda_{md}$) when the bottom surface is uniformly heated, with $M = 100$ throughout the domain. With $H_2(x)$ being non-zero, these plots reveal the post-rupture behavior of the liquid film for which the interface profiles at rupture (Figure 4.4) was analysed in section 4.3.1. Here $\bar{C} = 1$ while $H_1(x)$ and $H_2(x)$ varies as in the function (4.17) (section 4.2.3), with the maximum values of $H_1(x)$ and $H_2(x)$ being 1 and 0.1 respectively. In contrast to Figure 4.12, the width of the equilibrium film formed extends beyond the width of the hydrophobic patch in each case, destroying the near-perfect templated structure. With the domain being uniformly heated, the near rupture of the film seen at the hydrophilic areas (unhatched areas) is attributed to the Marangoni flows that drive liquid from the hydrophobic zones. Therefore, although heating may accelerate the dewetting process, it destroys the intended templating. The templating may be preserved, instead by localized cooling at the hydrophilic areas, as suggested by the profiles in Figure 4.14. In these plots, $M(x)$ varies as in the function (4.18) (section 4.2.3) with $M_0 = 100$, so that $M(x) \to 100$ on the hydrophobic areas (hatched) and $M(x) \to -100$ on the hydrophilic areas (unhatched). Here $\bar{C}$, $H_1(x)$, and $H_2(x)$ are set to be the same as in Figure 4.13. As the hydrophilic areas are now cooled, the Marangoni forces therefore prevent the liquid from being driven to the hydrophilic areas. Therefore, the qualitative features displayed in these plots resemble those in Figure 4.12 with $M = 0$, with near-ruptures occuring only on the hydrophobic areas.

A combination of localized cooling at the center and localized heating at the sides on the other hand induces the reversal of rupture dynamics as observed even for $H_2 = 0$ (figure 4.8). Figure 4.15 shows interface profiles at rupture for such localized cooling and heating conditions, with $M(x)$, $H_1(x)$, and $H_2(x)$ varying as in the analytical functions defined in section 4.2.3. The maximum values of H_1 and H_2 are 1 and 0.1 respectively, so that $H_2(x) \to 1$ and $H_1(x) \to 1$ at the hydrophobic areas, while $H_1(x) \to 0$ and $H_2(x) \to 0$ at the hydrophilic areas. The value of M_0 is set to -100 and $\bar{C} = 1$. Since intensive heating is present at the hydrophilic areas, the film ruptures there even before the intermolecular forces can kick in at the center. Keeping other values the same, if $H_2(x)$ is uniformly set to 0.1 throughout the domain so that a complete rupture can be prevented, the liquid film thins down to an equilibrium film on the hydrophilic areas. Interface profiles illustrating such behavior is shown in Figure 4.16 for different hydrophobic patch widths. Thus the reversal of rupture dynamics as observed in Figure 4.8 is also seen here.

As the repulsive intermolecular forces result in the formation of a flat film on the hydrophobic patch of width w_h, the final steady state interfacial profile of the

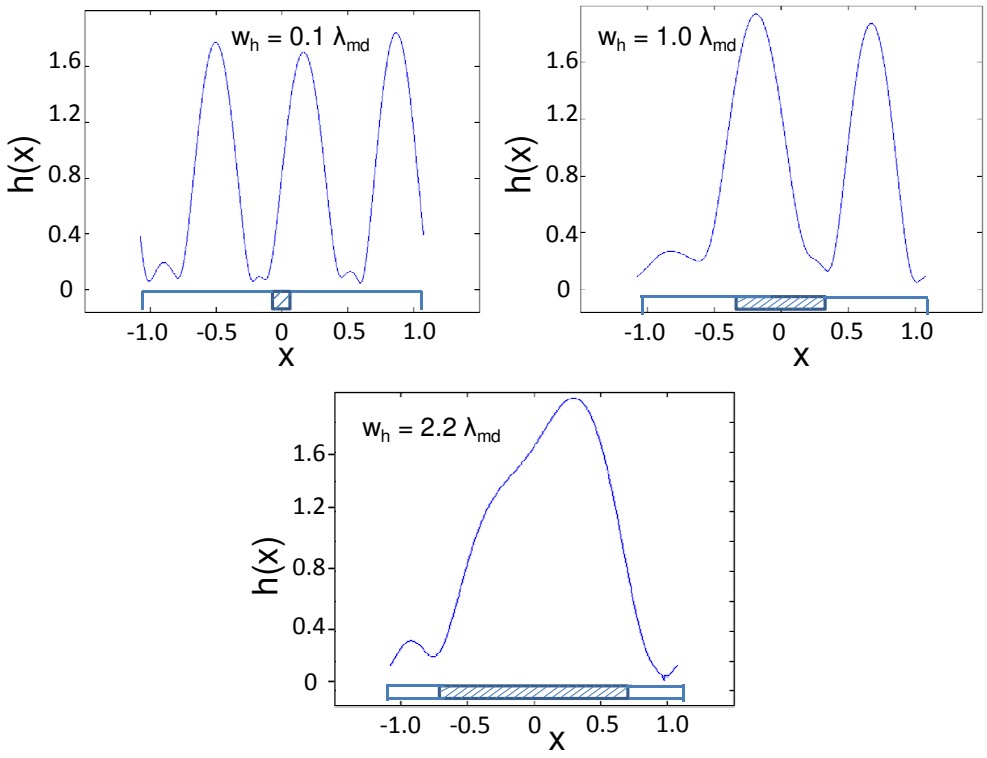

Figure 4.15: Interface profiles at rupture for a dewetted film with $\bar{C} = 1$. The paremeters $H_1(x)$, $H_2(x)$ and $M(x)$ vary as in the functions in section 4.2.3. The maximum values of H_1 and H_2 are 1 and 0.1 respectively, while $M_0 = -100$, and $w_h = w_M$ in all cases.

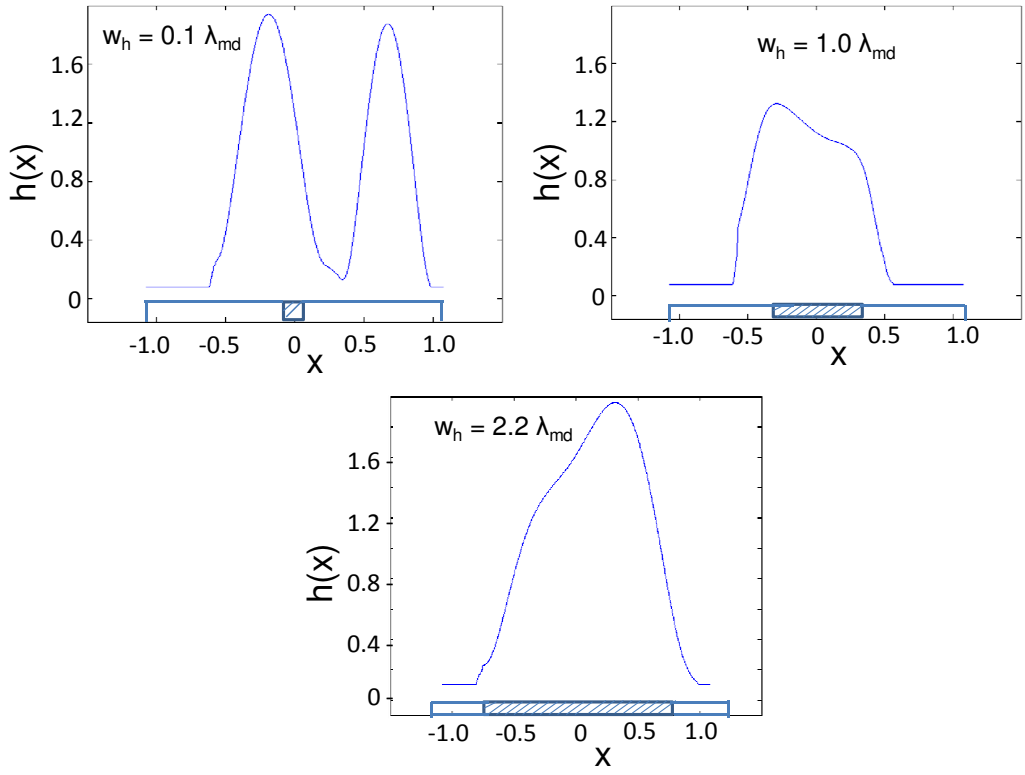

Figure 4.16: Interface profiles at rupture for a dewetted film with $\bar{C} = 1$. We set $H_2(x) = 0.1$ uniformly throughout the domain, while $H_1(x)$ and $M(x)$ vary as in the functions in section 4.2.3 with $H_0 = 1$, $M_0 = -100$, and $w_h = w_M$ in all cases.

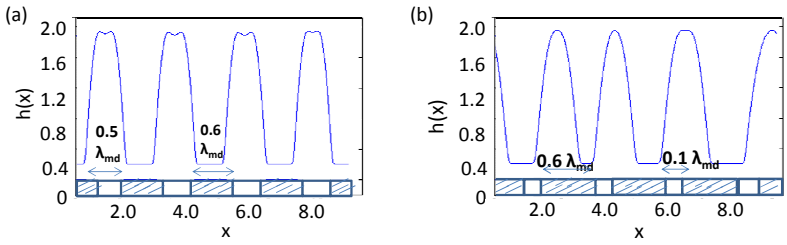

Figure 4.17: (a) Steady state interface profile for a dewetted film with several hydrophobic patches packed in the domain, each separated by a hydrophilic patch of width $0.5\lambda_{md}$. Here $\bar{C} = 1$. Governed by the functions in section 4.2.3, $H_1(x) \to 1$ and $M(x) \to 1$ on the hydrophobic patches (hatched) of width $w_h = 0.6\lambda_{md}$. Here $w_M = w_h$ and $H_1(x) \to 0$ and $M(x) \to 0$ elsewhere in the domain. We also model $H_2(x)$ by the function (4.17) in section 4.2.3 with $H_0 = 0.1$. (b) The same figure as in (a), but with a hydrophilic patch width of $0.1\lambda_{md}$.

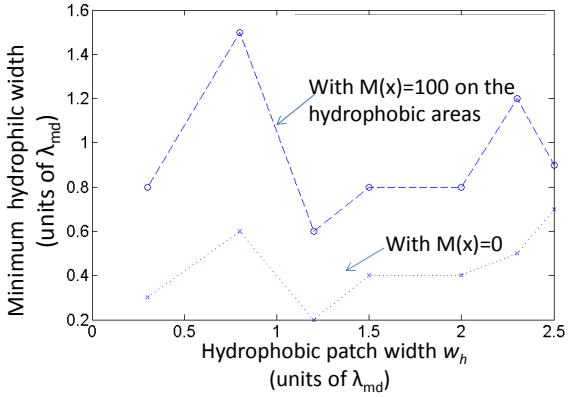

Figure 4.18: Critical hydrophobic patch width required to avoid the "spill-over" effect in the presence and absence of thermocapillary effects. These results were obtained using $\bar{C} = 0.05$. Here $H_1(x)$ and $H_2(x)$ are modeled by the function (4.17) (section 4.2.3) with their maximum values being 1 and 0.1 respectively. The parameter $M(x)$ was also modeled similar to $H_1(x)$ and $H_2(x)$, with the maximum value of $M(x)$ being 100 at the hydrophobic center and $M(x) \to 0$ at the hydrophilic areas of the domain.

film would be a configuration with minimum free energy for different patch widths w_h. This thermodynamic consideration would lead to more complex film dynamics when multiple hydrophobic patches of small widths are packed in a domain separated by a hydrophilic patch of given width (e.g., Figure 4.17). This would require large volumes of the liquid to necessarily collect at the hydrophilic areas (unhatched areas in Figure 4.17) and form structures with high interfacial curvatures (see Figure 4.17(a)). For a hydrophobic spacing of width $0.5\lambda_{md}$, Figure 4.17(a) shows that the formation of the equilibrium film has occured on all the hydrophobic patches (hatched areas) of width w_h, leading to near-perfect templating. However, as the width of the adjacent hydrophilic patch is reduced to $0.1\lambda_{md}$, Figure 4.17(b) shows that the equilibrium film starts to "spill-over" to a portion of the hydrophilic areas, destroying the near-perfect templating. Although a similar "spill-over" effect was observed in Figure 4.13, we point out that the cause of spill-over seen in Figure 4.17(b) is rather different, as $M(x)$ is set to 0 at the hydrophilic areas here. Similar anomalies in achieving perfect templating have been reported in previous studies on the effect of substrate periodicity single-layer flows on chemically patterned surfaces (Kargupta and Sharma, 2002c). We have also later extended their work to two-layer flows that will be reported elsewhere (Kalpathy et al., 2012).

Our current investigations show that the "spill-over" effect occurs when the hydrophilic patches (unhatched areas in Figure 4.17) separating each hydrophobic patch of width w_h (hatched areas in Figure 4.17) is smaller than a critical size. Figure 4.18

maps this critical hydrophilic patch width for different hydrophobic patch widths w_h in the presence of Marangoni effects and in their absence. The lower curve is obtained using the parameter set $\bar{C} = 0.05$, $M(x) = 0$ in the entire domain, and $H_1(x) = 10$ and $H_2(x) = 0.1$ along the hydrophobic patches, whereas $H_1(x)$ and $H_2(x)$ are modeled by the function (4.17) in section 4.2.3 with their maximum values being 10 and 0.1 respectively. In the upper curve where the effects of Marangoni forces are probed, we set $w_M = w_h$. In all cases, $\bar{C} = 0.05$, and $M(x)$ varies similar to that of $H_1(x)$ and $H_2(x)$ by the function (4.17) (section 4.2.3), with its maximum and minimum values being 100 and 0. The result shows that larger hydrophilic spaces are necessary to avoid the "spill-over" effect in the presence of thermocapillary effects as the strong Marangoni flows tend to promote the removal of large amounts of liquid from the hydrophobic patches, leading to increase in the interfacial curvatures on the hydrophilic areas.

Figure 4.18 allows us to extract a general heuristic to conveniently estimate the minimum width of the hydrophilic spacing for a given hydrophobic patch in terms of the most dangerous wavelength λ_{md} (see section 4.2.2). In the absence of any thermocapillary effects, one would require a hydrophilic spacing in the range $0.2\lambda_{md} - 0.6\lambda_{md}$ to avoid the spill-over of the equilibrium film and maintain near-perfect templating. However, when intensive localized heating is involved, the hydrophilic spacing needs to be increased to $\sim 0.8\lambda_{md} - 1.5\lambda_{md}$.

4.3.4 *Simulations with realistic parameter values*

As discussed in section 4.2.1, the parameters used in the present study have been rescaled from a physically realistic range for computational convenience. To substantiate our findings, we discuss the results obtained from a limited set of runs with a realistic set of values. In particular, we verify the reversal of rupture profiles observed in Figure 4.8 when intensive localized heating and cooling is present. As a typical parameter set, we choose M to be varying between -4 x 10^{-2} on a hydrophobic patch to 4 x 10^{-2} on the hydrophilic areas with the spatial variation similar to Figure 4.6. Further we set $H_1 = 3.5$ x 10^{-4}, $H_2 = 0$, and $C = 0.01$. Figure 4.19 shows the interface profiles at rupture obtained using these values for three different hydrophobic patch sizes (hatched areas). The resulting structures resemble those in Figure 4.8 with the film rupture occuring on the hydrophilic areas of the domain (unhatched areas) for all the three hydrophobic patch widths. Comparison with Figure 4.2 for the case $M = 0$ reflects that the competition from Marangoni forces can indeed reverse the

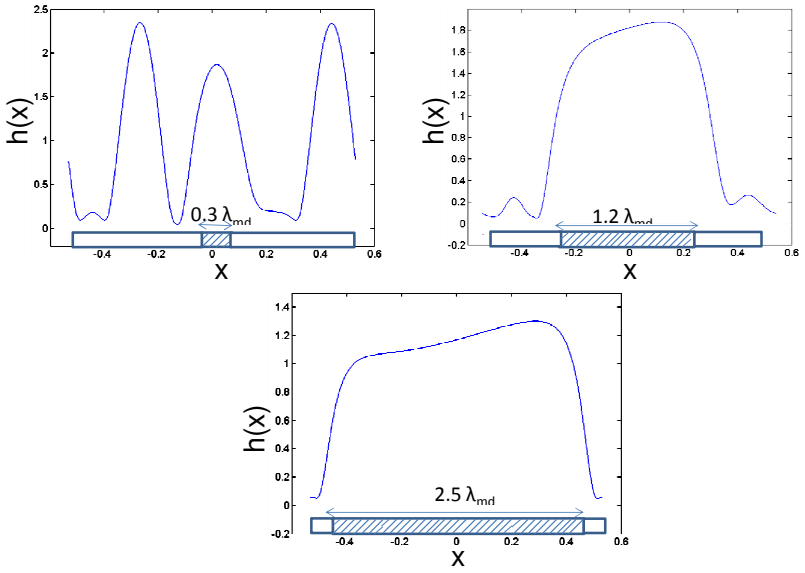

Figure 4.19: Interface profiles at rupture for hydrophobic patch widths of $0.3\lambda_{md}$, $1.2\lambda_{md}$, and $2.5\lambda_{md}$. In each case, $H_1(x)$ and $M(x)$ were modeled using the functions (4.17) and (4.18) (section 4.2.3), where we set $H_0 = 3.5 \text{ x } 10^{-4}$ and $M_0 = \text{-}4.0 \text{ x } 10^{-2}$. Further $h_0 = 1$, $H_2 = 0$, $w_h = w_M$, and $C = 0.01$.

pattern obtained from wettability-gradient-driven-rupture. This suggests the applicability of localized heating and cooling as a practical strategy to manipulate wetting on a chemically patterned substrate.

We note that the transition width δ (see section 4.2.3) in these calculations was set to 0.01, which would considerably weaken the gradients in M as compared to the results with M varying from -100 to 100 discussed earlier (section 4.3.2). These results further indicate that competitive dewetting is resulting from the absolute degree of heating and cooling alone, and not the high gradients in M over a localized space.

The chosen value of M may be obtained for an aqueous film with a mean initial thickness of $\sim$ 200 nm and $\epsilon \sim 0.001$, when subjected to a temperature rise of 10 - 15 K. Alternatively, we may also obtain such values for M by invoking higher temperature differences and suitably modulating the other parameters involved (see Table 1). However, excessive heating or cooling may lead to the risk of evaporating or freezing the liquid which would prove detrimental in any physical application. This is more likely a problem with typical aqueous systems, while non-aqueous liquids with higher boiling temperatures or lower freezing temperatures would be able to withstand higher degrees of heating or cooling.

4.4 Conclusions

Motivated by emerging industrial applications, we have perfomed a systematic analysis of thermocapillary-driven single-layer thin film dewetting onto chemically patterned surfaces. Thermal stresses may be incorporated in such flows either by uniform heating/cooling of the system or by localized heating/cooling techniques. Marangoni effects induced by these thermal stresses significantly change the instability behavior due to resulting competitions between wettability gradient-driven flows and thermocapillary-driven flows.

On a chemically patterned substrate with a wide enough heterogeneous patch, intensive cooling can help considerably delay the rupture even in presence of wettability gradients, though not completely suppress it. Uniform heating on the other hand changes the rupture pattern only when the width of the heterogeneity is large enough overcome to trigger an independent rupture at the center of the patch. When combined heating and cooling effects are present, thermocapillary effects can significantly modify the film dynamics by reversing the rupture pattern otherwise occuring due to the wettability gradients. As an example, on a chemically patterned surface with hydrophobic and hydrophilic areas, intensive localized cooling on a hydrophobic patch would prevent a rupture from occuring there. If intensive heating is simultaneously present in the adjoining hydrophilic zones, Marangoni flow-driven-rupture can be induced in those regions. In such a setup, the mechanism of instability is determined by the width of the cooled region w_M relative to the width of the hydrophobic patch w_h. When $w_M > w_h$, the film ruptures on the hydrophobic patch and the film is stabilized on the hydrophobic patch when $w_M < w_h$. However, the interfacial features in each of the regimes remain qualitatively similar, suggesting that the rupture is initiated by the wettability gradients, while the Marangoni forces only assist the rupture thus induced.

The results obtained in the present study provide a convenient handle to precisely deposit liquid on substrates whose wettability is hard to control. Presumably, one can achieve the desired combination of wetting and dewetting by local heating and cooling of the substrate to suitably induce or suppress rupture. This strategy would have tremendous practical significance from the viewpoint of physical applications like templating and in coating and printing flows in processes involving wetting on chemically patterned substrates. For instance, in the lithographic printing process (MacPhee, 1998) an oil-based ink needs to displace an aqueous barrier film to wet selected areas of a substrate known as the ‘image areas’, while a stable aqueous film

is maintained at the 'non-image areas'. The desired result may be achieved by local heating of the zone where rupture is desired, and cooling the adjoining zones. In conventional printing processes where one encounters cylinders that back up rollers (e.g., Figure 4.20), such localized heating and cooling may be implemented at the printing nip by the use of microheaters made of a series of thermal resistors (Darhuber et al., 2003b) or digital coolers (Paik et al., 2008) by attaching ventilator slots to the substrate connected to external coolers.

Interesting dynamics occur when repulsive intermolecular forces are present. Our results indicate that in presence of these repulsive intermolecular forces, there exist a critical smallest spacing of the hydrophobic patch that needs to be maintained between two adjacent hydrophilic patches in order to obtain near-perfect templating. Thermocapillary-driven Marangoni flows increase the size of this smallest spacing required. A general heuristic in terms of the parameter λ_{md} for the smallest hydrophobic patch width is $\sim 0.8\lambda_{md} - 1.5\lambda_{md}$.

We note at this point that besides thermocapillary stresses, surface-active particles like surfactant molecules are another major source of surface-tension gradients, particularly important in coating and printing processes which may be subject to contaminants. Our present work emphasizes only the former aspect of thermocapillary effects, because on probing the effects of Marangoni flows generated by insoluble surface-active particles on chemically patterned surfaces, we observed only small quantitative shifts in the instability behavior. The essential qualitative aspects of instability observed in thin film studies with chemically heterogeneous surfaces in the absence of surface-active particles (Konnur et al., 2000; Kargupta et al., 2000) remained the same. More recently, surfactant spreading along thin liquid films on chemically patterned surfaces has been studied experimentally and numerically by Sinz et al. (2011) without accounting for intermolecular forces. However, the authors in that work have only focused on the dynamics of surfactant spreading and an extensive study of the film instability behavior was not pursued.

The localized heating and cooling strategies which we have modeled in the present work may be implemented in practice by several techniques. Besides the use of conventional resistor-based microheaters, heating induced by an array of focused light beams (e.g., laser-induced heating (Vela et al., 2009)) can provide a convenient way to promote dewetting on a chemically patterned surface. This is particularly useful even for simple laboratory coating experiments like wire-wound rod coating (MacLeod, 2006) on chemically patterned substrates, and the open issue lies in the technological advancement of developing narrow beam sizes. Finally, we point out that our model

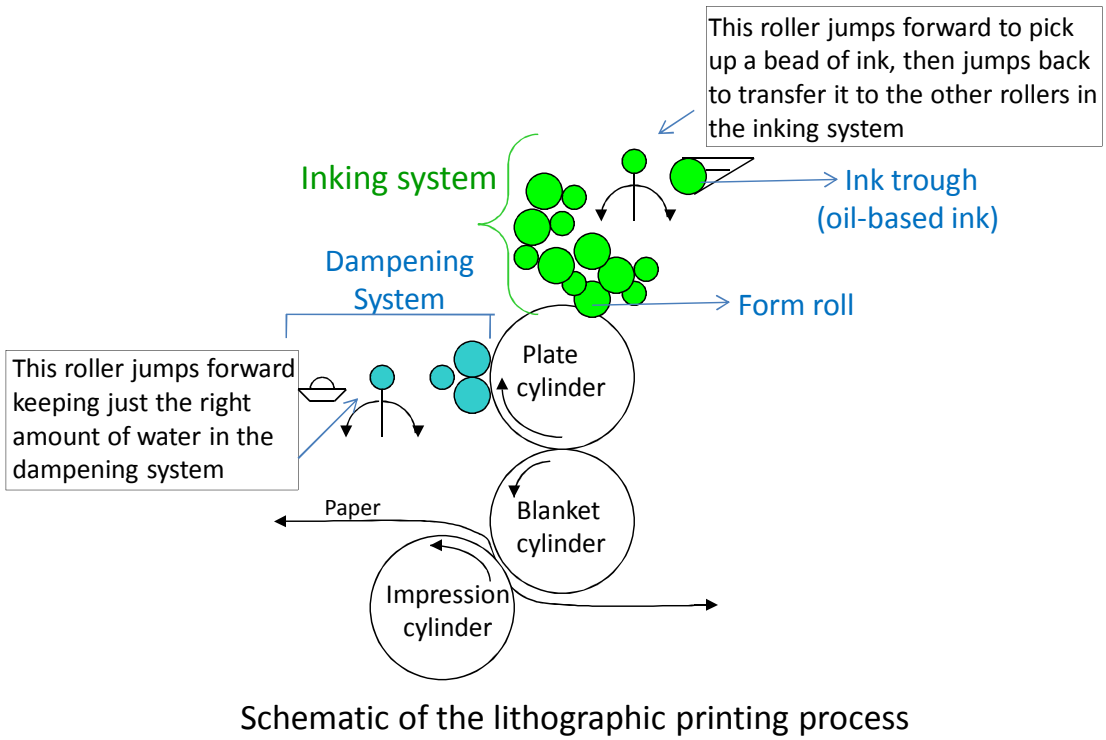

Figure 4.20: Schematic of the lithographic printing process.

problem is based on thin-film flow of a single liquid layer, but it is a starting point to model Marangoni effects in multi-layer flows on chemically patterned surfaces that are particularly useful from the viewpoint of applications like the lithographic printing process or a two-layer slot coating process.

CHAPTER 5

Conclusions

In this thesis we have examined comprehensively three model problems that are industrially relevant and rich topics, and which provide a great depth of understanding of coating and printing on chemically patterned surfaces. The fluid mechanics issues associated with coating and printing processes are key to understand and improve the quality of the coated or printed product. This explains the emphasis in this thesis on characterizing liquid film stability in each of the model problems we have considered. We summarize the key results from each chapter and examine possible directions for future work.

5.1 Summary of key results

Throughout chapters $2-4$, we have included the effect of van der Waals forces in causing film rupture on chemically patterned surfaces, illustrating that these forces play a governing role for films as thick as a few 100 nm. However, several other factors often present in coating and printing flows could compete with these forces, as shear (e.g., Chapter 2), repulsive polar forces (e.g., chapter 3), or thermal effects (e.g., chapter 5). Depending on the relative magnitude of the forces involved, such factors may alter or even destroy the final templated structure of the thin liquid film on the chemically patterned surface.

In chapter 2, it was found that a mean flow resulting from shear can considerably delay rupture as the mean flow tends to convect and steepen interfacial perturbations,

preventing the film from thinning down further. On a chemically patterned surface, the shear not only delays the rupture, but is also instrumental in changing the rupture mechanism. As an example, Figure 2.9 in chapter 2 shows how increased shear velocity modifies the rupture pattern from multiple rupture points at the edges of the pattern to a single rupture at the center. However, from the point of view of lithographic printing, our results suggested that shear may not prove to be a significant factor that affects liquid displacement mechanisms, although the shear rates involved in an actual printing process are high, $\sim 10^5$ s^{-1}.

An extension of the work presented in chapter 2 was pursued in chapter 3 where the model is enriched by the inclusion of a short-range repulsive component of the disjoining pressure, and the distinct effect of the 'non-image' size was probed. Noting that typical nip widths in lithographic printing are on a length scale where these intermolecular forces become important, our model captures phenomena like the formation of droplets (figure 3.5, chapter 3) in equilibrium with an underlying thin film, and suggests new mechanisms of liquid-liquid displacement in lithographic printing. Even more importantly, the addition of the repulsive force component illustrated how near-perfect templating is destroyed, due to 'spill-over' of ink onto the 'non-image' areas. Our results showed that one may obtain estimates of the smallest printable 'image' size and the smallest packing between images in terms of the parameter λ_{md}, the fastest growing wavelength of an interfacial perturbation (see section 3.3.3, chapter 3). This is especially handy for the purpose of design in a real printing process since λ_{md} is in turn a function of the physical properties of the system (e.g., interfacial tension, Hamaker constant).

The competitions to wettability-gradient-driven dewetting from surface-tension gradients or Marangoni effects was examined in Chapter 4. Typical sources of these Marangoni effects in coating and printing processes may be deliberate temperature variations, environments with surface contaminants, or intentional addition of surface-active particles. Among these factors, our results suggested the specific applicability of localized heating and cooling techniques in modifying the rupture patterns in wettability-gradient-driven-flows. This provides a handle to control the liquid deposition on substrates whose wettability is hard to control. Further we demonstrated how even intensive uniform cooling can significantly delay rupture driven by wettability gradients. Depending on the nature of application involved, the delay by factors as large as 10^3 (section 4.3.1, chapter 4) would prove significant for applications where intentional rupture is engineered on chemically patterned surfaces.

5.2 Directions for future work

First, it is necessary to point out that the models constructed herein and the conclusions we have drawn are based on idealizations of the known physics of lithographic printing and other applications considered. In each case, we have had to necessarily invoke a number of simplifying assumptions, with suitable quantitative justification. Each problem therefore offers the scope to construct more complex models which could examine the concerned physical aspects in more detail. As an example, many fluids using in coating processes, incluing the printing inks used in lithographic printing are essentially non-Newtonian in character. Though the Newtonian models used herein are a good starting point, one would aptly need to account for non-Newtonian rheology to understand these processes. Particularly worth mentioning is the issue of shear examined in chapter 2. Our current results suggest that one may be able to understand the mechanics of emulsification of the ink in lithographic printing even at high shear rates of the order 10^5 s^{-1}. Though a considerable variation in the time of rupture is not seen in our model, such shear rates may significantly affect the viscosity ratio and the resulting liquid-liquid displacement mechanisms.

The resolution limitations arising from the 'spill-over' effect described in Chapter 3 is inferred to be largely a consequence of thermodynamic considerations. When the packing space between adjacent images is shrunk, a lower free energy state appears to be the ones where near-perfect templating is lost. Prior studies (Lenz and Lipowsky, 1998; Gau et al., 1999; Lenz et al., 2001; Brinkmann and Lipowsky, 2002) suggest that morphologies of liquid droplets on patterned surface domains are largely a function of the interfacial properties (e.g., surface tension, contact angle with the solid). A detailed free energy minimization analysis is not probed here, but a thermodynamic analysis using tools like the Surface Evolver (Brakke, 1992) could provide insights on possible strategies to restore near-perfect templating. As suggested by current investigations in industrial lithographic printing practices, one may be able to induce differences in surface wettability by the use of additives (MacPhee, 1998) which could further change the dynamics of film evolution.

The model constructed in Chapter 3 could be suitably tailored to understand the dip coating process (Scriven, 1988) on chemically patterned surfaces. To our knowledge, a comprehensive model accounting for the combined interactions of wettability gradients, gravity, and meniscus curvature effects as in the dip coating process has not been formulated, which enables the prediction of steady state film thicknesses on chemically patterned surfaces. The earlier work by Davis (2005) provides an analyt-

ical solution for film thicknesses, only valid in the range $Ca << 1$, and $Bo << 1$, where $Ca = \frac{\mu V}{\gamma}$ is the capillary number and $Bo = \frac{\rho L^2 g}{\gamma}$ is the bond number. Here μ is the liquid viscosity, V is a characteristic velocity, L is a typical length scale, ρ is the density, and γ is the surface tension in the problem. However, the analysis does not account for wettability gradients arising from intermolecular forces. Further it fails to provide a complete numerical solution for the transition from a narrow pattern width to a homogeneous substrate. This could be achieved by extending the model we constructed in chapter 3 to two-dimensions, and including the effect of gravity, while turning the viscosity ratio μ_r to 0.

It is important to point out that computational models are particularly useful for obtaining research insights where length scales as narrow as a micron or a few nanometers is involved. However, many of the model predictions may be tested by real laboratory experiments that are relatively simple to perform. For instance, the validity of thermally-induced competitive dewetting mechanisms presented in Chapter 4 could be utilized to engineer the coating of chemically patterned wire-wound rod coating of a single liquid layer. Such simple laboratory experiments also provide the opportunity to develop and test new heating and cooling techniques as laser-induced heating, or a microfluidic cooling device (see Chapter 4). The model used in chapter 4 would also be aptly treated as a starting point to model single-layer flows, but it could be suitably extended to model liquid-liquid displacement in two-layer applications like lithographic printing. While our analysis is confined to one-dimensional interfacial evolution, two-dimensional dynamics would be required to completely understand the stability regime of the modified rupture profiles in the presence of Marangoni effects.

5.3 Final remarks

Coating and printing on chemically patterned surfaces is an interdisciplinary research topic attracting interest from several emerging industrial applications. Several open issues remain despite the fact that some of these processes like lithographic printing are as old as a century. This is because the fundamentals and the mechanics remain largely not understood, and the underlying issues are complex, requiring in depth application of several scientific branches like surface chemistry, fluid mechanics, and colloidal phenomena. We hope that ideas proposed in this thesis answer some of the open questions in industrial coating and printing process, at the same time offering the tools for developing more sophisticated models.

Bibliography

Arase, H., Nakagawa, T., 2009. Interfacial-energy-controlled deposition technique of microstructures using blade-coating. J. Phys. Chem. B 113, 15278–15283.

Bandyopadhyay, D., Sharma, A., 2010. Self-organized microstructures in thin bilayers on chemically patterned substrates. J. Phys. Chem. 114, 2237–2247.

Bielarz, C., Kalliadasis, S., 2003. Time-dependent free-surface thin film flows over topography. Phys. Fluids 15 (9), 2512–2524.

Brakke, K. A., 1992. The surface evolver. Exp. Math. 1 (2), 141–165.

Brasjen, B. J., Darhuber, A. A., 2011. Dry-spot nucleation in thin liquid films on chemically patterned surfaces. Microfluid. Nanofluid. 11, 703–716.

Brinkmann, M., Lipowsky, R., 2002. Wetting morphologies on substrates with striped surface domains. J. Appl. Phys. 92 (8), 4296–4306.

Brusch, L., Kuhne, H., Thiele, U., Bar, M., 2002. Dewetting of thin films on heterogeneous substrates: Pinning versus coarsening. Phy. Rev. E 66, 011602–1 – 011602–5.

Burelbach, J. P., Bankoff, S. G., Davis, S. H., 1988. Nonlinear stability of evaporating/condensing liquid films. J. Fluid Mech. 195, 463–494.

Burelbach, J. P., Bankoff, S. G., Davis, S. H., 1990. Steady thermocapillary flows of thin liquid layers: II. experiment. Phys. Fluids A 2 (3), 322–333.

Burmeister, F., Schafle, C., Keilhofer, B., Bechinger, C., Boneberg, J., Leiderer, P., 1998. From mesoscopic to nanoscopic surface structures: Lithography with colloid monolayers. Chem. Eng. Technol. 21 (9), 761–763.

Chaug, Y. S., Haubrich, J. E., Sereda, M., Liang, R. C., 2004. Roll-to-roll processes for the manufacturing of patterned conductive electrodes on flexible substrates. Mater. Res. Soc. Symp. Proc. 814, 213–218.

Chen, K. P., 1995. Interfacial instabilities in stratified shear flows involving multiple viscous and viscoelastic fluids. Appl. Mech. Rev. 48 (11), 763–776.

Clark, S. L., Montague, M., Hammond, P. T., 1997. Selective deposition in multilayer assembly: Sams as molecular templates. Supramol. Sci. 4 (1-2), 141–146.

Darhuber, A. A., Davis, J. M., Troian, S. M., 2003a. Thermocapillary actuation of liquid flow on chemically patterned surfaces. Phys. Fluids 15 (5), 1295–1304.

Darhuber, A. A., Troian, S. M., 2005. Principles of microfluidic actuation by modulation of surface stresses. Annu. Rev. Fluid. Mech. 37, 425–455.

Darhuber, A. A., Troian, S. M., Miller, S. M., Wagner, S., 2000. Morphology of liquid microstructures on chemically patterned surfaces. J. Appl. Phys. 87 (11), 7768–7775.

Darhuber, A. A., Valentino, J. P., Troian, S. M., Wagner, S., 2003b. Thermocapillary actuation of droplets on chemically patterned surfaces by programmable microheater arrays. J. Microelectromech. S. 12 (56), 873–879.

Davis, J. M., 2005. Asymptotic analysis of liquid films dip-coated onto chemically micropatterned surfaces. Physics of Fluids 17 (5), 038101–1–4.

Davis, S. H., 1987. Thermocapillary instabilities. Ann. Rev. Fluid Mech. 19, 403–435.

Deen, W. M., 1998. Analysis of Transport Phenomena. Oxford.

Dodds, S., 2011. Stretching and Slipping Liquid Bridges: Liquid Transfer in Industrial Printing. PhD Thesis, University of Minnesota.

Drelich, J., Miller, J. D., Kumar, A., Whitesides, G. M., 1994. Wetting characteristics of liquid drops at heterogeneous surfaces. Colloids Surf., A 93, 1–13.

Drodofsky, U., Stuhler, J., Schulze, T., Drewsen, M., Brezger, B., Pfau, T., Mlynek, J., 1997. Hexagonal nanostructures generated by light masks for neutral atoms. Appl. Phys. B: Lasers and Optics 65 (6), 755–759.

Eijkel, J. C. T., van den Berg, A., 2005. Nanofluidics: What is it and what can we expect from it? Microfluid. Nanofluid. 1 (3), 249–267.

Fowkes, F. M., 1962. Determination of interfacial tensions, contact angles, and dispersion forces in surfaces by assuming additivity of intermolecular interactions in surfaces. J. Chem. Phys. 66, 382.

Garcia, R., Calleja, M., Perez-Murano, F., 1998. Local oxidation of silicon surfaces by dynamic force microscopy: Nanofabrication and water bridge formation. Appl. Phys. Lett. 72 (18), 2295–2297.

Gau, H., Herminghaus, S., Lenz, P., Lipowsky, R., 1999. Liquid morphologies on structured surfaces: From microchannels to microchips. Science 283 (5398), 46–49.

Golovin, A. A., Rubinstein, B. Y., Pismen, L. M., 2001. Effect of van der waals interactions on the fingering instability of thermally driven thin wetting films. Langmuir 17, 3930–3936.

Goto, H., 2007. Overview on nanoimprint technology - process, tools, applications and technical issues for industrialization. Key Eng. Mat. 345-346, 1073–1077.

Gramlich, C. M., Kalliadasis, S., Homsy, G. M., Messer, C., 2002. Optimal leveling of flow over one-dimensional topography by marangoni stresses. Phys. Fluids 14 (6), 1841–1850.

Gunther, A., Jensen, K. F., 2006. Multiphase microfluidics: From flow characteristics to chemical and materials synthesis. IEEE Sens. J. 6, 1487–1503.

Guo, Q., Arnoux, C., Palmer, R. E., 2001. Guided assembly of colloidal particles on patterned substrates. Langmuir 17, 7150–7155.

Hamaker, H. C., 1937. The london-van der waals attraction between spherical particles. Physica 4, 1058–1072.

Hanumanthu, R., Scriven, L. E., 1996. Coating with patterned rolls and rods. TAPPI 79 (5), 126–138.

Hay, G. I., Evans, P. S. A., Harrison, D. J., Southee, D., Simpson, G., Harrey, P. M., 2005. Characterization of lithographically printed resistive strain gauges. IEEE Sens. J. 5 (5), 864–872.

Hay, G. I., Southee, D. J., Evans, P. S. A., Harrison, D. J., Simpson, G., Ramsey, B. J., 2007. Examination of silvergraphite lithographically printed resistive strain sensors. Sens. Actuators, A 135 (2), 534–546.

Hayward, R. C., Saville, D. A., Aksay, I. A., 2000. Electrophoretic assembly of colloidal crystals with optically tunable micropatterns. Nature 404 (6773), 56–59.

Heier, J., Kramer, E. J., Walheim, S., Krausch, G., 1997. Thin diblock copolymer films on chemically heterogeneous surfaces. Macromolecules 30 (21), 6610–6614.

Heule, M., Schonholzer, U. P., Gauckler, L. J., 2004. Patterning colloidal suspensions by selective wetting of microcontact-printed surfaces. J. Eur. Ceram. Soc. 24 (9), 2733–2739.

Higgins, A. M., Jones, R. A. L., 2000. Anisotropic spinodal dewetting as a route to self-assembly of patterned surfaces. Nature 404 (6777), 476–478.

Hoda, N., Kumar, S., 2008. Theory of polyelectrolyte adsorption onto surfaces patterned with charge and topography. J. Chem. Phys. 128 (12), 124907–1–12.

Hohne, D. N., Chen, H., J. Lahann, M. J. S., 2008. Near-surface structure of lithographic ink-fountain solution emulsions on model substrates. Colloids Surf., A: Physicochem. Eng. Aspects 326, 138–146.

Israelachvili, J. H., Adams, G. E., 1978. Measurement of forces between two mica surfaces in aqueous electrolyte solutions in the range 0-100 nm. J. Chem. Soc., Farday Trans. 74, 975–1001.

Israelachvili, J. N., 1972. The calculation of van der waals dispersion forces between macroscopic bodies. Proc. R. Soc. Lond. A 331, 39–55.

Israelachvili, J. N., 1992. Intermolecular and Surface Forces. Academic Press, London.

James, D. W., 1968. The thermal diffusivity of ice and water between -40 and +60 C. J. Mater. Sci. 3, 540–543.

Joo, S. W., Davis, S. H., Bankoff, S. G., 1991. Long-wave instabilities of heated falling films: two dimensional theory of uniform layers. J. Fluid Mech. 230, 117–146.

Joo, S. W., Hsieh, K., 2000. Interfacial instabilities in thin stratified viscous fluids under microgravity. Fluid Dyn. Res. 26 (3), 203–217.

Kaelble, D. H., Dynes, P. J., 1975. Surface energetics of lithography. J. Adhes. Sci. Technol. 9b, 735–761.

Kalpathy, S., Francis, L. F., Kumar, S., 2012. Thin-film models of liquid displacement on chemically patterned surfaces for lithographic printing processes. Submitted to J. Colloid Interface Sci.

Kalpathy, S. K., Francis, L. F., Kumar, S., 2010. Shear-induced suppression of rupture in two-layer thin liquid films. J. Colloid Interface Sci. 348, 271–279.

Kao, J. C. T., Golovin, A. A., Davis, S. H., 2006. Rupture of thin films with resonant substrate patterning. J. Colloid Interface Sci. 303, 532–545.

Kargupta, K., Konnur, R., Sharma, A., 2000. Instability and pattern formation in thin liquid films on chemically heterogeneous substrates. Langmuir 16 (26), 10243–10253.

Kargupta, K., Konnur, R., Sharma, A., 2001. Spontaneous dewetting and ordered patterns in evaporating thin liquid films on homogeneous and heterogeneous substrates. Langmuir 17, 1294–1305.

Kargupta, K., Sharma, A., 2001. Templating of thin films induced by dewetting on patterned surfaces. Phys. Rev. Lett. 86 (20), 4536–4539.

Kargupta, K., Sharma, A., 2002a. Dewetting of thin films on periodic physically and chemically patterned surfaces. Langmuir 18 (5), 1893–1903.

Kargupta, K., Sharma, A., 2002b. Dewetting of thin films on periodic physically and chemically patterned surfaces. Langmuir 18 (5), 1893–1903.

Kargupta, K., Sharma, A., 2002c. Morphological self-organization by dewetting in thin films on chemically patterned substrates. J. Chem. Phys. 116 (7), 3042–3051.

Kargupta, K., Sharma, A., 2003. Mesopatterning of thin liquid films by templating on chemically patterned complex substrates. Langmuir 19, 5153–5163.

Kasunich, C., 1998. Gravure Primer. GATFPress.

Kayser, W. V., 1975. Temperature dependence of the surface tension of water in contact with its saturated vapor. J. Colloid Interface Sci. 56 (3), 622–627.

Khanna, R., Jameel, A. T., Sharma, A., 1996. Stability and breakup of thin polar films on coated substrates: Relationship to macroscopic parameters of wetting. Ind. Eng. Chem. Res. 35, 3081–3092.

Khanna, R., Sharma, A., 1997. Pattern formation in spontaneous dewetting of thin apolar films. J. Colloid Interface Sci. 195, 42–50.

Kipphan, H., 2006. Handbook of print media: technologies and production methods. Springer.

Kistler, S. F., Schweizer, P. M., 1994. Liquid film coating: scientific principles and their technological implications. Chapman & Hall.

Ko, H., Peleshanko, S., Tsukruk, V. V., 2004. Combing and bending of carbon nanotube arrays with confined microfluidic flow on patterned surfaces. J. Phys. Chem. B 108, 4385–4393.

Konnur, R., Kargupta, K., Sharma, A., 2000. Instability and morphology of thin liquid films on chemically heterogeneous substrates. Phys. Rev. Lett. 84 (5), 931–934.

Krishnamoorthy, S., Ramaswamy, B., 1995. Spontaneous rupture of thin liquid films due to thermocapillarity: A full-scale direct numerical simulation. Phys. Fluids 7 (9), 2291–2293.

Kumar, S., Matar, O., 2002. Instability of long-wavelength disturbances on gravity-modulated surfactant-covered thin liquid layers. J. Fluid Mech. 466, 249–258.

Kumar, S., Matar, O. K., 2004. Dewetting of thin liquid films near soft elastomeric layers. J. Colloid Interface Sci. 273 (2), 581–588.

Lenz, P., Fenzl, W., Lipowsky, R., 2001. Wetting of ring-shaped surface domains. Europhys. Lett. 53 (5), 618 – 24.

Lenz, P., Lipowsky, R., 1998. Morphological transitions of wetting layers on structured surfaces. Phys. Rev. Lett. 80 (9), 1920–1923.

Lenz, R. D., Kumar, S., 2007a. Competitive displacement of thin liquid films on chemically patterned substrates. J. Fluid Mech. 571, 33–57.

Lenz, R. D., Kumar, S., 2007b. Instability of confined thin liquid film trilayers. J. Colloid Interface Sci. 316 (2), 660–670.

Leyland, N. S., Evans, J. R. G., Harrison, D. J., 2002. Lithographic printing of ceramics. J. Eur. Ceram. Soc. 22 (1), 1–13.

Lipowsky, R., Lenz, P., Swain, P. S., 2000. Wetting and dewetting of structured and imprinted surfaces. Colloids Surf., A 161, 3–22.

Lopez, G. P., Biebuyek, H. A., Frisbie, C. D., Whitesides, G. M., 1993. Imaging of features on surfaces by condensation figures. Science 260 (5108), 647–649.

Luo, C., Xing, R., Zhang, Z., Fu, J., Han, Y., 2004. Ordered droplet formation by thin polymer film dewetting on a stripe-patterned substrate. J. Colloid Interface Sci. 269, 158–163.

MacLeod, D. M., 2006. Coatings Technology Handbook. Taylor and Francis Group, 3rd ed.

MacPhee, J., 1998. Fundamentals of lithographic printing. GATF Press.

Maldarelli, C., Jain, R. K., Ivanov, I. B., Ruckenstein, E., 1980. Stability of symmetric and unsymmetric thin liquid films to short and long wavelength perturbations. J. Colloid Interface Sci. 78 (1), 118–143.

McCollough, G. T., Rankin, C. M., Weuiner, M. L., 2006. Roll-to-roll manufacturing considerations for flexible, cholesteric liquid-crystal display (ch-lcd) media. J. Soc. Inf. Display, 14 (1), 25–30.

Merkt, D., Pototsky, A., Bestehorn, M., Thiele, U., 2005. Long-wave theory of bounded two-layer films with a free liquid-liquid interface: Short- and long-time evolution. Phys. Fluids 17 (6), 64104–1–20.

Michel, B., Bernard, A., Bietsch, A., Delamarche, E., Geissler, M., Juncker, D., Kind, H., Renault, J. P., Rothuizen, H., Schmid, H., Schmidt-Winkel, P., Stutz, R., Wolf, H., 2001. Printing meets lithography: Soft approaches to high-resolution patterning. IBM J. Res. and Dev. 45, 697–719.

Miladinova, S., Slavtchev, S., Lebon, G., Legros, J., 2002. Long-wave instabilities of non-uniformly heated falling films. J. Fluid Mech. 453, 153–175.

Moller, G., Harke, M., Motschmann, H., Prescher, D., 1998. Controlling microdroplet formation by light. Langmuir 14 (18), 4955–4957.

Nepomnyashchy, A. A., Simanovskii, I. B., 2007. Marangoni instability in ultrathin two-layer films. Phys. Fluids 19, 122103–1–122103–14.

Noh, Y., Zhao, N., Caironi, M., Sirringhaus, H., 2007. Downscaling of self-aligned, all-printed polymer thin-film transistors. Nat. Nanotechnol. 2, 784–789.

Nuzzo, R. G., Rogers, J. A., Menard, E., Lee, K. J., Khang, D., Sun, Y., Meitl, M., Zhu, Z., Nov 24, 2009. Methods and devices for fabricating and assembling printable semiconductor elements. U.S. Patent 7622367.

Oron, A., 2000. Nonlinear dynamics of three-dimensional long-wave marangoni instability in thin liquid films. Phys. Fluids 12 (7), 1633–1645.

Oron, A., Bankoff, S. G., 1999a. Dewetting of a heated surface by an evaporating liquid film under conjoining/disjoining pressures. J. Colloid. Interface Sci. 218, 152–156.

Oron, A., Bankoff, S. G., 1999b. Dewetting of heated surface by an evaporating liquid film under conjoining/disjoining pressures. J. Colloid Interface Sci. 218, 152–166.

Oron, A., Davis, S. H., Bankoff, S. G., 1997. Long-scale evolution of thin liquid films. Rev. Mod. Phys. 69, 931–980.

Oron, A., Rosenau, P., 1994. Formation of patterns induced by thermocapillarity and gravity. J. Fluid Mech. 273, 131–146.

Oss, C. J. V., Chaudhury, M. K., Good, R. J., 1988. Interfacial lifshitz-van der waals and polar interactions in macroscopic systems. Chem. Rev. 88 (6), 927–941.

Paik, P. Y., Pamula, V. K., Chakrabarty, K., 2008. Adaptive cooling of integrated circuits using digital microfluidics. IEEE Trans. Very Large Scale Integr. (VLSI) Syst. 16 (4), 432–443.

Park, J., Suh, K. Y., Seo, S., Lee, H. H., 2006. Anisotropic rupture of polymer strips driven by Rayleigh instability. J. Chem. Phys. 124, 214710–1–5.

Powell, C. A., Savage, M. D., Guthrie, J. T., 2005. Modelling printing processes: A computational approach. Surf. Coat. Int. B 88, 157–230.

Preziosi, L., Chen, K., Joseph, D. D., 1989. Lubricated pipelining: stability of core-annular flow. J. Fluid Mech. 201, 323–356.

Qin, D., Xia, Y., Black, A. J., Whitesides, G. M., 1998. Photolithography with transparent reflective photomasks. J. Vac. Sci. Technol. B 16 (1), 98–103.

Ramires, M. L. V., de Castro, C. A. N., Nagasaka, Y., Nagashima, A., Assael, M. J., Wakeham, W. A., 1994. Standard reference data for thermal conductivity of water. J. Phys. Chem. Ref. Data 24 (3), 1377–1381.

Ramsey, B. J., Harrison, D. J., Southee, D. J., 2007. Characterisation of the lithographic printing of conducting films. TAGA Journal of Graphic Technology 4, 25–34.

Rayleigh, L., 1878. On the stability of jets. Proc. Lond. Math. Soc. 10, 4–13.

Reynolds, O., 1886. On the theory of lubrication and its application to mr. beauchamp tower's experiments, including an experimental determination of the viscosity of olive oil. Philos. Trans. R. Soc. London 177, 157–234.

Reynolds, T. D., 2007. Investigation of patterned particulate coatings. MS Thesis, University of Minnesota.

Reynolds, T. D., Kalpathy, S. K., Kumar, S., Francis, L. F., 2010. Dip coating of charged colloidal suspensions onto substrates with patterned wettability: Coating regime maps. J. Colloid Interface Sci. 352 (1), 202–210.

Satas, D., Tracton, A. A., 2000. Coatings Technology Handbook. Marcel Dekker, 2nd edition.

Schwartz, L. W., Eley, R. R., 1998. Simulation of droplet motion on low-energy and heterogeneous surfaces. J. Colloid Interface Sci. 202, 173–188.

Scriven, L. E., 1988. Physics and applications of dip coating and spin coating. Mater. Res. Soc. 121, 717–729.

Sharma, A., 1993. Relationship of thin film stability and morphology to macroscopic parameters of wetting in the apolar and polar systems. Langmuir 9 (3), 861–869.

Sharma, A., Khanna, R., 1998. Pattern formation in unstable thin liquid films. Phys. Rev. Lett. 81 (16), 3463–3466.

Sharma, A., Khanna, R., 1999. Pattern formation in unstable thin liquid films under the influence of antagonistic short- and long-range forces. J. Chem. Phys. 110 (10), 4929–4936.

Sharma, A., Konnur, R., Kargupta, K., 2003. Thin liquid films on chemically heterogeneous substrates: self-organization, dynamics and patterns in systems displaying a secondary minimum. Physica A 318 (1-2), 262–278.

Sheludko, A., 1967. Thin liquid films. Adv. Colloid Interface Sci. 1, 391–464.

Silver, J., Mi, Z., Takamoto, K., Bungay, P., Brown, J., Powell, A., 1999. Controlled formation of low-volume liquid pillars between plates with a lattice of wetting patches by use of a second immiscible fluid. J. Colloid Interface Sci. 219 (1), 81–89.

Sinz, D. K. N., Hanyak, M., Zeegers, J. C. H., Darhuber, A. A., 2011. Insoluble surfactant spreading along thin liquid films confined by chemical surface patterns. Phys. Chem. Chem. Phys. 13, 9768–9777.

Southee, D. J., Hay, G. I., Evans, P. S. A., Harrison, D. J., 2007. Lithographically printed voltaic cells a feasibility study. Circuit World 33 (1), 31–35.

Speight, J. G., 2007. The Chemistry and Technology of Petroleum. CRC Press/Taylor & Francis, 2007.

.Speth, R. L., Lauga, E., 2009. Capillary instability on a hydrophilic stripe. New J. Phys. 11, 075024–1–15.

Squires, T. M., Quake, S. R., 2005. Microfluidics: Fluid physics at the nanoliter scale. Rev. Mod. Phys. 77 (3), 977–1026.

Stillwagon, L. E., Larson, R. G., 1988. Fundamentals of topographic substrate leveling. J. Appl. Phys. 63, 5251–5258.

Teletzke, G. F., Davis, H. T., Scriven, L. E., 1987. How liquids spread on solids. Chem. Eng. Commun. 55, 41–81.

Thiele, U., Brusch, L., Bestehorn, M., Bar, M., 2003. Modelling thin film dewetting on structured substrates and templates: Bifurcation analysis and numerical simulations. Eur. Phys. J. E. 11, 255–271.

Thiele, U., Neuffer, K., Bestehorn, M., Pomeau, Y., Velarde, M. G., 2002. Sliding drops on an inclined plane. Colloids Surf., A 206, 87–104.

Thiele, U., Velarde, M. G., Neuffer, K., Bestehorn, M., Pomeau, Y., 2001. Sliding drops in the diffuse interface model coupled to hydrodynamics. Phys. Rev. E 64, 061601–1–12.

Tracton, A. A., 2006. Coatings Technology: Fundamentals: Testing, and Processing Techniques. CRC Press.

Tuckerman, D. B., Pease, R. F. W., 1981. High-performance heat sinking for vlsi. IEEE Electron Device Lett. 2 (5), 126–129.

U.S., Aug 23, 1994. Patent 5339737.

U.S., Jul 14, 1981. Patent 4278467.

van Oss, C., Chaudhury, M. K., Good, R. J., 1987. Monopolar surfaces. Adv. Colloid Interface Sci. 28, 35–64.

VanHook, S. J., Schatz, M. F., Swift, J. B., Swinney, H. L., 1997. Long-wavelength instability in surface-tension-driven benard convection: experiment and theory. J. Fluid Mech. 345, 45–78.

Vela, E., Hafez, M., Regnier, S., 2009. Laser-induced thermocapillary convection for mesoscale manipulation. Int. J. Optomechatronics 3, 289–302.

Vrij, A., 1966. Possible mechanism for the spontaneous rupture of thin, free liquid films. Discuss. Faraday Soc. 42, 23–33.

Wang, J. Z., Zheng, Z. H., Li, H. W., Huck, W. T. S., Sirringhaus, H., 2004. Dewetting of conducting polymer inkjet droplets on patterned surfaces. Nat. Mater. 3, 171–176.

Wang, R., Parikh, A. N., Beers, D. J., Shreve, A. P., Swanson, B., 1999. Nonequilibrium pattern formation in langmuir-phase assisted assembly of alkylsiloxane monolayers. J. Phys. Chem. B 103 (46), 10149–10157.

Wayner, P., Kao, Y. K., LaCroix, L. V., 1976. The interline heat-transfer coefficient of an evaporating wetting film. Int. J. Heat Mass Tran. 19 (5), 487–492.

Williams, M. B., Davis, S. H., 1982. Nonlinear theory of film rupture. J. Colloid Interface Sci. 90 (1), 220–228.

Wu, S., 1971. Calculation of interfacial tension in polymer systems. J. Polym. Sci., Part C 34 (1), 19–30.

Xiong, X., Jaberansari, L., Hahm, M. G., Busnaina, A., Jung, Y. J., 2006. Building highly organized single-walled carbon-nanotube networks using template-guided fluidic assembly. Small 3 (12), 2006–2010.

Yang, W., Tsutsui, K., 2000. Overview of boiling on microstructures - macrobubbles from microheaters. Microscale Therm. Engg. 4, 7–24.

Yeo, L. Y., Craster, R. V., Matar, O. K., 2003. Marangoni instability of a thin liquid film resting on a locally heated horizontal wall. Phys. Rev. E. 67, 056315–1–14.

Zope, M., Kargupta, K., Sharma, A., 2001. J. Chem. Phys. 114 (16), 7211–7221.